

# **Mathematical Modelling of Quantum Transport in Nanoscale Structures**

**Ahmad Abdulrhman Almutlg**

PhD Thesis in Mathematics



Submitted in partial fulfilment of the requirements for the degree of

Doctor of Philosophy

April 2021

## **Declaration**

Except where stated otherwise, this thesis is a result of the author's original work and has not been submitted in whole or in part for the award of a higher degree elsewhere. This thesis documents work carried out between October 2018 and March 2021 at Lancaster University, UK, under the supervision of Professor. Colin J. Lambert and funded by Al-Qassim University, Saudi Arabia.

**Ahmad Almutlg**

March 2021

**To my father Abdullrhaman, Allah mercy  
him, and my lovely mother and my brothers.**

## Abstract

Molecular electronics is a versatile test bed for investigating nanoscale thermoelectricity and for contributing to the design of new low-cost and eco-friendly organic thermoelectric materials. This thesis presents theoretical results which aid this design process, firstly through demonstrating the optimisation of thermopower in self assembled monolayers based on the pressure applied to the molecules, and secondly through a novel method of predicting thermoelectric properties based on experimental  $I - V$  curves. This thesis provides a brief introduction to the theoretical tools used, starting in chapter 2 with density functional theory and its implementation in the SIESTA code, which enables Hamiltonians and ground state wavefunctions for molecules and junction interfaces to be found. Subsequently in chapter 3 the theoretical basis for calculating electronic and heat transport is described, including Green's function methods for obtaining the transmission coefficient of semi-infinite leads connected to a scattering region. The second tool is the quantum transport code GOLLUM. To introduce this approach, in chapter 3 I present solutions of Green's functions for infinite and semi-infinite chains and the transmission coefficient equation which forms the theoretical basis of this code.

Chapter 4 is the first results chapter in this thesis, which demonstrates a major potential advantage of creating thermoelectric devices using self-assembled monolayers (SAMs). Two anthracene based SAMs terminated with thioacetate are investigated: **9,10**- di(4-(ethynyl)phenylthioacetate), and **1,5**- di(4-(ethynyl)phenylthioacetate). I demonstrate that the thermoelectric properties of such molecular devices can be controlled by taking advantage of their mechanical flexibility, more specifically by tuning the optimum power via the applied pressure which alters the molecules' tilt angle  $\theta$ . Through

systematic theoretical simulations, I show how varying  $\theta$  increases the conductance  $G$  while decreasing thermopower  $S$ , ultimately achieving the optimum power  $P = G S^2$  at  $\theta \approx 65^\circ$ . Excellent agreement has been obtained between my simulations and experimental measurements using conductive Atomic Force Microscopy (AFM) for both SAMs.

The thermoelectric properties of SAMs fabricated from thiol terminated molecules were measured by my collaborators, with a modified AFM system, and the conformation of the SAMs was controlled by regulating the loading force between the organic thin film and the probe, which changes the tilt angle at the metal-molecule interface. The thermopower shift versus the tilt angle of the SAM was tracked and showed that changes in both the electrical conductivity and Seebeck coefficient combine to optimise the power factor  $P$  at a specific tilt angle. This optimisation of thermoelectric performance via applied pressure is confirmed through the use of my theoretical calculations and is expected to be a general method for optimising the power factor of SAMs.

In chapter 5, I address the question of whether the Seebeck coefficient of a single molecule or SAM can be predicted from a measurement of  $I - V$  curves. If so, then the experimentally more difficult task of creating a set-up to measure their thermoelectric properties could be avoided, thus saving a significant amount of cost and effort. My theoretical approach begins by making a fit to measured  $G - V$  curves using three fitting parameters, denoted  $a, b$  and  $c$ , hence I refer to this method as 'ABC' theory. Then predicts a maximum value for the magnitude of the corresponding Seebeck coefficient. This is a useful material parameter, because if the predicted upper bound is large, then the material would warrant further investigation using a full Seebeck measurement setup. On the other hand, if the upper bound is small, then the material would not be

promising and this much more technically demanding set of measurements would be avoided.

Histograms of predicted Seebeck coefficients from the 'ABC' theory are compared with histograms of directly measured Seebeck coefficients using a Scanning Tunnelling Microscope (STM) device. This is done for six SAMs of anthracene-based molecules with different anchor groups including pristine thioether, pristine thioacetate, pristine pyridine and a mixture of thioether and pyridine. I show that excellent agreement is found in each case, both when using all three parameters  $a, b$  and  $c$  in the fitting procedure, and also when the number of parameters is reduced to two by setting  $c = 0$ .

## **Acknowledgements**

I am so grateful to my supervisors Professor Colin Lambert and Dr Ali Ismael for their support and for guiding me to achieve my goals. Also, I would like to thank all the members of the group that I have worked with during my PhD studies. Moreover, I would like to thank my sponsor Al-Qassim University, KSA. Finally, words cannot express how grateful I am to my father, who I lost whilst writing this thesis, and my lovely mother for her sacrifices.

## List of publication during PhD studies

1. Wang, X., Ismael, A., **Almutlg, A.**, Alshammari, M., Al-Jobory, A., Alshehab, A., Bennett, T., Wilkinson, L., Cohen, L., Long, N., Robinson, B. and Lambert, C., **2021**. Optimised power harvesting by controlling the pressure applied to molecular junctions. *Chemical Science* (accepted).
2. Ismael, A., Al-Jobory, A., Wang, X., Alshehab, A., **Almutlg, A.**, Alshammari, M., Grace, I., Benett, T., Wilkinson, L., Robinson, B., Long, N. and Lambert, C., **2020**. Molecular-scale thermoelectricity: as simple as ‘ABC’. *Nanoscale Advances*, 2(11), pp.5329-5334.

## Table of Contents

Abstract .....	iv
Acknowledgements.....	vii
List of publication during PhD studies .....	viii
Table of Contents.....	ix
List of Figures .....	xiii
List of Tables .....	xix
List of abbreviations .....	xx
1. Introduction.....	1
1.1 Molecular electronics and thermopower.....	1
1.2 Thesis outline.....	3
1.3 Bibliography .....	6
2. Density Functional Theory .....	16
2.1 Introduction.....	16
2.2 The Schrödinger Equation and Variational Principle .....	17
2.3 The Hohenberg-Kohn Theorems .....	21
2.4 The Kohn-Sham Method and Self-Consistent Field.....	24
2.5 The Exchange-Correlation Functional.....	30
2.6 Local Density Approximation (LDA).....	30
2.7 Generalized Gradient Approximation (GGA) .....	32
2.8 SIESTA.....	34

2.9 The Pseudo-Potential Approximation.....	35
2.10 Bibliography .....	36
3. Quantum Transport and Green's Functions Method .....	42
3.1 Introduction.....	42
3.2 Landauer Formula.....	43
3.3 Thermoelectric coefficients .....	47
3.4 Scattering in One Dimension.....	53
3.4.1 Perfect One-Dimensional Lattice .....	53
3.4.2 One-Dimensional Scattering Solution.....	59
3.5 Generalisation of the Scattering Formalism .....	63
3.5.1 Hamiltonian and Green's Function of the Leads .....	64
3.5.2 Effective Hamiltonian of the Scattering Region .....	73
3.5.3 Scattering Matrix.....	75
3.6 Bibliography .....	77
4. Optimised Power Harvesting in Anthracene-Based SAMs Junctions .....	80
4.1 Introduction.....	80
4.2 Motivation.....	80
4.3 Introduction.....	81
4.4 Product Rule .....	83
4.5 Frontier orbitals of molecules 1 and 2 .....	87
4.6 Binding energy of molecules on Au-substrate.....	90
4.7 Optimised DFT Structures of Compounds in their Junctions.....	92

4.8 The tilt angle ( $\theta$ ) .....	92
4.9 Beyond the optimised tilt angle ( $\theta$ ) .....	93
4.10 DFT Calculations .....	94
4.11 Transport calculations.....	95
4.12 Seebeck Coefficient Calculations .....	97
4.13 Mechanical Gating Charge Transport in Molecular Junctions .....	99
4.14 2-D Histogram .....	100
4.15 Theory Versus Experiment .....	100
4.16 Conductance G .....	101
4.17 The Conductance Ratio $G_1/G_2$ .....	103
4.18 Seebeck Coefficient .....	104
4.19 Power Factor .....	105
4.20 Charge Transport .....	108
4.21 Bibliography .....	110
5. ABC Theory of Molecular-Scale Thermoelectricity .....	118
5.1 Introduction.....	118
5.2 Motivation.....	119
5.3 Studied Molecules.....	120
5.4 ABC Theory.....	121
5.5 Proof that $IV, a, b, c = IV, a, -b, c$ .....	125
5.6 Curve Fitting .....	126

5.7 Experimental Data ( $I - V$ Characterisation) .....	129
5.8 Applying the Curve fitting procedure .....	133
5.9 Histograms of Seebeck coefficients.....	136
5.10 Mean Square Deviations $\chi$ Versus Standard Deviations $\sigma$ .....	142
5.11 Parameter $c$ .....	144
5.12 ( $I - V$ ) Fit Versus ( $G - V$ ) Fit.....	147
5.13 Conclusion .....	149
5.14 Bibliography .....	150
6. Conclusion and Future Work.....	156
6.1 Conclusion .....	156
6.2 Future work.....	158

## List of Figures

Figure 2.1 Flowchart of the self-consistent DFT cycle.....	28
Figure 3.1: A mesoscopic scatterer linked to contacts with ballistic leads. $\mu_L$ and $\mu_R$ represent the chemical potential of the left and right contacts, respectively. .....	44
Figure 3.2: Tight-binding approximation of a one-dimensional periodic lattice with on-site energies $\varepsilon_o$ and couplings $-\gamma$ .....	53
Figure 3.3: A schematic illustration the retarded Green's function structure for an infinite one-dimensional lattice.....	56
Figure 3.4: Tight-binding model of a one-dimensional scatterer connected to one-dimensional leads.....	60
Figure 3.5: Schematic representation of semi-infinite generalised leads. States described by the Hamiltonian $H_0$ are linked by a generalised hopping matrix $H_1$ . The direction $z$ is defined to be parallel to the chain axis. A label $z$ can be assigned to every slice.....	64
Figure 4.1. Chemical structures of molecules 1 and 2 studied in this chapter. 1 (9,10-di(4-(ethynyl)phenylthioacetate) anthracene and 2 (1,5-di(4-(ethynyl)phenylthioacetate) anthracene. ....	82
Figure 4.2. Fully relaxed isolated molecules 1 and 2. Key: C = grey, H = white, O = red, S = yellow (synthesis reported [12, 13])......	83
Figure 4.3: a: Fully optimised structure of naphthalene. b: Wavefunction plots of naphthalene: HOMO (Highest Occupied Molecular Orbital, LUMO (Lowest Occupied Molecular Orbitals), HOMO-1 and LUMO+1 along with their energies. ....	85

Figure 4.4: a: Fully optimised conformation of 1. b: Wavefunction plots of 1 for HOMO (Highest Occupied Molecular Orbitals), LUMO (Lowest Occupied Molecular Orbitals), HOMO-1 and LUMO+1 along with their energies. 88

Figure 4.5: a: Fully optimised conformation of 2. b: Wavefunction plots of 2 for HOMO (Highest Occupied Molecule Orbitals), LUMO (Lowest Occupied Molecule Orbitals), HOMO-1 and LUMO+1 along with their energies. .... 89

Figure 4.6. Example binding energy plot of 1, for thiol anchor Au-S (left), with its idealised ad-atom configuration at the Au lead interface Au-S. Key: C = grey, H = white, S = light yellow, Au = dark yellow..... 91

Figure 4.7. Optimised structures of molecules 1 and 2. Tilt angle (side-view)..... 92

Figure 4.8. Optimised structures of molecules 1 and 2..... 93

Figure 4.9. Schematic illustrations of modelling an increase in the tilt angle (pressure model). .... 94

Figure 4.10. Zero bias transmission coefficient  $T(E)$  of molecule 1 as a function of pressure. The tilt angle varies from approximately  $55^\circ$  (red curve, light pressure) to  $80^\circ$  . (The blue arrow points towards heavy pressure; for clarity, not all curves are shown). .... 96

Figure 4.11. Zero bias transmission coefficient  $T(E)$  of molecule 2 as a function of pressure. The tilt angle varies from approximately  $55^\circ$  (red curve, light pressure) to  $80^\circ$  . (The blue arrow points towards heavy pressure; for clarity, not all curves are shown). .... 96

Figure 4.12. Seebeck coefficient  $S$  of molecule 1 as a function of pressure. The tilt angle varies from approximately  $55^\circ$  (red curve, light pressure) to  $80^\circ$  . (The blue arrow points towards heavy pressure; for clarity, not all curves are shown). .... 98

Figure 4.13 Seebeck coefficient $S$ of molecule 2 as a function of pressure. The tilt angle varies from approximately $55^\circ$ (red curve, light pressure) to $80^\circ$ . (The blue arrow points towards heavy pressure; for clarity, not all curves are shown). .....	98
Figure 4.14. Current transport in molecular junctions 1 and 2. Current plotted versus bias voltage for 1 and 2 (left and right respectively). ....	99
Figure 4.15. $I/V$ plotted versus bias voltage for 1 and 2 (left and right respectively). ....	99
Figure 4.16. Two-dimensional visualization of $I/V$ versus bias voltage for 1 and 2. .....	100
Figure 4.17. Electrical conductance of SAM of molecule 1 at different tilt angles $\theta$ , including a comparison between theory and experiment. ....	102
Figure 4.18. Electrical conductance of SAM of molecule 2 at different tilt angles $\theta$ , including a comparison between theory and experiment. ....	102
Figure 2.19. A lattice of sites representing anthracene. The connectivity table of anthracene. ....	103
Figure 4.20. Conductance ratio between SAMs of molecule 1 and molecule 2 at different tilt angle. ....	104
Figure 4.21. Seebeck coefficient of SAM of 1 at different tilt angles. ....	105
Figure 4.22 Seebeck coefficient of SAM of 2 at different tilt angles. ....	105
Figure 4.23. The experimentally measured and theoretical predicted power factor of a SAM of molecule 1. ....	107
Figure 4.24. The experimentally measured and theoretical predicted power factor of a SAM of molecule 2. ....	107
Figure 4.25. Mechanical gating of charge transport in molecular junctions. Two-dimensional visualization of $I/V$ versus bias voltage for SAMs of 1 and 2.	

The top panels (a-b) are DFT calculations, while the lower panels (c-d) are experimental results. ....	108
Figure 5.1: Structures of studied anthracene-based molecular wires. 1, 2, 3 and 5 correspond to the 7,2' connectivity, while 4 and 6 correspond to the 1,5' connectivity around the central anthracene core. These molecules also differ in the anchor groups through which they bind to a terminal electrode, with the binding groups denoted as follows; 1 = PySMe, 2 = 2Py, 3 and 4 = 2SAc, 5 and 6 = 2SMe. ....	120
Figure 5.2: Example of an experimental $I - V$ curve. ....	127
Figure 5.3: Example $G - V$ curve; the spike occurs due to dividing by zero. ....	127
Figure 5.4: Example of a smooth $G - V$ curve after deleting the spike close to zero volts. ....	128
Figure 5.5: Example of a comparison between experimental values of $G/G_0$ versus voltage $V$ (blue-circles) and the fitted curve from ABC theory (red-solid line). ....	128
Figure 5.6: $I - V$ curves obtained from STM device of molecule 1. ....	130
Figure 5.7: $I - V$ curves obtained from STM device of molecule 2. ....	130
Figure 5.8: $I - V$ characterisation experimental curves obtain from STM device of molecule 3. ....	131
Figure 5.9: $I - V$ characterisation experimental curves obtain from STM device of molecule 4. ....	131
Figure 5.10: $I - V$ characterisation experimental curves obtain from STM device of molecule 5. ....	132
Figure 5.11: $I - V$ characterisation experimental curves obtain from STM device of molecule 6. ....	132

Figure 5.12: A comparison between experimental values of $\log (G/G_0)$ versus voltage $V$ (blue-circles) obtained from STM and the fitted curve from ABC theory (red-solid line) for molecule 1. ....	133
Figure 5.13: A comparison between experimental values of $\log (G/G_0)$ versus voltage $V$ (blue-circles) and the fitted curve from ABC theory (red-solid line) for molecule 2.....	134
Figure 5.14: A comparison between experimental values of $\log (G/G_0)$ versus voltage $V$ (blue-circles) and the fitted curve from ABC theory (red-solid line) for molecule 3.....	134
Figure 5.15: A comparison between experimental values of $\log (G/G_0)$ versus voltage $V$ (blue-circles) and the fitted curve from ABC theory (red-solid line) for molecule 4.....	135
Figure 5.16: A comparison between experimental values of $\log (G/G_0)$ versus voltage $V$ (blue-circles) and the fitted curve from ABC theory (red-solid line) for molecule 5.....	135
Figure 5.17: A comparison between experimental values of $\log (G/G_0)$ versus voltage $V$ (blue-circles) and the fitted curve from ABC theory (red-solid line) for molecule 6.....	136
Figure 5.18: Experimentally derived and predicted ABC theory histograms along with their Gaussian and folded fit curves (black- and blue-solid lines) for 1 (green experiment, yellow absolute experiment and red absolute theory).....	137
Figure 5.19: Experimentally derived and predicted ABC theory histograms along with their Gaussian and folded fit curves (black- and blue-solid lines) for 2 (green experiment, yellow absolute experiment and red absolute theory).....	137

Figure 5.20: Experimentally derived and predicted ABC theory histograms along with their Gaussian and folded fit curves (black- and blue-solid lines) for 3 (green experiment, yellow absolute experiment and red absolute theory)..... 138

Figure 5.21: Experimentally derived and predicted ABC theory histograms along with their Gaussian and folded fit curves (black- and blue-solid lines) for 4 (green experiment, yellow absolute experiment and red absolute theory)..... 138

Figure 5.22: Experimentally derived and predicted ABC theory histograms along with their Gaussian and folded fit curves (black- and blue-solid lines) for 5 (green experiment, yellow absolute experiment and red absolute theory)..... 139

Figure 5.23: Experimentally derived and predicted ABC theory histograms along with their Gaussian and folded fit curves (black- and blue-solid lines) for 6 (green experiment, yellow absolute experiment and red absolute theory)..... 139

Figure 5.24 Experimental and ABC-theory predictions for average of the magnitudes of Seebeck coefficients  $\langle |S| \rangle$  (yellow- and red-circles respectively)..... 140

Figure 5.25. Standard deviations  $\sigma$  obtained from experiment and predicted ABC theory data (yellow- and red-circles). ..... 142

Figure 5.26: Distributions of root mean square deviations ( $\chi$ ) from individual  $G - V$  fits for molecules 1-6. .... 143

## List of Tables

Table 3.1: Sorting the eigenstates into left and right propagating or decaying states based on the wave number and group velocity. ....	<b>67</b>
Table 4.1: Product Rule of Naphthalene molecule for three different connectivities: 1-5, 1-6 and 1-10. PR applies on three regions: reg.1, reg.2 and reg.3, (red colour is +ive, blue -ive, c=constructive and d=destructive). ....	<b>86</b>
Table 4.2: Product Rule of 1. PR applies on three regions: reg.1, reg.2 and reg.3, (red colour is +ive, blue -ive, c=constructive and d=destructive). ....	<b>90</b>
Table 4.3: Product Rule of 2. PR applies on three regions: reg.1, reg.2 and reg.3, (red colour is +ive, blue -ive, c=constructive and d=destructive). ....	<b>90</b>
Table 4.4: Experimental break-off distance and equivalent theoretical tilt angle ( $\theta$ ). <b>93</b>	
Table 5.1: A comparison between the differences in standard deviations between theory and experiment ( $\Delta\sigma$ ), and the average root mean square deviations ( $\langle\chi\rangle$ ) from $G - V$ fits. ....	<b>144</b>
Table 5.2 Absolute ABC predicted theory Seebeck coefficients $ S $ ( $\mu\text{V}/\text{K}$ ) in two cases $c = 0$ and $c \neq 0$ for 10 ( $I - V$ ) characteristics curves for each molecule 1-6 (numbers in parentheses when $c \neq 0$ ), and experiment Seebeck coefficients. ....	<b>145</b>
Table 5.3: Absolute theoretical Seebeck coefficient $ S $ ( $\mu\text{V}/\text{K}$ ) of nearly a thousand ( $I - V$ ) characteristics curve in two cases when $c = 0$ and $c \neq 0$ and absolute experiment Seebeck coefficient. ....	<b>146</b>
Table 5.4: Absolute Seebeck coefficient $ S $ ( $\mu\text{V}/\text{K}$ ) obtained from two fits, ( $G - V$ ) and ( $I - V$ ). ....	<b>148</b>

## List of abbreviations

DFT	Density Functional Theory
LDA	Local Density Approximation
GGA	Generalized Gradient Approximation
SCF	Self-Consistent Field
vdW	Van der Waals
DZ	Double- $\xi$ basis set
DZP	Double- $\xi$ polarized basis set
SIESTA	Spanish Initiative for Electronic Simulations with Thousands of Atoms
LCAOB	Linear Combination of Atomic Orbital Basis
T(E)	Transmission coefficient
S	Seebeck coefficient
LCAO	Linear Combination of Atomic Orbital
DOS	Density of States
STM	Scanning Tunnelling Microscopy
SAM	Self-Assembled Monolayer
G	electrical conductivity
P	Power factor
AFM	Atomic Force Microscope
PR	Product Rule
HOMO	Highest Occupied Molecular Orbital
LUMO	Lowest Occupied Molecular Orbital
I-V	Current Voltage

# Chapter 1

## 1.Introduction

### 1.1 Molecular electronics and thermopower

Since Moore's law was first proposed in 1965, thousands of studies have been carried out to seek ways to continue this historical trend. Over time, the length scale of such studies has become smaller and smaller, and is now focused on the *nano* or *molecular scale* [1]. The crucial challenges, both theoretical and experimental, in this area are the fabrication of devices at the *sub*-10 nm scale and the exploration of their properties.

A reduction in the size of electronic components was proposed in 1974, when Aviram and Ratner suggested the substitution of silicon chips by molecules [2]; their idea provided the foundation for the field of molecular electronics. Since then, the efforts of experts from many disciplines combining experiment and theory has vastly expanded the field. A significant achievement has been the development of computational and modelling tools to obtain theoretical results which closely match experimental measurements. Meanwhile, the latest experimental techniques, such as scanning tunnelling microscopy (STM) break junctions [4], allow the investigation of the electronic properties of a single molecule.

During the past couple of decades, the theory of molecular-scale electronics has advanced significantly, in part by comparing prediction of material-specific transport codes, such as SMEAGOL and GOLLUM [5,6] with state-of-the-art experiments. Notable examples include studies of transport through long conjugated wires [7-10]

graphene nanoribbons and graphene break junctions [11-25]. These studies have revealed the crucial role played by conformation [26,27] and connectivity [28-30] in determining the electrical conductance of single molecules.

More recently, theories of phonon transport at the nanoscale [31,32] have been generalised to describe phonon transport at the molecular scale [33-35]. These studies highlight the role of electrodes in controlling phonon scattering at interfaces and suggests that exploration of alternative electrode materials such as platinum, palladium or even iron [36,37] may be a fruitful route to controlling the flow of heat at the molecular scale. In a more exotic direction, the use of superconducting electrodes is now being explored, in which superconducting interference effects associated with Andreev scattering [38-42] coexist with quantum interference effects associated with frontier orbitals in molecular-scale junctions [43,44].

As well as explorations of electrical and thermal conductance, there has been much progress in understanding the thermoelectrical properties of single-molecule junctions [45-48], stimulated in part by reports of high Seebeck coefficients of order  $161 \mu\text{VK}^{-1}$  for PEDOT:PSS organic films [49]. In this regard, thermoelectricity in fullerenes and nanotubes has led to the observation that the sign of the Seebeck coefficient in fullerenes and nanotubes can be switched by pressure, strain and inter-molecular interactions [50-55]. Interestingly, many of the quantum interference effects observed and predicted in single-molecule junctions are now being scaled up into self-assembled monolayers [56-58], leading to new thin-film materials whose room-temperature transport properties are controlled by quantum effects. These development suggest that the field of single molecule electronics has a tremendous future for the design of new functional materials.

## 1.2 Thesis outline

In this thesis, I present the main equations and theoretical tools that constitute the foundation of these projects. In chapter 2, density functional theory as a method for solving the Schrödinger equation is reviewed. The Hohenberg-Kohn theorems [59] and the Kohn-Sham ansatz [60] are described. The functional forms of the exchange and correlation energy in the local density approximation [61] and the generalized gradient approximation [62] are explained. Finally, the SIESTA code [63] is introduced, along with some fine details of the calculations, such as the use of pseudopotentials and finite basis sets.

Next, in chapter 3, I discuss single particle charge transport through molecules by introducing quantum transport theory, with some examples of how to calculate the transmission coefficient for different systems using the Hamiltonian and Green's functions.

This is followed by my first results chapter which investigates optimising the power harvested by anthracene based molecular junctions by controlling the applied pressure. This study is a result of a collaboration between chemists from Imperial College London, experimental physicists from Lancaster University and myself in Lancaster. Two anthracene-based SAMs have been synthesised with thioacetate (ASc) as an anchor group: **9,10-** di(4-(ethynyl)phenylthioacetate), and **1,5-**di(4-(ethynyl)phenylthioacetate). The two SAMs differ by the connectivity of the anthracene cores to the backbone of the molecules. In this work, I demonstrate that the thermoelectric properties such as thermopower  $S$  and conductance  $G$  can be tuned to achieve an optimum power factor  $P = G S^2$ . The optimum power can be reached by

varying the applied pressure, in other words, changing tilt angle  $\theta$ . Through systematic theoretical simulations, I demonstrate how the tilt angle  $\theta$  is a pivotal factor in increasing both the conductance  $G$  and thermopower  $S$  and ultimately achieving the optimum power  $P = G S^2$  at tilt angle  $\theta \approx 65^\circ$ . An excellent agreement has been obtained between my simulations and the STM measurements for both SAMs.

Chapter 5, the second results chapter, is also a result of a collaboration between chemists from Imperial College London, experimental physicists from Lancaster University and myself. Here I answer the question of whether one could predict the Seebeck coefficient of a SAM or single molecule simply from an experimental  $I - V$  curve. If so, then the experimentally more difficult task of creating a set-up to measure their thermoelectric properties could be avoided, meaning a significant amount of efforts and cost could be saved.

Although this work is a collaboration, the whole study is a theoretical approach since all that is needed from the experiment is an  $I - V$  curve. This chapter presents a novel strategy for predicting an upper bound to the Seebeck coefficient of single molecules or SAMs, from measurements of their  $G - V$  characteristics. My theoretical approach begins by making a fit to measured  $G - V$  curves using three fitting parameters, denoted  $a, b, c$ . In this work, histograms of predicted Seebeck coefficients of the ‘ $ABC$ ’ theory are compared with histograms of the directly measured Seebeck coefficients from a Scanning Tunnelling Microscope STM device. These histograms, along with standard deviations  $\sigma$ , are obtained for six different SAMs, formed from anthracene-based molecules with different anchor groups including pristine thioether, pristine thioacetate, pristine pyridine and a mixture of thioether and pyridine.

I also discuss the case when the three parameters  $a, b, c$  of the ‘ $ABC$ ’ theory are reduced to only two ( $a$  and  $b$ ) by setting  $c$  to be zero. In both cases an excellent agreement is reached with the experiment results.

Finally, in chapter 6, I present the conclusions of this thesis and discuss future work.

### 1.3 Bibliography

1. Leon, S. J., Bica, I., & Hohn, T. (1998). Linear algebra with applications (Vol. 6). Upper Saddle River, NJ: Prentice Hall.
2. Visions for a molecular future. S J van der Molen et al Nat. Nano 8 385 (2013)
2. Molecular rectifiers. A. Aviram, and M.A. Ratner, Chemical physics letters, 29(2), 277-283. (1974)
3. Basic concepts of quantum interference and electron transport in single-molecule electronics. C.J. Lambert, Chemical Society Reviews, 44(4), 875-888 (2015)
4. Single-molecule quantum-transport phenomena in break junctions. P. Gehring, J. Thijssen and H.S.J van der Zant, Nat. Rev. Phys. 1 381 (2019)
5. Spin and molecular electronics in atomically generated orbital landscapes. AR Rocha, VM García-Suárez, S Bailey, C Lambert, J Ferrer, S Sanvito, Phys.Rev. B 73 (8), 085414 (2006)
6. GOLLUM: a next-generation simulation tool for electron, thermal and spin transport. Jaime Ferrer, Colin J Lambert, Víctor Manuel García-Suárez, D Zs Manrique, D Visontai, L Oroszlany, Rubén Rodríguez-Ferradás, Iain Grace, SWD Bailey, Katalin Gillemot, Hatef Sadeghi, LA Algharagholy, New Journal of Physics 16 (9), 093029 (2014)

7. Single-molecule electrical studies on a 7 nm long molecular wire, GJ Ashwell, B Urasinska, C Wang, MR Bryce, I Grace, CJ Lambert, *Chemical communications*, 4706-4708 (2006)
8. Bias-driven conductance increase with length in porphyrin tapes. Edmund Leary, Bart Limburg, Sara Sangtarash, Asma Alanazy, Iain Grace, Katsutoshi Swada, Louisa J. Esdaile, Mohammed Noori, M. Teresa González, Gabino Rubio-Bollinger, Hatef Sadeghi, Nicolás Agrait, Andrew Hodgson, Simon J. Higgins, Colin J. Lambert, Harry L. Anderson and Richard J. Nichols, *J. Am. Chem. Soc.* 140 (40), 12877-12883 (2018)
9. The conductance of porphyrin-based molecular nanowires increases with length. N Algethami, H Sadeghi, S Sangtarash, CJ Lambert, *Nano Letters* 18 (7), 4482-4486 (2018)
10. Structure-Independent Conductance of Thiophene-Based Single-Stacking Junctions Wenjing Hong, Xiaohui Li; Qingqing Wu; Jie Bai; Songjun Hou; Wenlin Jiang; Chun Tang; Hang Song; Xiaojuan Huang; Jueting Zheng; Yang Yang; Junyang Liu; Yong Hu; Jia Shi; Zitong Liu; Colin Lambert; Deqing Zhang, *Angewandte Chemie International Edition* 59 (8), 3280-3286 (2020)
11. A Mechanically Tunable Quantum Dot in a Graphene Break Junction. Caneva Sabina, Hermans Matthijs, Lee Martin, García-Fuente Amador, Watanabe Kenji, Taniguchi Takashi, Dekker Cees, Ferrer Jaime, SJ Herre, Gehring Pascal. *Nano Letters* 20, 4924 (2020)

12. Exchange interactions from a nonorthogonal basis set: From bulk ferromagnets to the magnetism in low-dimensional graphene systems. L Oroszlány, J Ferrer, A Deák, L Udvardi, L Szunyogh, *Phys. Rev. B* 99 (22), 224412 (2019)
13. Mechanically Controlled Quantum Interference in Graphene Break Junctions. Sabina Caneva, Pascal Gehring, Víctor M García-Suárez, Amador García-Fuente, Davide Stefani, Ignacio J Olavarria-Contreras, Jaime Ferrer, Cees Dekker, Herre SJ van der Zant, *Nature Nanotechnology* 13 1126 (2018)
14. Spin signatures in the electrical response of graphene nanogaps. Víctor M García-Suárez, Amador García-Fuente, Diego J Carrascal, Enrique Burzurí, Max Koole, Herre SJ van der Zant, Maria El Abbassi, Michel Calame, Jaime Ferrer, *Nanoscale* 2018,10, 18169 (2018)
15. Effects of antidots on the transport properties of graphene nanoribbons. XH Zheng, GR Zhang, Z Zeng, VM García-Suárez, CJ Lambert *Physical review b* 80 (7), 075413 (2009)
16. Quantum interference in graphene nanoconstrictions. Pascal Gehring, Hatef Sadeghi, Sara Sangtarash, Chit S. Lau, Junjie Liu, Arzhang Ardavan, Jamie H. Warner, Colin J. Lambert, G. Andrew. D. Briggs, Jan A. Mol, *Nano Letters* 16 (7), 4210-4216 (2016)
17. Spin signatures in the electrical response of graphene nanogaps. Víctor M García-Suárez, Amador García-Fuente, Diego J Carrascal, Enrique Burzurí, Max Koole, Herre SJ van der Zant, Maria El Abbassi, Michel Calame, Jaime Ferrer, *Nanoscale* 2018,10, 18169 (2018)

18. Spin-state dependent conductance switching in single molecule-graphene junctions. Enrique Burzurí, Amador García-Fuente, Victor García-Suárez, Kuppusamy Senthil Kumar, Mario Ruben, Jaime Ferrer, Herre SJ Van Der Zant, *Nanoscale* 10 (17), 7905-7911 (2018)
19. A study of planar anchor groups for graphene-based single-molecule electronics. S Bailey, D Visontai, CJ Lambert, MR Bryce, H Frampton, D Chappell, J. *Chem. Phys.* 140 (5), 054708 (2014)
20. Theory of the arrangement of cells in a network. CJ Lambert, DL Weaire, *Metallography* 14 (4), 307-318 (1981)
21. Anchor groups for graphene-porphyrin single-molecule transistors. Bart Limburg, James O. Thomas, Gregory Holloway, Hatef Sadeghi, Sara Sangtarash, Jonathan Cremers, Akimitsu Narita, Klaus Müllen, Colin J. Lambert, G. Andrew D. Briggs, Jan Mol, and Harry L. Anderson, *Advanced Functional Materials* 28 (45), 1803629 (2018)
22. Robust graphene-based molecular devices. Maria El Abbassi, Sara Sangtarash, Xunshan Liu, Mickael Lucien Perrin, Oliver Braun, Colin J. Lambert , Herre Sjoerd Jan van der Zant, Shlomo Yitzchaik, Silvio Decurtins, Shi-Xia Liu, Hatef Sadeghi and Michel Calame, *Nature Nanotechnology* 14 (10), 957-961 (2019)
23. Low-frequency noise in graphene tunnel junctions. Pawel Puczarski, Qingqing Wu, Hatef Sadeghi, Songjun Hou, Amin Karimi, Colin J. Lambert, G. Andrew D. Briggs and Jan A. Mol, *ACS Nano* 12 (9), 9451-9460 (2018)
24. Bottom-up synthesis of nitrogen-doped porous graphene nanoribbons. Rémy Pawlak, Xunshan Liu, Silviya Ninova, Philipp D'Astolfo, Carl Drechsel,

- Robert Häner, Silvio Decurtins, Hatef Sadeghi, Colin J. Lambert, Ulrich Aschauer, Shi-Xia Liu, and Ernst Meyer, *J. Am. Chem. Soc.* 142 (29), 12568-12573 (2020)
25. Hexagonal-boron nitride substrates for electroburnt graphene nanojunctions. H Sadeghi, S Sangtarash, C Lambert, *Physica E: Low-dimensional Systems and Nanostructures* 82, 12-15 (2026)
26. Conformation dependence of molecular conductance: chemistry versus geometry. C. M. Finch, S. Sirichantaropass, S. W. Bailey, I. M. Grace, V. M. Garcia-Suarez, C. J. Lambert, *J. Phys.: Condensed Matter* 20 (2), 022203 (2007)
27. Turning the Tap: Conformational Control of Quantum Interference to Modulate Single-Molecule Conductance. Feng Jiang, Douglas I. Trupp, Norah Algethami, Haining Zheng, Wenxiang He, Afaf Alqorashi, Chenxu Zhu, Chun Tang, Ruihao Li, Junyang Liu, Hatef Sadeghi, Jia Shi, Ross Davidson, Marcus Korb, Alexandre N. Sobolev, Masnun Naher, Sara Sangtarash, Paul J. Low, Wenjing Hong, Colin J. Lambert, *Angewandte Chemie* 131 (52), 19163-19169 (2019)
28. Connectivity dependence of Fano resonances in single molecules. AK Ismael, I Grace, CJ Lambert, *Phys. Chem. Chem. Phys.* 19 (9), 6416-6421 (2017)
29. Searching the hearts of graphene-like molecules for simplicity, sensitivity, and logic. Sara Sangtarash, Cancan Huang, Hatef Sadeghi, Gleb Sorohhov, Jürg Hauser, Thomas Wandlowski, Wenjing Hong, Silvio Decurtins, Shi-Xia Liu, Colin J Lambert. *J. Am. Chem. Soc.* 137 (35), 11425-11431 (2015)

30. A magic ratio rule for beginners: a chemist's guide to quantum interference in molecules. CJ Lambert, SX Liu, *Chemistry—A European Journal* 24 (17), 4193-4201 (2018)
31. Phonon-mediated thermal conductance of mesoscopic wires with rough edges. A Kambili, G Fagas, VI Fal'ko, CJ Lambert *Phys. Rev. B-Condensed Matter* 60 (23), 15593-15596 (1999)
32. Cross-plane enhanced thermoelectricity and phonon suppression in graphene/MoS<sub>2</sub> van der Waals heterostructures. H Sadeghi, S Sangtarash, CJ Lambert *2D Materials* 4 (1), 015012 (2016)
33. Suppression of phonon transport in molecular Christmas trees. M Famili, I Grace, H Sadeghi, CJ Lambert, *ChemPhysChem* 18 (10), 1234-1241 (2017)
34. Functionalization mediates heat transport in graphene nanoflakes, Haoxue Han, Yong Zhang, Zainelabideen Y Mijbil, Hatef Sadeghi, Yuxiang Ni, Shiyun Xiong, Kimmo Saaskilahti, Steven Bailey, Yuriy A Kosevich, Johan Liu, Colin J Lambert, Sebastian Volz, *Nature Communications* 7 11281 (2016)
35. Thermal transport through single molecule junctions. N. Mosso, H. Sadeghi, A. Gemma, S. Sangtarash, C. Lambert, and B. Gotsmann, *Nano Letters* 19 (11) 7614-7622 (2019)
36. Single-channel conductance of H<sub>2</sub> molecules attached to platinum or palladium electrodes. VM García-Suárez, AR Rocha, SW Bailey, CJ Lambert, S Sanvito, J Ferrer, *Phys. Rev. B* 72 (4), 045437 (2005)

37. Optimized basis sets for the collinear and non-collinear phases of iron. VM García-Suárez, CM Newman, CJ Lambert, JM Pruneda, J Ferrer, J. Phys.: Condensed Matter 16 (30), 5453 (2004)
38. Boundary conditions for quasiclassical equations in the theory of superconductivity. CJ Lambert, R Raimondi, V Sweeney, AF Volkov, Phys. Rev. B 55 (9), 6015 (1997)
39. Andreev reflections and magnetoresistance in ferromagnet-superconductor mesoscopic structures, VI Fal'Ko, CJ Lambert, AF Volkov, Journal of Experimental and Theoretical Physics Letters 69 (7), 532-538 (1999)
40. Andreev scattering, universal conductance fluctuations and phase periodic transport. VC Hui, CJ Lambert Europhysics Letters 23 (3), 203 (1993)
41. Superconductivity-induced phase-periodic transport in nanoscale structures. M Leadbeater, CJ Lambert, Phys. Rev. B 56 (2), 826 (1997)
42. Quantum resonances of weakly linked, mesoscopic, superconducting dots. CJ Lambert, A Martin, J. of Phys.: Condensed Matter 6 (16), L221 9 (1994)
43. Quantum interference and nonequilibrium Josephson currents in molecular Andreev interferometers. NL Plaszkó, P Rakyta, J Cserti, A Kormányos, CJ Lambert, Nanomaterials 10 (6), 1033 (2020)
44. Magic number theory of superconducting proximity effects and Wigner delay times in graphene-like molecules. P. Rakyta, A. Alanazy, A. Kormányos, Z. Tajkov, G. Kukucska, J. Koltai, S. Sangtarash, H. Sadeghi, J. Cserti and C.J. Lambert, J. Phys. Chem C 123 6812 (2019)

45. Enhancing the thermoelectric figure of merit in engineered graphene nanoribbons. H Sadeghi, S Sangtarash, CJ Lambert, *Beilstein Journal of nanotechnology* 6 (1), 1176-1182 (2015)
46. High-performance thermoelectricity in edge-over-edge zinc-porphyrin molecular wires. M Noori, H Sadeghi, CJ Lambert *Nanoscale* 9 (16), 5299-5304 (2017)
47. Thermoelectric Properties of 2, 7-Dipyridylfluorene Derivatives in Single-Molecule Junctions. Gilles Yzambart, Laura Rincón-García, Alaa A. Al-Jobory, Ali K. Ismael, Gabino Rubio-Bollinger, Colin J. Lambert, Nicolás Agraït, Martin R. Bryce, *J. Phys.Chem. C* 122 (48), 27198-27204 (2018)
48. Thermoelectricity in vertical graphene-C<sub>60</sub>-graphene architectures. Q Wu, H Sadeghi, VM García-Suárez, J Ferrer, CJ Lambert, *Scientific reports* 7 (1), 1-8 (2017)
49. Improvement of the Seebeck coefficient of PEDOT: PSS by chemical reduction combined with a novel method for its transfer using free-standing thin films. Massonnet, N., Carella, A., Jaudouin, O., Rannou, P., Laval, G., Celle, C., & Simonato, J. P., *Journal of Materials Chemistry C*, 2(7), 1278-1283 (2014)
50. Molecular design and control of fullerene-based bi-thermoelectric materials, Laura Rincón-García, Ali K. Ismael, Charalambos Evangelis, Iain Grace, Gabino Rubio-Bollinger, Kyriakos Porfyrakis, Nicolás Agraït, and Colin J. Lambert, *Nature Materials*, 15, 289–293 (2016)

51. Strain-induced bi-thermoelectricity in tapered carbon nanotubes. L.A.A. Algharagholy, T. Pope, and C.J. Lambert, *J. Phys. Condens. Matt.* 30 105304 (2018)
52. Does a Cyclopropane Ring Enhance the Electronic Communication in Dumbbell-Type C60 Dimers? La Rosa, A.; Gillemot, K.; Leary, E.; Evangeli, C.; González, M. T.; Filippone, S.; Rubio-Bollinger, G.; Agraït, N.; Lambert, C. J.; Martín, N., *J. Org. Chem.* 79 (11), 4871-4877 (2014)
53. Connectivity-driven bi-thermoelectricity in heteroatom-substituted molecular junctions. Sara Sangtarash, Hatf Sadeghi and Colin J. Lambert, *Phys Chem Chem Phys* 20, 9630 - 9637 (2018)
54. Oscillating chiral currents in nanotubes: A route to nanoscale magnetic test tubes. CJ Lambert, SWD Bailey, J Cserti, *Phys. Rev. B* 78 (23), 233405 (2008)
55. Thermoelectricity in vertical graphene-C 60-graphene architectures. Q Wu, H Sadeghi, VM García-Suárez, J Ferrer, CJ Lambert, *Scientific reports* 7 (1), 1-8 (2017)
56. Quantum interference mediated vertical molecular tunneling transistors. Chuancheng Jia, Marjan Famili, Marco Carlotti, Iain M. Grace, Yuan Liu, Peiqi Wang, Ziyang Feng, Yiliu Wang, Mengning Ding, Jian Guo, Xiang Xu, Yu Huang, Ryan C. Chiechi, Colin J. Lambert and Xiangfeng Duan, *Science advances* 4 (10), eaat8237 (2018)
57. Self-assembled molecular-electronic films controlled by room temperature quantum interference. Marjan Famili, Chuancheng Jia, Xunshan Liu, Peiqi Wang, Iain M. Grace, Jian Guo, Yuan Liu, Ziyang Feng, Yiliu Wang, Zipeng

Zhao, Silvio Decurtins, Robert Häner, Yu Huang, Shi-Xia Liu, Xiangfeng Duan and Colin J. Lambert, *Chem* 5 (2), 474-484 (2019)

58. Scale-up of room-temperature constructive quantum interference from single molecules to self-assembled molecular-electronic films. Xintai Wang, Troy L. R. Bennett, Ali Ismael, Luke A. Wilkinson, Joseph Hamill, Andrew J. P. White, Iain M. Grace, Tim Albrecht, Benjamin J. Robinson, Nicholas J. Long, Lesley F. Cohen and Colin J. Lambert, *J. Am. Chem. Soc.* 142 (19), 8555-8560 (2020)
59. P. Hohenberg and W. Kohn, Inhomogeneous electron gas. *Physical review*, 136(3B), B864. (1964)
60. Self-consistent equations including exchange and correlation effects. W. Kohn and L.J. Sham, *Physical review*, 140(4A), A1133. (1965)
61. Self-interaction correction to density-functional approximations for many-electron systems. J.P. Perdew, J. P. and A. Zunger, *Physical Review B*, 23(10), 5048. (1981)
62. Generalized gradient approximation made simple. J.P. Perdew, K. Burke, and M. Ernzerhof, *Physical Review letters*, 77(18), 3865. (1996)
63. The SIESTA method for ab initio order-N materials simulation. J.M. Soler, E. Artacho, J.D. Gale, A. García, J. Junquera, P. Ordejón, and D. Sánchez-Portal, *Journal of Physics: Condensed Matter*, 14(11), 2745. (2002)

## Chapter 2

### 2. Density Functional Theory

This chapter presents the formalism behind density functional theory (DFT) along with general details of the DFT code SIESTA which is used in all the electronic structure calculations in this thesis. These calculations represent the first step of the procedure to obtain the electron transport properties of the molecule. However, since the Hamiltonian extracted is only of the isolated molecule, it still has to be connected to semi-infinite leads which in theory produces an infinite problem. This second step will be discussed in detail in the following chapter.

#### 2.1 Introduction

DFT is frequently used by scientists in the fields of physics and chemistry for investigating the ground-state characteristics of interacting multiple particle systems such as atoms, molecules and crystals. Through DFT, the many-body system is transformed into one that consists of non-interacting fermions within an effective field. Put differently, it is possible to describe the electronic characteristics of a system with multiple interacting particles as a function of the system's ground-state density [1, 2]. The significance of DFT was affirmed in 1998 with the decision to present Walter Kohn with the Nobel Prize in Chemistry for his role in developing density functional theory. The DFT methodology has good reliability and is applicable to various different molecular systems, where a large body of literature including articles and books has

described the principles and applications of DFT in great detail [1-6]. The foundation of DFT was the Thomas-Fermi model that was developed in the 1920s, which described the fundamental steps required for obtaining the density functional for overall energy on the basis of wave functions [1, 6-8]. This model was enhanced by Hartree, Dirac, Fock and Slater approximately 40 years after the work published by Thomas and Fermi. DFT itself was subsequently established by the Hohenberg-Kohn theorems and the Kohn-Sham technique [1, 3, 4, 7-11].

The primary objective of this chapter is to briefly introduce DFT and to describe the main formalism as an approach for determining a solution to the non-relativistic multiple-particle time-independent Schrödinger equation (TISE). This allows us to in principle determine the characteristics of a system with multiple electrons by utilising functionals of the electron density. The DFT code ‘SIESTA’ will also be briefly summarised, as it is employed frequently throughout this work as a theoretical tool for optimising the molecular structures.

## 2.2 The Schrödinger Equation and Variational Principle

It is possible to describe a general, non-relativistic system with multiple particles using the time-independent Schrödinger equation:

$$H\Psi_i(\vec{r}_1, \vec{r}_2, \dots, \vec{r}_N, \vec{R}_1, \vec{R}_2, \dots, \vec{R}_M) = E_i\Psi_i(\vec{r}_1, \vec{r}_2, \dots, \vec{r}_N, \vec{R}_1, \vec{R}_2, \dots, \vec{R}_M) \quad (2.1)$$

In this equation,  $H$  denotes the Hamiltonian operator of a system comprised of  $N$  electrons and  $M$  nuclei, and describes the interaction between particles.  $\Psi_i$  represents the wave function of the system’s  $i^{\text{th}}$  state, with energy  $E_i$ . This system’s Hamiltonian operator can then be written in the form of a sum of five terms shown by [2, 3, 12]:

$$\begin{aligned}
H = & \overbrace{-\frac{\hbar^2}{2m_e} \sum_{i=1}^N \nabla_i^2}^{T_e} - \overbrace{\frac{\hbar^2}{2m_n} \sum_{n=1}^M \nabla_n^2}^{T_n} - \overbrace{\frac{1}{4\pi\epsilon_0} \sum_{i=1}^N \sum_{n=1}^M \frac{1}{|\vec{r}_i - \vec{R}_n|} Z_n e^2}^{U_{en}} \\
& + \overbrace{\frac{1}{4\pi\epsilon_0} \frac{1}{2} \sum_{i=1}^N \sum_{i \neq j}^N \frac{e^2}{|\vec{r}_i - \vec{r}_j|}}^{U_{ee}} \\
& + \overbrace{\frac{1}{4\pi\epsilon_0} \frac{1}{2} \sum_{n=1}^M \sum_{n \neq n'}^M \frac{1}{|\vec{R}_n - \vec{R}_{n'}|} Z_n Z_{n'} e^2}^{U_{nn}}
\end{aligned} \tag{2.2}$$

where  $i$  and  $j$  label the  $N$  electrons,  $n$  and  $n'$  run over the  $M$  nuclei within the system,  $m_e$  and  $m_n$  denote the mass of the electron and nucleus respectively, and  $e$  and  $Z_n$  describe the electron and nuclear charge, respectively. Furthermore,  $\vec{r}_i$  and  $\vec{R}_n$  denote the respective positions of the electrons and nuclei, while  $\nabla_i^2$  denotes the Laplacian operator which in Cartesian coordinates is defined as

$$\nabla_i^2 = \frac{\partial^2}{\partial x_i^2} + \frac{\partial^2}{\partial y_i^2} + \frac{\partial^2}{\partial z_i^2}$$

In equation (2.2), the first two terms,  $T_e$  and  $T_n$  denote the kinetic energy of electrons and nuclei respectively. The remaining three terms represent the potential component of the Hamiltonian. The attractive electrostatic interaction between the nuclei and electrons is defined by  $U_{en}$ . The electron-electron interaction,  $U_{ee}$  and nuclear-nuclear interaction,  $U_{nn}$ , describe the repulsive component of the potential [1, 3, 6, 9, 13].

It is possible to apply the Born-Oppenheimer approximation, also known as the clamped nuclei approximation, where the nuclei are regarded as being fixed in position. This is

justified since approximately 99.9% of the atom's total mass is condensed within the nucleus (for instance, the weight of a hydrogen nucleus is around 1,800 times greater compared to an electron). In such a situation, when the treated atoms' nuclei are fixed, they have no kinetic energy and will play no further role in the complete wave function. This assumption implies that the Hamiltonian is reduced to a simpler form, defined as the electronic Hamiltonian  $H_{ele}$ , which it is possible to rewrite according to the fixed nuclear picture as [1, 3, 6, 13-15]:

$$\begin{aligned}
 H_{ele} = & \overbrace{-\frac{\hbar^2}{2m_e} \sum_{i=1}^N \nabla_i^2}^{T_e} - \overbrace{\frac{1}{4\pi\epsilon_0} \sum_{i=1}^N \sum_{n=1}^M \frac{1}{|\vec{r}_i - \vec{R}_n|} Z_n e^2}_{U_{en}} \\
 & + \overbrace{\frac{1}{4\pi\epsilon_0} \frac{1}{2} \sum_{i=1}^N \sum_{i \neq j}^N \frac{e^2}{|\vec{r}_i - \vec{r}_j|}}^{U_{ee}} + \overbrace{\frac{1}{4\pi\epsilon_0} \frac{1}{2} \sum_{i=1}^M \sum_{n \neq n'}^M \frac{Z_n Z_{n'} e^2}{|\vec{R}_n - \vec{R}_{n'}|}}^{U_{nn}} \quad (2.3)
 \end{aligned}$$

where  $U_{nn}$  represents a constant. For the given system, the Schrödinger equation for 'clamped-nuclei' is

$$H_{ele} \Psi_{ele} = E_{ele} \Psi_{ele} \quad (2.4)$$

where  $\Psi_{ele}$  is dependent on the coordinates of the electrons only, with the nuclear component only entering parametrically. Hence, the overall energy  $E_{total}$  is calculated by summing  $E_{ele}$  and the constant nuclear repulsion term:

$$E_{total} = E_{ele} + U_{nn} \quad (2.5)$$

In itself, a wave function is not a physically observable quantity. However, its modulus squared, in the form

$$|\Psi(\vec{r}_1, \vec{r}_2, \dots, \vec{r}_N)|^2 d\vec{r}_1 d\vec{r}_2 \dots d\vec{r}_N \quad (2.6)$$

determines the probability that electrons  $1, 2, \dots, N$  will be detected in the volume elements  $d\vec{r}_1 d\vec{r}_2 \dots d\vec{r}_N$ . Since electrons cannot be distinguished, the probability cannot change if the coordinates of two given electrons (in this case  $i$  and  $j$ ) are interchanged [12]:

$$|\Psi(\vec{r}_1, \vec{r}_2, \dots, \vec{r}_i, \vec{r}_j, \dots, \vec{r}_N)|^2 = |\Psi(\vec{r}_1, \vec{r}_2, \dots, \vec{r}_j, \vec{r}_i, \dots, \vec{r}_N)|^2 \quad (2.7)$$

Because electrons are fermions with a half spin, it follows that  $\Psi$  is anti-symmetric in terms of the swapping of the spin and spatial coordinates of two given electrons:

$$\Psi(\vec{r}_1, \vec{r}_2, \dots, \vec{r}_i, \vec{r}_j, \dots, \vec{r}_N) = -\Psi(\vec{r}_1, \vec{r}_2, \dots, \vec{r}_j, \vec{r}_i, \dots, \vec{r}_N) \quad (2.8)$$

Based on the probability interpretation of the wave function, it is convenient to choose the integral of equation (2.6) over the complete range of all variables is equal to one. This implies that the likelihood that an N-electron will be found at any point in space must be precisely unity,

$$\int \dots \int |\Psi(\vec{r}_1, \vec{r}_2, \dots, \vec{r}_N)|^2 d\vec{r}_1 d\vec{r}_2 \dots d\vec{r}_N = 1 \quad (2.9)$$

A wave function that satisfies equation (2.9) is considered to be normalised.

Due to the fact that the Schrödinger equation cannot be solved precisely, numerous theories have been proposed to find approximate solutions, beginning with Hartree, Hartree-Fock and others.

The majority of such theories were founded on a significant theoretical principle defined as the variational principle of the wave function [1, 2, 5, 6, 12].

In simple terms, this principle guides the process of searching for solutions by utilising appropriate trial wave functions  $\Psi_{\text{Tri}}$ . The principle is beneficial for studying the ground state, but offers minimal benefit for studying excited states. In cases where the state of the system is  $\Psi_{\text{Tri}}$ , the energy's expectation value is calculated as [1, 3, 6, 9]:

$$\langle E_{\text{Tri}} \rangle = \frac{\int \Psi_{\text{Tri}} H \Psi_{\text{Tri}}^* d\vec{r}}{\int \Psi_{\text{Tri}} \Psi_{\text{Tri}}^* d\vec{r}} \quad (2.10)$$

equation (2.10) contains the variational principle. The variational principle states that the energy expectation value of any  $\Psi_{\text{Tri}}$  (trial wave function) represents an upper bound to the actual ground-state energy. Where  $\Psi_{\text{Tri}}$  is normalised on the basis of equation (2.9), and  $\Psi_{\text{Tri}}$  is equal to the ground state ( $\Psi_{\text{Tri}} = \Psi_{\text{GS}}$ ), this implies  $E_{\text{Tri}}$  equates to the precise ground state energy  $E_{\text{GS}}$ , which means that equation (2.10) can now be rewritten for the ground state as:

$$\langle E_{\text{GS}} \rangle = \int \Psi_{\text{GS}} H \Psi_{\text{GS}}^* d\vec{r} \quad (2.11)$$

Thus, the normalised  $\Psi_{\text{Tri}}$  can indicate that either  $E_{\text{Tri}} > E_{\text{GS}}$  or  $E_{\text{Tri}} = E_{\text{GS}}$ . Hence, the optimal selection of  $\Psi_{\text{Tri}}$  is the one where the  $E_{\text{Tri}}$  is minimised [3, 4, 6].

### 2.3 The Hohenberg-Kohn Theorems

DFT is founded on the theorems of Hohenberg and Kohn, who in 1964 validated the use of the electron density  $n(\vec{r})$  for calculating ground state energy [6,10, 17, 18]:

According to Theorem (1), the electron density can be uniquely calculated for an interacting multiple particle system that has an applied external potential  $V_{\text{ext}}(\vec{r})$ . This implies that it is possible to use the density  $n(\vec{r})$  rather than the potential as a function that uniquely characterises the system. Specifically, the ground state density  $n_{\text{GS}}(\vec{r})$ ,

provides a unique determination of the potential up to an arbitrary constant [6, 10, 17, 19].

According to Proof (1), which was originally presented by of Hohenberg and Kohn, the theorem has been proven for densities whose ground states are non-degenerate, where the proof was elementary and by contradiction [17]. Two differing external potentials  $V_{\text{ext}}(\vec{r})_{(1)}$  and  $V_{\text{ext}}(\vec{r})_{(2)}$  are considered that differ by more than a constant and produce an identical ground state density  $n_{\text{GS}}(\vec{r})$ . It is evident that the potentials relate to different Hamiltonians, namely  $H_{\text{ext}}[(\vec{r})]_{(1)}$  and  $H_{\text{ext}}[(\vec{r})]_{(2)}$ , which generate unique wave functions, namely  $\Psi_{\text{ext}}[(\vec{r})]_{(1)}$  and  $\Psi_{\text{ext}}[(\vec{r})]_{(2)}$ .

As the ground state is identical, using the variational principle, which indicates that a wave function does not exist with less energy than that of  $\Psi_{\text{ext}}[(\vec{r})]_{(1)}$  for  $H_{\text{ext}}[(\vec{r})]_{(1)}$ , we have:

$$\langle E_{(1)} \rangle = \int \Psi_{(1)} H_{(1)} \Psi_{(1)}^* d\vec{r} < \int \Psi_{(2)} H_{(2)} \Psi_{(2)}^* d\vec{r} \quad (2.12)$$

When the ground-state is non-degenerate, and as a result the two Hamiltonians' ground state densities are exactly the same, equation (2.12) is transformed to:

$$\int \Psi_{(2)} H_{(1)} \Psi_{(2)}^* d\vec{r} = \overbrace{\int \Psi_{(2)} H_{(2)} \Psi_{(2)}^* d\vec{r}}^{\langle E_{(2)} \rangle} + \int \{ [V_{\text{ext}}(\vec{r})]_{(1)} - [V_{\text{ext}}(\vec{r})]_{(2)} \} n_{\text{GS}}(\vec{r}) d\vec{r} \quad (2.13)$$

When the labels in equation (2.13) are exchanged, this gives:

$$\int \Psi_{(1)} H_{(2)} \Psi_{(1)}^* d\vec{r} = \overbrace{\int \Psi_{(1)} H_{(1)} \Psi_{(1)}^* d\vec{r}}^{\langle E_{(1)} \rangle} + \int \{ [V_{ext}(\vec{r})]_{(2)} - [V_{ext}(\vec{r})]_{(1)} \} n_{GS}(\vec{r}) d\vec{r} \quad (2.14)$$

The addition of equation (2.13) to equation (2.14) yields

$$\langle E_{(1)} \rangle + \langle E_{(2)} \rangle < \langle E_{(2)} \rangle + \langle E_{(1)} \rangle \quad (2.15)$$

which evidently reveals a contradiction. Hence, the proof of the theorem has been shown by *reductio ad absurdum*.

A variational ansatz is provided by Theorem 2 to obtain  $n(\vec{r})$ ; in other words, it searches for the  $n(\vec{r})$  which causes the energy to be minimised. Put differently, it implies that a universal functional can be defined for the energy,  $E[n(\vec{r})]$ . The particular system's precise ground state energy represents the global minimum value of this functional, and the density  $n(\vec{r})$  which causes the functional to be minimised is the precise ground state density  $n_{GS}(\vec{r})$  [1, 6, 10, 17, 19].

According to Proof (2), the first theorem indicates that the system's overall energy is a functional of the density  $n(\vec{r})$  and is formulated as

$$E_{total}[n(\vec{r})] = \overbrace{T_{int}[n(\vec{r})] + U_{ee}[n(\vec{r})]}^{F_{H-K}[n(\vec{r})]} + \int V_{ext}(\vec{r}) n(\vec{r}) d\vec{r} \quad (2.16)$$

$\underbrace{U_{ee}[n(\vec{r})]}_{\substack{=zero, \text{ for} \\ \text{non-interacting} \\ \text{system}}}$

In equation (2.16) the first two terms ( $F_{H-K}[n(\vec{r})]$ ) represent the kinetic energy ( $T_{int}$ ) and electron-electron interaction energy ( $U_{ee}$ ), which are treated in the same manner for the entire system. Therefore  $F_{H-K}[n(\vec{r})]$  is considered a universal functional that has

been defined as the ultimate goal of density functional theory [12]. If the assumption is made that the system is in the ground state, the energy can be uniquely defined based on the ground state density  $n_{GS}(\vec{r})$ :

$$\langle E_{GS} \rangle = \langle E[n_{GS}(\vec{r})] \rangle = \int \Psi_{GS} H_{GS} \Psi_{GS}^* d\vec{r} \quad (2.17)$$

On the basis of the variational principle, the ground state energy, corresponding to the ground state density, represents the minimum energy and it follows that all other densities will yield increased energy:

$$\begin{aligned} \langle E_{GS} \rangle = \langle E[n_{GS}(\vec{r})] \rangle &= \int \Psi_{GS} H_{GS} \Psi_{GS}^* d\vec{r} < \int \Psi H \Psi^* d\vec{r} \\ &= \langle E[n(\vec{r})] \rangle = \langle E \rangle \end{aligned} \quad (2.18)$$

After the functional  $F_{H-K}[n(\vec{r})]$  has been determined, the overall energy (equation (2.16) ) can be minimised with respect to variations in the density function, which facilitates the process of precisely identifying the system's ground state characteristics. (It is important to consider that in the majority of practical calculations, the ground state energy will be found by direct minimisation, but this can be achieved using the less complex process according to Kohn-Sham).

## 2.4 The Kohn-Sham Method and Self-Consistent Field

It was observed by Kohn and Sham that the theorems of Hohenberg and Kohn can be applied to systems that are either interacting or non-interacting. One of the benefits of a non-interacting system compared to an interacting system is that it is easier to find the ground-state energy in the former. They developed a method to take advantage of this

to circumvent the issue of multiple interacting particles. This forms the basis of density functional theory.

In 1965, Kohn Sham proposed one of the benefits of the non-interacting system compared to the interacting system is that it is easier to find the ground-state energy in the former. In 1965, Kohn and Sham [11] proposed that the system's original Hamiltonian could be substituted with an effective Hamiltonian ( $H_{\text{eff}}$ ) of a non-interacting system in an effective external potential  $V_{\text{eff}}(\vec{r})$ , which generates the identical ground state density found in the original system. As there is no definitive method by which this is calculated, the Kohn-Sham technique is regarded as an ansatz, but the process of solving it is much less complex compared to the interacting problem. The foundation of the Kohn-Sham technique is the Hohenberg-Kohn universal density functional [6, 9, 10, 20]:

$$F_{H-K}[n(\vec{r})] = T_{\text{int}}[n(\vec{r})] + U_{ee}[n(\vec{r})] \quad (2.19)$$

In contrast to (2.16), the Kohn-Sham ansatz  $F_{K-S}[n(\vec{r})]$ , for the energy functional is formulated as

$$F_{K-S}[n(\vec{r})] = T_{\text{non}}[n(\vec{r})] + E_{\text{Hart}}[n(\vec{r})] + \int V_{\text{ext}}(\vec{r}) n(\vec{r}) d\vec{r} + E_{\text{xc}}[n(\vec{r})] \quad (2.20)$$

where  $T_{\text{non}}$  denotes the non-interacting system's kinetic energy, which differs from that of  $T_{\text{int}}$  (for the interacting system) from equation (2.16), and  $E_{\text{Hart}}$  represents the classical self-interaction or electrostatic energy of the electron gas, which is related to the density  $n(\vec{r})$ . The fourth term,  $E_{\text{xc}}$ , is the exchange-correlation energy functional, and is formulated as

$$E_{xc}[n(\vec{r})] = F_{H-K}[n(\vec{r})] - \frac{1}{2} \int \frac{n(\vec{r}_1)n(\vec{r}_2)}{|\vec{r}_1 - \vec{r}_2|} d\vec{r}_1 d\vec{r}_2 - T_{non}[n(\vec{r})] \quad (2.21)$$

It is possible to trivially cast the first three terms of equation (2.20) into functional form. In contrast,  $E_{xc}$  does not have a precise functional form. In recent years, researchers have focused their efforts on searching for ever improving approximations to  $E_{xc}$ . Presently, the functionals are capable of investigating and predicting the physical characteristics of a broad range of molecules and solid-state systems. For the latter three terms in equation (2.20), functional derivatives are taken for the purpose of constructing the effective individual particle potential  $V_{eff}(\vec{r})$ :

$$V_{eff}(\vec{r}) = V_{ext}(\vec{r}) + \frac{\partial E_{Hart}[n(\vec{r})]}{\partial n(\vec{r})} + \frac{\partial E_{xc}[n(\vec{r})]}{\partial n(\vec{r})} \quad (2.22)$$

Subsequently, the obtained potential can be used to generate the single particle Hamiltonian,

$$H_{K-S} = T_{non} + V_{eff} \quad (2.23)$$

Through the use of this Hamiltonian, the Schrödinger equation is transformed into:

$$[T_{non} + V_{eff}]\Psi_{K-S} = E\Psi_{K-S} \quad (2.24)$$

Equation (2.24) is known as the Kohn-Sham equation. The ground state density  $n_{GS}^{K-S}(\vec{r})$  corresponds to the ground state wave function  $\Psi_{GS}^{K-S}$ , which accordingly causes the Kohn-Sham functional to be minimised subject to the orthonormalization constraints  $\langle \Psi_i | \Psi_j \rangle = \delta_{ij}$  [1, 4, 14, 21].

To solve the Kohn-Sham equation in density functional theory, a self-consistent field process is used. To illustrate this, assume for sake of argument that it is possible to

precisely determine the functionals  $E_{\text{Hart}}$  and  $E_{\text{xc}}$ . The problem then becomes the inability to calculate  $V_{\text{eff}}$  without knowing the right ground state density, which cannot be derived from the Kohn-Sham wave functions prior to solving equation (2.2.9) using the right  $V_{\text{eff}}$ . Hence, a Self-Consistent Field (SCF) cycle is conducted to enable this circular problem to be solved [3, 12, 22] as illustrated in Figure 2.1.

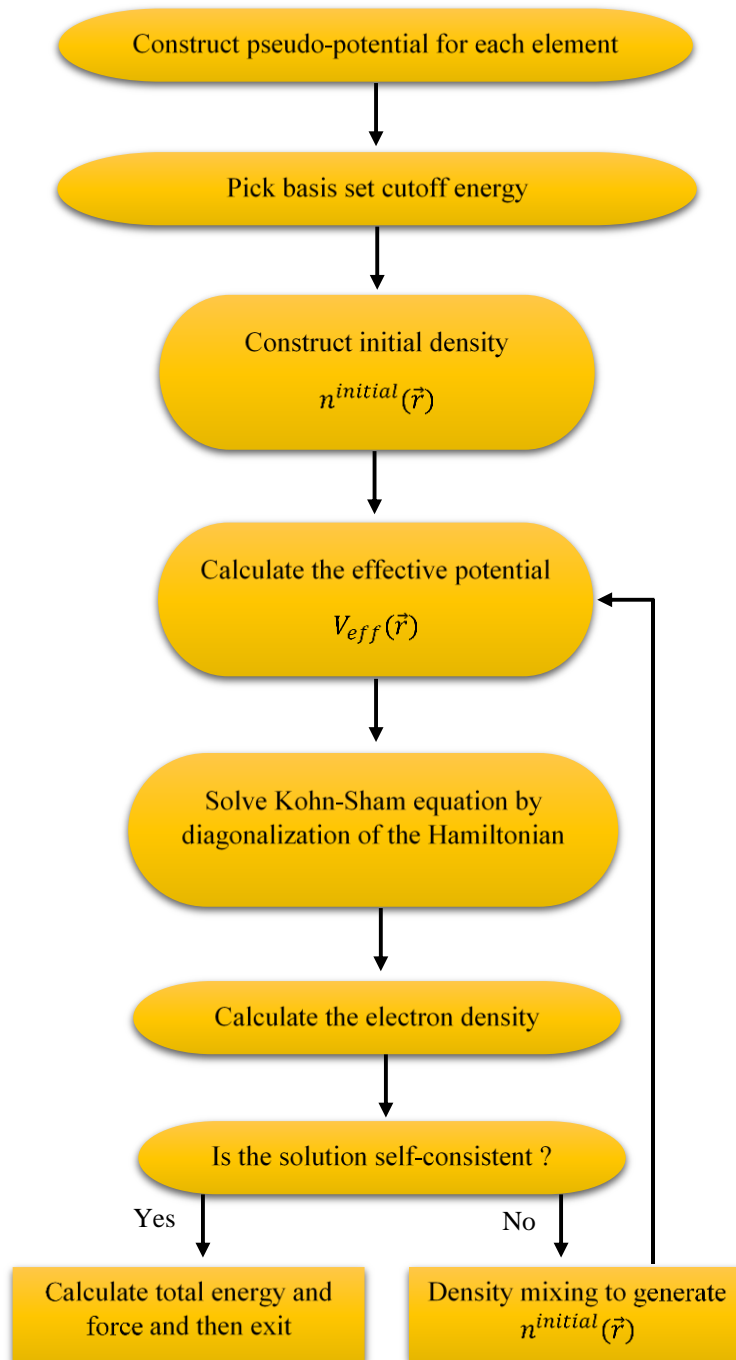


Figure 2.1 Flowchart of the self-consistent DFT cycle.

As shown in Figure 2.1, the initial stage involves the generation of the pseudo-potential, discussed further in section 2.8, which is representative of the electrostatic interaction

that occurs between the valence electrons and nuclei and core electrons. This is followed by the formation of the necessary basis set using a specified energy cutoff that is introduced to the basis set; this stage enables the density functional quantities to be expanded.

Evidently, if the density is identified, the energy functional is completely determined. A trial electronic density  $n^{\text{initial}}(\vec{r})$  is proposed as a provisional estimate. This provisional estimate is used for calculating the quantity

$$G = E_{\text{Hart}}[n^{\text{initial}}(\vec{r})] + E_{\text{xc}}[n^{\text{initial}}(\vec{r})] \quad (2.25)$$

This is followed by the calculation of  $\frac{\partial G}{\partial n^{\text{initial}}(\vec{r})}$  as well as the effective potential  $V_{\text{eff}}$ .

The latter is used for solving the Kohn-Sham equation (2.24), by specifying the electron Hamiltonian. After being obtained, the Hamiltonian is then diagonalised to give the wavefunctions  $\Psi_{\text{K-S}}$ , which in turn determine the new electron density  $n^{\text{new}}(\vec{r})$ . Ideally, this  $n^{\text{new}}(\vec{r})$  will be nearer to the actual ground state density.

In terms of self-consistency, if this new modified electron density  $n^{\text{new}}(\vec{r})$  is in numerical agreement with the density  $n^{\text{initial}}(\vec{r})$  used for constructing the Hamiltonian when the SCF cycle began, then the end of the loop has been reached. The loop is then exited and all the intended converged quantities are calculated, including the overall energy, the electronic band structure, and density of states. Alternatively, if the aforementioned density  $n^{\text{new}}(\vec{r})$  is not in agreement with the initial density  $n^{\text{initial}}(\vec{r})$ , a new input density is generated and a further SCF cycle is initiated in which a new Hamiltonian that is dependent on the input density is generated and after diagonalisation the output density is computed. The process continues until self-consistency is verified [3, 17, 23].

The Kohn-Sham method demonstrates that it is possible to precisely map a complex system comprised of many interacting particles onto a basic series of non-interacting particle equations when the exchange correlation functional has been determined. Nevertheless, as we do not precisely know the exchange-correlation functional, some approximation is necessary.

## 2.5 The Exchange-Correlation Functional

Although DFT is a proven approach with high reliability, the kinetic energy functional and exchange-correlation functional are still approximations. Extensive research has been conducted with the aim of determining expressions for such functionals that exhibit good reliability. The exchange-correlation functional approximations that are most frequently used are the Local Density Approximation (LDA), which is purely dependent on the density, as well as the more complex Generalised Gradient Approximation (GGA), which incorporates the density's derivative and additionally includes data pertaining to the environment, implying that it is semi-local.

## 2.6 Local Density Approximation (LDA)

According to the Kohn-Sham approach, it is possible to calculate the functional  $E_{xc}$  within a homogenous electron gas for the purpose using this less complex system to approximate the true many body particle problem [11]. It was shown by Kohn-Sham that if a system's density varies only gradually, the  $E_{xc}$  functional at point  $\vec{r}$  can be considered to act in a uniform density. Hence, one can represent the  $E_{xc}$  functional via a uniform electron gas  $E_{xc}^{\text{homo}}[n(\vec{r})]$  that has a density  $n(\vec{r})$ . Generally, the LDA is not applicable for systems in which interactions between electrons are dominant.

Using the LDA assumption – i.e. assuming that the density remains constant within the local region surrounding any given position – the exchange-correlation functional has the form [6, 12]:

$$E_{xc}^{LDA}[n(\vec{r})] = \int E_{xc}^{homo}[n(\vec{r})]n(\vec{r})d\vec{r} \quad (2.26)$$

It is possible to divide the exchange-correlation energy  $E_{xc}^{homo}[n(\vec{r})]$  into two separate terms, namely the exchange  $E_x^{homo}[n(\vec{r})]$  and the correlation energies  $E_c^{homo}[n(\vec{r})]$  :

$$E_{xc}^{homo}[n(\vec{r})] = E_x^{homo}[n(\vec{r})] + E_c^{homo}[n(\vec{r})] \quad (2.27)$$

The determination of the exchange terms is performed using an analytical approach; it is widely recognised and has been included in multiple textbooks (see [6, 12]) resulting in

$$E_x^{homo}[n(\vec{r})] = -\frac{3}{4} \left( \frac{3n(\vec{r})}{\pi} \right)^{1/3} \quad (2.28)$$

Although, it is not possible to obtain the correlation energy ( $E_c^{homo}[n(\vec{r})]$ ) using an analytical approach, a precise determination can be made utilising numerical techniques. The most frequent and precise technique was developed by Ceperly and Alder (CA) [24] which uses quantum Monte Carlo simulations. Monte Carlo simulations can be interpreted in various different ways; for instance, the most frequently adopted approach was proposed by Perdew and Zunger (PZ), who succeeded in fitting the numerical data to an analytical expression, which yielded [25,26]:

$$E_c^{homo}[n(\vec{r})] = \left\{ \begin{array}{ll} -0.048 + 0.031 \ln(r_o) - 0.0116 r_o + 0.002 \ln(r_o) & \text{if } r_o < 1 \\ -\frac{0.1423}{(1 + 1.9529 \sqrt{r_o} + 0.3334 r_o)} & \text{if } r_o > 1 \end{array} \right\} \quad (2.29)$$

where  $r_o$  denotes the average radius of the electrons within the homogenous electron gas, and is given by  $\left(\frac{3}{4\pi n}\right)^{1/3}$ .

The LDA is a basic and widely-recognised functional with significant power, and is regarded as being accurate for carbon and graphene nanotubes or in situations where there are no rapid changes in the electronic density. It is anticipated that atoms with d and f orbitals will exhibit larger errors. There are certain shortcomings associated with this functional; for instance, the band gap in insulators and semi-conductors is generally not precise and the error is larger (between 0.5 and 2eV or 10-30%). Hence, it is recommended that better functionals are sought [25, 27, 28].

## 2.7 Generalized Gradient Approximation (GGA)

Although all systems are treated by LDA as being homogenous, this is not usually the case in reality. To account for this situation, the LDA can be extended further by incorporating the density's derivative information within the exchange-correlation functionals. This can only be achieved by incorporating the gradient as well as the higher spatial derivatives of the overall charge density ( $|\nabla n(\vec{r})|$ ,  $|\nabla^2 n(\vec{r})|$ , ...) within the approximation. This type of functional is defined as the generalised gradient approximation (GGA). In this situation, the exchange aspect of the functional does not have a closed expression, which means it must be calculated in combination with correlation contributions utilising numerical techniques. Identical to the LDA, there are

multiple parameterisations for the exchange-correlation energies within the GGA [29-32].

The following section will present a discussion on the functional form that was proposed by Perdew, Burke and Ernzerhof (PBE) [29]. This parameterisation includes two separate expressions, where the first is the exchange  $E_x^{\text{GGA}}[n(\vec{r})]$  and is formulated as:

$$E_x^{\text{GGA}}[n(\vec{r})] = \int n(\vec{r}) E_x^{\text{homo}}[n(\vec{r})] F_x(s) d\vec{r}, \quad (2.30)$$

$$F_x(s) = 1 + \kappa - \frac{\kappa}{(1 + \mu s^2)/\kappa}$$

where  $F_x(s)$  is defined as the enhancement factor,  $\kappa = 0.804$ ,  $\mu = 0.21951$  and  $s = |\nabla n(\vec{r})|/2k_s n(\vec{r})$  denotes the dimensionless density gradient, where  $k_s = \sqrt{\frac{4 k_{\text{T-F}}}{\pi a_0}}$  and  $k_{\text{T-F}} = \frac{(12/\pi)^{1/3}}{\sqrt{r_s}}$  represents the Thomas-Fermi screening wavenumber, while the local Seitz radius is defined as  $r_s$ .

The second expression denotes the correlation energy  $E_c^{\text{GGA}}[n(\vec{r})]$  and is formulated as:

$$E_c^{\text{GGA}}[n(\vec{r})] = \int (E_c^{\text{homo}}[n(\vec{r})] + \chi[n(\vec{r})]) d\vec{r}, \quad (2.31)$$

$$\chi[n(\vec{r})] = \frac{e^2}{a_0} \gamma \ln \left( 1 + \frac{\beta}{\gamma} t^2 \frac{1 + At^2}{1 + At^2 + A^2 t^4} \right),$$

$$A = \frac{\beta}{\gamma} \left[ e^{\left( \frac{E_c^{\text{homo}}[\mathbf{n}(\vec{r})]}{\gamma} \right)^{-1}} \right]^{-1}$$

where  $\gamma = (1 - \ln(2))/\pi^2$ ,  $t = |\nabla n(\vec{r})|/2k_{\text{T-F}}n(\vec{r})$  is an additional dimensionless density gradient,  $\beta = 0.066725$ , and  $a_0 = \frac{\hbar}{me^2}$ .

The two most frequently utilised approximations for approximating the exchange-correlation energies within the DFT are GGA and LDA. Various additional functionals also exist, which extend beyond GGA and LDA. A robust theory demonstrating these validity does not generally exist. The determination is based on tests conducted on the functional for a range of different materials across a broad scope of systems, the results of which are compared with experimental data proven to have good reliability.

## 2.8 SIESTA

For the purpose of this thesis, all DFT calculations were performed using the SIESTA (Spanish Initiative for Electronic Simulations) package. It is used for obtaining the relaxed geometry of the given structures as well as to perform calculations to explore their electronic characteristics. SIESTA is a self-consistent density functional theory code that enables efficient calculations to be performed using norm-conserving pseudopotentials and linear combination of atomic orbital (LCAO) basis sets [33]. Additional theoretical information regarding the SIESTA code and what it enables can be found in [34, 35]. DFT simulations can be performed in two distinct modes, namely a standard self-consistent field diagonalisation technique used for solving the Kohn-Sham equations and a second technique in which a modified energy functional is directly

minimised [36]. The following sections will present a description of specific components of SIESTA as well the process by which they are implemented in the code.

## **2.9 The Pseudo-Potential Approximation**

This section briefly introduces the notion of pseudo-potentials. A given system's physical characteristics are dependent on a highly effective description of the valence electron distribution. Any electron within an atom is defined as being either core or valence. Nevertheless, for a given system that comprises a significant number of atoms that contain complex potentials, any investigation of its electronic properties will be lengthy and will require a large computer memory. The introduction of an approximation defined as a pseudo-potential or effective potential allows the number of electrons included within the simulation to be reduced. This is aimed at replacing the complex effects of the motion of the non-valence electrons (core electrons) of an atom and nucleus via a pseudo-potential. It follows from the assumption that the core electrons play no role in chemical bonding, are spatially localised around the nucleus, and have wavefunctions which only weakly overlap with those of core electrons from adjacent atoms. Due to the fact that overlap only occurs between valence electron states in the majority of systems, they are the only electrons to play a role in the formation of molecular orbitals. Hence, it can logically be assumed that it is possible to remove the core electrons and substitute them with a pseudo-potential. This enables the coulombic potential term for the core electrons within the Schrödinger equation to be replaced by a modified effective potential term. The pseudo-potential approximation was firstly proposed by Fermi in 1934 and Hellmann in 1935 [35-38].

## 2.10 Bibliography

1. Tung, K. K., & Tung, K. K. (2007). *Topics in mathematical modeling* (pp. 126-157). Princeton, NJ: Princeton University Press.
2. Argaman, N., & Makov, G. (2000). Density functional theory: An introduction. *American Journal of Physics*, 68(1), 69-79.
2. Dronskowski, R. (2005). *Computational chemistry of solid state materials* (Vol. 300). Weinheim, Germany: Wiley-VCH.
3. Eschrig, H. (2003). *The fundamentals of density functional theory* (Vol. 2). Leipzig: Edition am Gutenbergplatz.
4. Kohn, W., Becke, A. D., & Parr, R. G. (1996). Density functional theory of electronic structure. *The Journal of Physical Chemistry*, 100(31), 12974-12980.
5. Martin, R. M. (2020). *Electronic structure: basic theory and practical methods*. Cambridge university press.
6. Parr, R. G., & Weitao, Y. (1994). *Density-Functional Theory of Atoms and Molecules*. Oxford University Press.
7. Kumar, A. (2012). A Brief Introduction to Thomas-Fermi Model in Partial Differential Equations.
8. Lieb, E. H. (1982). Erratum: Thomas-Fermi and related theories of atoms and molecules. *Reviews of Modern Physics*, 54(1), 311.
9. Dreizler, R. M. (1995). Density Functional Theory Vol. 337 of NATO ASI Series B, edited by EKH Gross and RM Dreizler.

10. Hohenberg, P., & Kohn, W. (1964). Inhomogeneous electron gas. *Physical review*, *136*(3B), B864.
11. Kohn, W., & Sham, L. J. (1965). Self-consistent equations including exchange and correlation effects. *Physical review*, *140*(4A), A1133.
12. Koch, W., Holthausen, M. C., & Kaupp, M. (2001). BUCHER-A Chemist's Guide to Density Functional Theory. *Angewandte Chemie-German Edition*, *113*(5), 989-989.
13. Geerlings, P., De Proft, F., & Langenaeker, W. (2003). Conceptual density functional theory. *Chemical reviews*, *103*(5), 1793-1874.
14. Eschrig, H., Koepernik, K., & Chaplygin, I. (2003). Density functional application to strongly correlated electron systems. *Journal of Solid State Chemistry*, *176*(2), 482-495.
15. Ziesche, P., & Tasnádi, F. (2004). Methods for electronic-structure calculations: Overview from a reduced-density-matrix point of view. *International journal of quantum chemistry*, *100*(4), 495-508.
16. Thomas, L. H. (1927, January). The calculation of atomic fields. In *Mathematical proceedings of the Cambridge philosophical society* (Vol. 23, No. 5, pp. 542-548). Cambridge University Press.
17. Burke, K. (2007). friends, The ABC of DFT. *Department of Chemistry, University of California, Irvine, CA, 92697*, 117.

18. Walker, B. G., Molteni, C., & Marzari, N. (2004). Ab initio molecular dynamics of metal surfaces. *Journal of Physics: Condensed Matter*, *16*(26), S2575.
19. Kohn, W. (1999). Nobel Lecture: Electronic structure of matter—wave functions and density functionals. *Reviews of Modern Physics*, *71*(5), 1253.
20. Levy, M. (1982). Electron densities in search of Hamiltonians. *Physical Review A*, *26*(3), 1200.
21. Lima, N. A., Oliveira, L. N., & Capelle, K. (2002). Density-functional study of the Mott gap in the Hubbard model. *EPL (Europhysics Letters)*, *60*(4), 601.
22. March, N. H. (1975). Self-consistent fields in atoms: Hartree and Thomas-Fermi atoms.
23. Ceperley, D. M., & Alder, B. J. (1980). Ground state of the electron gas by a stochastic method. *Physical review letters*, *45*(7), 566.
24. Perdew, J. P., & Zunger, A. (1981). Self-interaction correction to density-functional approximations for many-electron systems. *Physical Review B*, *23*(10), 5048.
25. Naghavi, S. S. (2010). *Theoretical study of correlated systems using hybrid functionals* (Doctoral dissertation, Ph. D. Thesis, Johannes Gutenberg-Universität, Mainz).
26. Hedin, L., & Lundqvist, S. (1970). Effects of electron-electron and electron-phonon interactions on the one-electron states of solids. In *Solid state physics* (Vol. 23, pp. 1-181). Academic Press.

27. Vosko, S. H., Wilk, L., & Nusair, M. (1980). Accurate spin-dependent electron liquid correlation energies for local spin density calculations: a critical analysis. *Canadian Journal of physics*, 58(8), 1200-1211.
28. Perdew, J. P., Burke, K., & Ernzerhof, M. (1996). Generalized gradient approximation made simple. *Physical review letters*, 77(18), 3865.
29. Becke, A. D. (1988). Density-functional exchange-energy approximation with correct asymptotic behavior. *Physical review A*, 38(6), 3098.
30. Hammer, B. H. L. B., Hansen, L. B., & Nørskov, J. K. (1999). Improved adsorption energetics within density-functional theory using revised Perdew-Burke-Ernzerhof functionals. *Physical review B*, 59(11), 7413.
31. Perdew, J. P., & Wang, Y. (1992). Accurate and simple analytic representation of the electron-gas correlation energy. *Physical review B*, 45(23), 13244.
32. Soler, J. M., Artacho, E., Gale, J. D., García, A., Junquera, J., Ordejón, P., & Sánchez-Portal, D. (2002). The SIESTA method for ab initio order-N materials simulation. *Journal of Physics: Condensed Matter*, 14(11), 2745.
33. Sánchez-Portal, D., Ordejón, P., Artacho, E., & Soler, J. M. (1997). Density-functional method for very large systems with LCAO basis sets. *International journal of quantum chemistry*, 65(5), 453-461.
34. Artacho, E., Cella, J. M., Gale, J. D., Martin, R. M., & Soler, J. M. (2011). SIESTA 3.1. *Fundacion General Universidad Autonoma de Madrid, Madrid*.

35. Ordejón, P., Drabold, D. A., Grumbach, M. P., & Martin, R. M. (1993). Unconstrained minimization approach for electronic computations that scales linearly with system size. *Physical Review B*, 48(19), 14646.
36. Kleinman, L., & Bylander, D. M. (1982). Efficacious form for model pseudopotentials. *Physical Review Letters*, 48(20), 1425.
37. Hamann, D. R., Schlüter, M., & Chiang, C. (1979). Norm-conserving pseudopotentials. *Physical Review Letters*, 43(20), 1494.
38. Troullier, N., & Martins, J. L. (1991). Efficient pseudopotentials for plane-wave calculations. *Physical review B*, 43(3), 1993.
39. Troullier, N., & Martins, J. (1990). A straightforward method for generating soft transferable pseudopotentials. *Solid State Communications*, 74(7), 613-616.
40. Boys, S. F., & Bernardi, F. J. M. P. (1970). The calculation of small molecular interactions by the differences of separate total energies. Some procedures with reduced errors. *Molecular Physics*, 19(4), 553-566.
41. Haynes, P. D., Skylaris, C. K., Mostofi, A. A., & Payne, M. C. (2006). Elimination of basis set superposition error in linear-scaling density-functional calculations with local orbitals optimised in situ. *Chemical physics letters*, 422(4-6), 345-349.
42. Mierzwicki, K., & Latajka, Z. (2003). Basis set superposition error in N-body clusters. *Chemical physics letters*, 380(5-6), 654-664.

43. Senent, M. L., & Wilson, S. (2001). Intramolecular basis set superposition errors. *International journal of quantum chemistry*, 82(6), 282-292.
44. Daza, M. C., Dobado, J. A., Molina, J. M., Salvador, P., Duran, M., & Villaveces, J. L. (1999). Basis set superposition error-counterpoise corrected potential energy surfaces. Application to hydrogen peroxide... X (X= F<sup>-</sup>, Cl<sup>-</sup>, Br<sup>-</sup>, Li<sup>+</sup>, Na<sup>+</sup>) complexes. *The Journal of chemical physics*, 110(24), 11806-11813.
45. Boese, A. D., Jansen, G., Torheyden, M., Höfener, S., & Klopper, W. (2010). Effects of counterpoise correction and basis set extrapolation on the MP2 geometries of hydrogen bonded dimers of ammonia, water, and hydrogen fluoride. *Physical Chemistry Chemical Physics: PCCP*, 13(3), 1230-1238.
46. Feynman, R. P. (1939). Forces in molecules. *Physical review*, 56(4), 340.
47. Cresson, J. (2003). Scale calculus and the Schrödinger equation. *Journal Of Mathematical Physics*, 44(11), 4907-4938. doi: 10.1063/1.1618923

## Chapter 3

### 3. Quantum Transport and Green's Functions Method

Chapter 2 described density functional theory, which can be used to calculate the electronic structure of an isolated molecule. The next step is to connect this isolated molecule to semi-infinite leads and compute the probability of transmission through the system. This is achieved by using the Green's function scattering formalism, which I describe in this chapter and is which used in the rest of this thesis. This method is based on scattering theory along with Green's function methods to describe the electric and thermoelectric properties of nanosized systems sandwiched between a number of macroscopic sized metal electrodes.

#### 3.1 Introduction

This chapter will begin by briefly summarising the Landauer formula. Subsequently, I will explain the most basic formula of a retarded Green's function for a tight binding chain in one dimension. After this, I will show how the periodicity of this lattice can be broken at an individual site and demonstrate that the Green's function has a direct relationship with the transmission coefficient  $T(E)$ , throughout the scattering region. The techniques demonstrated on these basic systems will subsequently be employed for deriving the transmission coefficient of mesoscopic conductors of arbitrarily complicated geometry. The approach described in this chapter is based on the assumption that the charge carriers have minimal interaction, inelastic processes are not present and the temperature is zero.

The objective of molecular electronics is to understand the electrical characteristics of molecular junctions, where a molecule (or structure that is adequately small) binds to bulk electrodes to enable ballistic transport to occur via its energy levels. In comparison to the strengths of the bonds between electrodes or molecules, the strength of the coupling between leads and molecules is generally low, which induces a process of scattering from the electrode to the molecule and vice versa. As the system is not periodic, the band structure (as calculated for instance by DFT) no longer describes the electronic properties effectively. Consequently, to increase understanding of the process of scattering in the molecular bridge and the electrode junction, a more general approach is required. This can be accomplished via the Green's function formalism.

### **3.2 Landauer Formula**

The Landauer formula [1, 2] is the conventional method of describing transport phenomena within ballistic mesoscopic systems and can be applied to phase coherent systems in which an individual wave function is sufficient for the electronic flow to be described. It establishes a relation between the mesoscopic sample's conductance and the transmission characteristics of electrons that pass through the sample. In a later section of this chapter, the approach used for calculating the transmission characteristics will be presented.



Figure 3.1: A mesoscopic scatterer linked to contacts with ballistic leads.  $\mu_L$  and  $\mu_R$  represent the chemical potential of the left and right contacts, respectively.

In the case where the scatterer is hit by an incident wave packet from the left, the probability that it will be transmitted to the right is  $T = |\vec{t}|^2 = \vec{t}\vec{t}^*$ , whereas the probability of reflection is  $R = |\vec{r}|^2 = \vec{r}\vec{r}^*$ . As incident electrons have to be either transmitted or reflected, probability conservation suggests  $R + T = 1$ .

Initially, assume we have a mesoscopic scatterer that has connections to a pair of contacts, which act as ideal ballistic leads (Figure 3.1) connected to electron reservoirs, where inelastic relaxation processes can take place. [3]. The chemical potentials of the reservoirs exhibit slight differences ( $\mu_L > \mu_R \Rightarrow \mu_L - \mu_R = \delta E = e\delta V > 0$ ), which will cause the electrons to be driven from the left to the right reservoir. I will first present a discussion of a solution for a single open channel (i.e., in which only a single electron is permitted to move in a specific direction).

In order for the current in this type of system to be calculated, we begin with an analysis of the incident electric current ( $\delta I^{in}$ ) produced by the chemical potential difference:

$$\delta I^{in} = ev_g \frac{\partial n}{\partial E} \delta E = ev_g \frac{\partial n}{\partial E} (\mu_L - \mu_R) \quad (3.1)$$

where  $e$  denotes the electronic charge,  $v_g$  represents the group velocity of wave packets in the lead, and  $\partial n/\partial E$  stands for the density of states (*DOS*) per unit length in the lead in the energy window described by the contacts' chemical potentials:

$$DOS = \frac{\partial n}{\partial E} = 2 \left( \frac{\partial n}{\partial k} \frac{\partial k}{\partial E} \right) \quad (3.2)$$

Spin degeneracy is accounted for by a factor of 2. In one dimension,  $\partial n/\partial k = 1/2\pi$  and  $\partial k/\partial E = 1/\hbar v_g$ . This allows equation (3.1) to be simplified to

$$\delta I^{in} = \frac{2e}{h} (\mu_L - \mu_R) = \frac{2e^2}{h} \delta V \quad (3.3)$$

where  $\delta V$  denotes the voltage related to the chemical potential mismatch. According to equation (3.3), it is evident that if there is no scattering region, a quantum wire with a single open channel has a conductance of  $2e^2/h$ , which equates to around  $77.5 \mu\text{S}$  (thus implying a resistance of  $12.9 \text{ k}\Omega$ ). This quantity is reasonable as it can generally be found on the circuit boards of electrical equipment used in daily life.

If a scattering region is now considered, the current that collects in the right contacts ( $\delta I^{out}$ ) is:

$$\delta I^{out} = \delta I^{in} T = \frac{2e^2}{h} T \delta V \Rightarrow \frac{\delta I^{out}}{\delta V} = \frac{2e^2}{h} T = \mathcal{G} \quad (3.4)$$

This is the renowned Landauer formula, which relates the mesoscopic scatterer's conductance ( $\mathcal{G}$ ) with the transmission probability ( $T$ ) of the electrons that pass through that scatterer. As it describes the conductance of the linear response regime, it only applies for bias voltages that are small,  $\delta V \approx 0$ . The formulation must be revised for a larger bias, and this is not included in the scope of this work.

Büttiker generalised the Landauer formula for cases involving multiple open channels [2]. In such cases, the sum of all the transmission amplitudes replaces the transmission coefficients, which describes electrons that enter via the left contact and then reach the right contact. Hence, equation (3.3) (the Landauer formula) for the open channels is transformed into:

$$\frac{\delta I^{out}}{\delta V} = \mathcal{G} = \frac{2e^2}{h} \sum_{ij} |\vec{t}_{ij}|^2 = \frac{2e^2}{h} \text{Trace} (\vec{t}\vec{t}^\dagger) \quad (3.5)$$

where  $\vec{t}_{ij}$  denotes the transmission amplitude that describes scattering from the left lead's  $j^{th}$  channel to the right lead's  $i^{th}$  channel. After the transmission amplitudes have been defined, it is then possible for the reflection amplitudes  $\vec{r}_{ij}$  to be introduced, which describe the processes of scattering from the left lead's  $j^{th}$  channel to the same lead's  $i^{th}$  channel. The combination of reflection and transmission amplitudes enables an object known as the  $S$  matrix to be defined, which establishes a connection between states entering from the left lead to the right lead, and vice versa:

$$S = \begin{pmatrix} \vec{r} & \vec{t} \\ \vec{t} & \vec{r} \end{pmatrix} \quad (3.6)$$

Here,  $\vec{r}$  and  $\vec{t}$  describe electrons entering from the left, whereas those entering from the right are described by  $\vec{r}$  and  $\vec{t}$ . As suggested by equation (3.5),  $\vec{r}$ ,  $\vec{t}$ ,  $\vec{r}$  and  $\vec{t}$  are matrices when multiple channels are considered and may have increased complexity (such as when a magnetic field is present). It is demanded by charge conservation that the  $S$  matrix must be unitary:  $SS^\dagger = I$ , where  $I$  is the identity matrix. The  $S$  matrix is a critical component of scattering theory. It is not only beneficial for describing transport within the linear response regime, but is also applies to other problems such as adiabatic pumping [4].

### 3.3 Thermoelectric coefficients

The discovery of the Seebeck, Peltier and Thompson effects at the beginning of the 19<sup>th</sup> century established the connections between heat, current, temperature and voltage. The production of electrical current as a result of temperature difference is described by the Seebeck effect, while the cooling or heating of a conductor that carries current are described by the Thompson and Peltier effects. [5]. It is possible to consider a more general system in which the temperature difference is  $\Delta\mathcal{T}$  and there is a potential drop  $\Delta V$  throughout the system, which causes the flow of both heat currents and charge.

To determine expressions for the thermoelectric coefficients of a device with two terminals, the generalised Landauer-Büttiker formulae will be demonstrated for both the heat ( $Q$ ) and charge ( $I$ ) and currents within the linear basis and temperature regime.

The system is comprised of a scattering region that has connections to two leads, which are themselves connected to a pair of electron reservoirs. The definitions of these

reservoirs are based on the chemical potential  $\mu_L$  and  $\mu_R$ , temperature  $\mathcal{T}_L$  and  $\mathcal{T}_R$ , as well as the Fermi distribution function [5]:

$$f_i(E) = \left(1 + e^{\frac{E-\mu_i}{k_B \mathcal{T}_i}}\right)^{-1} \quad (3.7)$$

Based on the assumption that the connection between the reservoirs and leads is established in such a manner that scattering does not occur at their interface, it can be stated that the cause of all the scattering effects is the central scattering region. It is possible to write the right moving charge current of an individual  $k$ -state emerging from the left reservoir on the basis of the number of electrons per unit length  $n$ , Fermi distribution  $f_L$ , group velocity  $v_g$  as well as the scattering region's transmission coefficient  $T(E)$ . (Here, the probability of transmission is represented by  $T(E)$  and the temperature is denoted by  $\mathcal{T}$ ).

$$I_k^+ = nev_g(E(k)) T(E(k)) f_L(E(k)) \quad (3.8)$$

Hence, it is possible to find the overall charge current from the right moving states by summing across all positive  $k$  states and then transforming this into the integral form,

where  $n = 1/L$  for the electron density and  $v_g = \frac{1}{\hbar} \frac{\partial E(k)}{\partial k}$ .

$$I_k^+ = \sum_k e \frac{1}{L} \frac{1}{\hbar} \frac{\partial E(k)}{\partial k} T(E(k)) f_L(E(k)) = \int_{-\infty}^{+\infty} \frac{2e}{\hbar} T(E) f_L(E) dE \quad (3.9)$$

In a similar way, for the left moving states, we obtain:

$$I_k^- = \int_{-\infty}^{+\infty} \frac{2e}{h} T(E) f_R(E) dE \quad (3.10)$$

Hence, one can write the overall right moving current as:

$$I = I^+ - I^- = \frac{2e}{h} \int_{-\infty}^{+\infty} T(E) (f_L(E) - f_R(E)) dE \quad (3.11)$$

Equation (3.11) represents the Landauer-Büttiker formula.

An analogous derivation can be performed for the heat current (alternatively, energy current) of the identical system by beginning with the relation  $Q = Env_g$  instead of  $I = nev_g$ . The outcome is comparable to the previous result, but includes two additional energy terms:

$$Q = Q^+ - Q^- = \frac{2}{h} \int_{-\infty}^{+\infty} T(E) ((E - \mu_L)f_L(E) - (E - \mu_R)f_R(E)) dE$$

where

$$f_L(E) = \left[ 1 + e^{\frac{E - \mu - \frac{\Delta\mu}{2}}{k_B(\mathcal{T} + \frac{\Delta\mathcal{T}}{2})}} \right]^{-1}, \quad f_R(E) = \left[ 1 + e^{\frac{E - \mu + \frac{\Delta\mu}{2}}{k_B(\mathcal{T} - \frac{\Delta\mathcal{T}}{2})}} \right]^{-1}$$

and

$$\mu_L = \mu + \frac{\Delta\mu}{2}, \quad \mu_R = \mu - \frac{\Delta\mu}{2}$$

In the linear-response regime, the electric current  $I$  and heat current  $\dot{Q}$  passing through a device is related to the voltage difference  $\Delta V$  and temperature difference  $\Delta \mathcal{T}$  by Buttiker, Imry, Landauer, et al. [6-9]. Therefore, both currents are related to the

temperature and potential differences through the thermoelectric coefficients  $G, L, M$ , and  $K$  [10, 11]:

$$\begin{pmatrix} I \\ \dot{Q} \end{pmatrix} = \begin{pmatrix} G & L \\ M & K \end{pmatrix} \begin{pmatrix} \Delta V \\ \Delta \mathcal{T} \end{pmatrix} \quad (3.12)$$

The thermoelectric coefficients  $L$  and  $M$ , in the absence of a magnetic field, are related by the Onsager relation:

$$M = -L\mathcal{T} \quad (3.13)$$

where  $\mathcal{T}$  is temperature. By rearranging these equations, the current relations can be expressed in terms of the measurable thermoelectric coefficients, electrical resistance  $R = 1/G$ , thermopower  $S = -\Delta V/\Delta \mathcal{T}$ , Peltier coefficient  $\Pi$ , and the thermal constant  $k$ :

$$\begin{pmatrix} \Delta V \\ \dot{Q} \end{pmatrix} = \begin{pmatrix} \frac{1}{G} & -\frac{L}{G} \\ M & K - \frac{LM}{G} \end{pmatrix} \begin{pmatrix} 1 \\ \Delta \mathcal{T} \end{pmatrix} = \begin{pmatrix} R & S \\ \Pi & -K \end{pmatrix} \begin{pmatrix} 1 \\ \Delta \mathcal{T} \end{pmatrix} \quad (3.14)$$

The thermopower  $S$  is defined as the potential drop due to a temperature difference in the absence of an electrical current:

$$S = -\left(\frac{\Delta V}{\Delta \mathcal{T}}\right)_{I=0} = \frac{L}{G} \quad (3.15)$$

The Peltier coefficient  $\Pi$  is defined as the heat transferred purely due to the charge current in the absence of a temperature difference:

$$\Pi = \left(\frac{\dot{Q}}{I}\right)_{\Delta \mathcal{T}=0} = \frac{M}{G} = -S\mathcal{T} \quad (3.16)$$

Finally the thermal conductance  $k$  is defined as the heat current due to the temperature drop in the absence of an electric current:

$$k = -\left(\frac{\dot{Q}}{\Delta\mathcal{T}}\right)_{I=0} = -\left(1 + \frac{S^2 G\mathcal{T}}{k}\right) \quad (3.17)$$

Therefore, the evaluation of  $S$  or  $\Pi$  gives an idea of how well the device will act as a heat driven current generator or a current driven cooling device.

An additional quantity, the thermoelectric figure of merit,  $Z\mathcal{T}$  [12, 13] can also be defined in terms of these measurable thermoelectric coefficients:

$$Z\mathcal{T} = \frac{S^2 G\mathcal{T}}{k} \quad (3.18)$$

From classical electronics,  $Z\mathcal{T}$  is derived by finding the maximum induced temperature difference produced by an applied electrical current in the presence of Joule heating. Let's consider a current carrying conductor placed between two heat baths with temperatures  $\mathcal{T}_L$  and  $\mathcal{T}_R$ , and electrical potentials  $V_L$  and  $V_R$  respectively. The thermoelectric figure of merit can be defined by finding the maximum induced temperature difference of the conductor due to an electrical current. Defining  $\dot{Q}$  as the gain in heat from bath  $L$  to  $R$ , then from equation (3.14) we have

$$\dot{Q} = \Pi I - k\Delta\mathcal{T} \quad (3.19)$$

This heat transfer will cause the left bath to cool and the right bath to heat, with a result that  $\Delta\mathcal{T}$  increases. The amount of Joule heating can be expressed as  $\dot{Q}_J = RI^2$ , which is proportional to the electrical resistance and the square of the current. This Joule heating will also affect the temperature difference induced by the heat transfer, and therefore in the steady state case:

$$\Pi I - k\Delta\mathcal{T} = \frac{R I^2}{2} \quad (3.20)$$

where,  $R/2$  is the sum of two parallel resistances (internal and external resistance). After rearranging this, the temperature difference is

$$\Delta\mathcal{T} = \frac{1}{k} \left( \Pi I - \frac{R I^2}{2} \right) \quad (3.21)$$

This expression shows how the temperature difference depends on the current. To find the maximum temperature difference, the derivative of equation. (3.21) with respect to the electric current is taken:

$$\frac{\partial \Delta\mathcal{T}}{\partial I} = \frac{\Pi - IR}{k} = 0 \quad (3.22)$$

Finally, by writing back  $I = \Pi / R$  and substituting equation (3.16) into equation (3.22), for the maximum of the temperature different we obtain:

$$(\Delta\mathcal{T})_{max} = \frac{\Pi^2}{2kR} = \frac{S^2\mathcal{T}^2G}{2k} \quad (3.23)$$

$$\frac{(\Delta\mathcal{T})_{max}}{\mathcal{T}} = \frac{S^2\mathcal{T}^2G\mathcal{T}}{2k} = \frac{1}{2}Z \quad (3.24)$$

yielding a dimensionless number that can be used to characterize the 'efficiency' of a molecular device.

### 3.4 Scattering in One Dimension

Prior to explaining the generalised methodology, it is beneficial to examine how the scattering matrix for a basic one-dimensional structure can be calculated. This will enable the methodology to be clearly described. As Green's functions will be employed as part of the derivation, the Green's function form for a basic one-dimensional discretised lattice will firstly be discussed (Section 3.4.1) followed by the calculation of the scattering matrix of a one-dimensional scatterer (Section 3.4.2).

#### 3.4.1 Perfect One-Dimensional Lattice

The following section will include a discussion on the Green's function form of a basic infinite one-dimensional chain that has on-site energies ( $\epsilon_0$ ) as well as hopping parameters ( $-\gamma$ ), as illustrated in Figure 3.2.

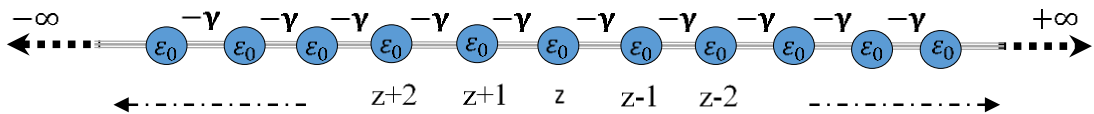


Figure 3.2: Tight-binding approximation of a one-dimensional periodic lattice with on-site energies  $\epsilon_0$  and couplings  $-\gamma$ .

The Hamiltonian for this system, in matrix form, has the on-site energies ( $\epsilon_0$ ) along the diagonal, as well as the hopping components ( $-\gamma$ ) along the first off-diagonal:

$$H = \begin{pmatrix} \cdot & \cdot & 0 & 0 & 0 & 0 & 0 & 0 \\ \cdot & \cdot & \cdot & 0 & 0 & 0 & 0 & 0 \\ 0 & \cdot & \varepsilon_o & -\gamma & 0 & 0 & 0 & 0 \\ 0 & 0 & -\gamma^* & \varepsilon_o & -\gamma & 0 & 0 & 0 \\ 0 & 0 & 0 & -\gamma^* & \varepsilon_o & -\gamma & 0 & 0 \\ 0 & 0 & 0 & 0 & -\gamma^* & \varepsilon_o & \cdot & 0 \\ 0 & 0 & 0 & 0 & 0 & 0 & \cdot & \cdot \\ 0 & 0 & 0 & 0 & 0 & 0 & 0 & \cdot \end{pmatrix} \quad (3.25)$$

In the tight-binding approximation and substituting equation (3.25) as well as the wave function into the Schrödinger equation  $(E - H)\Psi_{(z)} = 0$ , we obtain:

$$\begin{pmatrix} \cdot & \cdot \\ \cdot & \cdot \\ \cdot & -\gamma^* (E - \varepsilon_o) & -\gamma & 0 & 0 & 0 & \cdot & \cdot \\ \cdot & 0 & -\gamma^* (E - \varepsilon_o) & -\gamma & 0 & 0 & \cdot & \cdot \\ \cdot & 0 & 0 & -\gamma^* (E - \varepsilon_o) & -\gamma & 0 & \cdot & \cdot \\ \cdot & 0 & 0 & 0 & -\gamma^* (E - \varepsilon_o) & -\gamma & \cdot & \cdot \\ \cdot & \cdot \\ \cdot & \cdot \end{pmatrix} \begin{pmatrix} \cdot \\ \cdot \\ \Psi_{(z-1)} \\ \Psi_{(z)} \\ \Psi_{(z+1)} \\ \Psi_{(z+2)} \\ \cdot \\ \cdot \end{pmatrix} = \begin{pmatrix} \cdot \\ \cdot \\ 0 \\ 0 \\ 0 \\ 0 \\ \cdot \\ \cdot \end{pmatrix} \quad (3.26)$$

The Schrödinger equation can now be written out for row  $z$  of the Hamiltonian as

$$-\gamma^* \Psi_{(z-1)} + (E - \varepsilon_o) \Psi_{(z)} - \gamma \Psi_{(z+1)} = 0 \quad (3.27)$$

Therefore, in order for any function  $\Psi_{(z)}$  to be a wave function, it is only necessary for it to satisfy the Schrödinger equation (equation (3.27)). In the context of this perfect lattice, the wave function is in the form of a propagating Bloch state (equation (3.28)), which is normalised by its group velocity ( $v_g$ ) so it carries unit current flux. After substituting this into equation (3.27) (assuming  $\gamma = \gamma^*$ , in other words, if  $\gamma$  is real), it produces the famous one-dimensional dispersion relation (equation (3.29)):

$$\Psi_{(z)} = \frac{1}{\sqrt{v_g}} e^{ikz} \quad (3.28)$$

$$E = \varepsilon_o - 2\gamma \cos k \quad (3.29)$$

where the quantum number ( $k$ ) generally defined as the wavenumber is introduced. The retarded Green's function  $\mathcal{G}(z, z')$  has a close association with the wave function and actually represents a solution for an equation that has a strong similarity to that of the Schrödinger equation:

$$\left. \begin{aligned} (E - H) \mathcal{G}(z, z') &= \delta_{(z, z')} \Rightarrow \\ -\gamma^* \mathcal{G}(z - 1, z') + (E - \varepsilon_0) \mathcal{G}(z, z') - \gamma \mathcal{G}(z + 1, z') &= \delta_{(z, z')} \end{aligned} \right\} \quad (3.30)$$

where

$$\begin{aligned} \delta_{(z, z')} &= 1, & \text{if } z &= z' \\ \delta_{(z, z')} &= 0, & \text{if } z &\neq z' \end{aligned}$$

In physical terms, the retarded Green's function,  $\mathcal{G}(z, z')$  describes a system's response at a specific point  $z$  caused by an excitation at a point  $z'$ . It is intuitively expected that this excitation generates a pair of waves, which travel outwards from the excitation point, which have amplitudes of  $\mathcal{B}$  and  $\mathcal{D}$ , as illustrated in Figure 3.4.

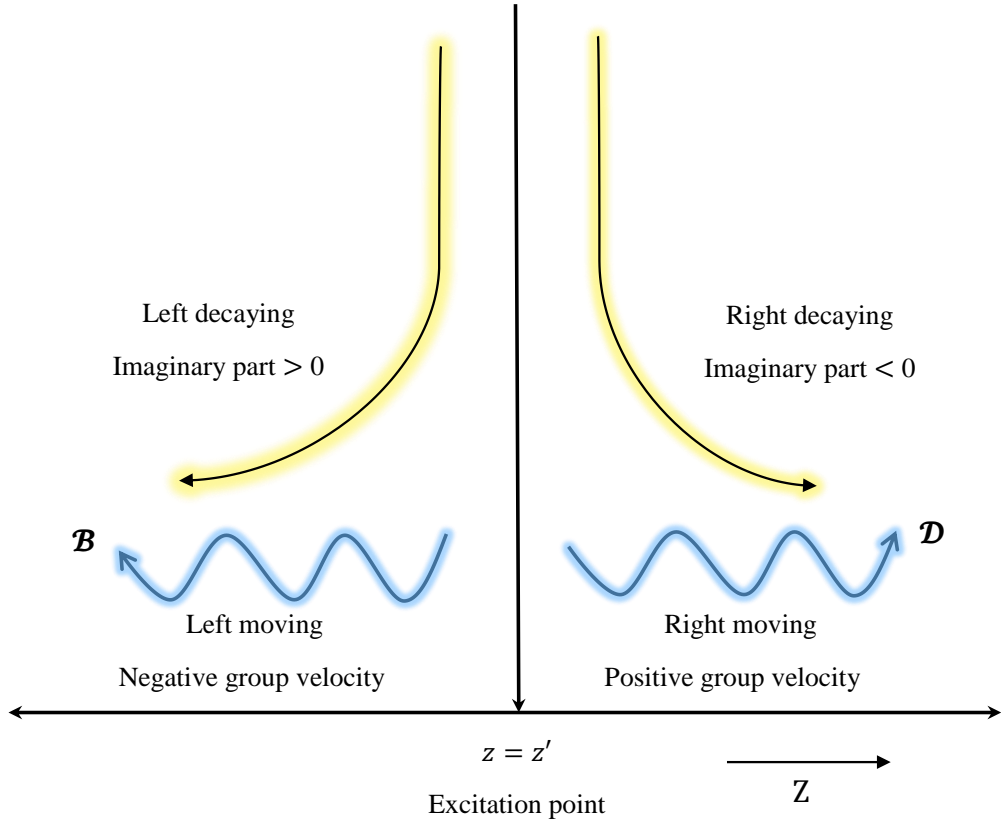


Figure 3.3: A schematic illustration the retarded Green's function structure for an infinite one-dimensional lattice.

As a result of an excitation at  $z = z'$ , waves are propagated left and right (blue modes are open channels), which have amplitudes of  $\mathcal{B}$  and  $\mathcal{D}$ , respectively, whereas the decaying modes are represented by the red colour.

Mathematically, these waves are

$$g(z, z') = \begin{cases} \mathcal{D} e^{ikz}, & z > z' \\ \mathcal{B} e^{-ikz}, & z < z' \end{cases} \quad (3.31)$$

Equation (3.30) is satisfied at each point by this solution, apart from  $z = z'$ . For this to be resolved, it is necessary for the Green's function to be continuous (equation (3.32)), so the two are equated at  $z = z'$ :

$$[\mathcal{G}(z, z')]_{Left} = [\mathcal{G}(z, z')]_{Right} \quad (3.32)$$

$$\mathcal{B}e^{-ikz'} = \mathcal{D}e^{ikz'} \quad (3.33)$$

$$\mathcal{B} = \mathcal{D}e^{2ikz'} \quad (3.34)$$

Substitution of equation (3.34) into the Green's functions (equation (3.31)) generates:

$$\mathcal{G}(z, z') = \begin{cases} \mathcal{D} e^{ikz} & , \quad z \geq z' \\ \mathcal{D}e^{2ikz'} e^{-ikz} = \mathcal{D}e^{ikz'} e^{ik(z'-z)}, & z \leq z' \end{cases} \quad (3.35)$$

When equation (3.35) is rewritten, a beneficial symmetry is revealed:

$$\mathcal{G}(z, z') = \begin{cases} \mathcal{D}e^{ikz'} e^{ik(z-z')}, & z \geq z' \\ \mathcal{D}e^{ikz'} e^{ik(z'-z)}, & z \leq z' \end{cases}$$

After noting that the complex exponent's power is consistently positive it is possible to write the last equation as:

$$\mathcal{G}(z, z') = \mathcal{D}e^{ikz'} e^{ik|z'-z|}, \quad \forall z \quad (3.36)$$

From equation (3.30) for  $z = z'$ , one obtains

$$\mathcal{D}e^{ikz'} = \frac{1}{i\hbar v_g}$$

where  $v_g$  is the group velocity, given by

$$v_g = \frac{1}{\hbar} \frac{\partial E(k)}{\partial k} = \frac{2\gamma \sin k}{\hbar}$$

It is interesting to compare this result with the Green's function in the continuum case,

where  $H$  can be written as  $-\frac{\hbar^2}{2m} \nabla^2$ , or  $-\frac{\hbar v_g}{2k} \nabla^2$  (where  $v_g = \frac{\hbar k}{m}$  denotes the group velocity), and the Green's function (equation (3.36)) can be substituted in, thus giving

$$\left( E + \frac{\hbar v_g}{2k} \frac{\partial^2}{\partial z^2} \right) (\mathcal{D}e^{ikz'} e^{ik|z'-z|}) = \delta_{(z, z')} \quad (3.37)$$

If this function is integrated over a minimal distance, focused on  $z'$ , that has width  $2\omega^+$ , it is found that:

$$\int_{z'-\omega^+}^{z'+\omega^+} \left( E + \frac{\hbar v_g}{2k} \frac{\partial^2}{\partial z^2} \right) (\mathcal{D} e^{ikz'} e^{ik|z'-z|}) dz = 1 \quad (3.38)$$

$$\mathcal{D} e^{ikz'} \left( \overbrace{E \int_{z'-\omega^+}^{z'+\omega^+} e^{ik|z'-z|} dz}^{=Zero} + \int_{z'-\omega^+}^{z'+\omega^+} \frac{\hbar v_g}{2k} \frac{\partial^2}{\partial z^2} e^{ik|z'-z|} dz \right) = 1 \quad (3.39)$$

$$\mathcal{D} e^{ikz'} \left( \frac{\hbar v_g}{2k} \frac{\partial}{\partial z} e^{ik|z'-z|} \right)_{z'-\omega^+}^{z'+\omega^+} = \mathcal{D} e^{ikz'} \left( \frac{\hbar v_g}{2k} i k e^{ik|z'-z|} \right)_{z'-\omega^+}^{z'+\omega^+} = 1 \quad (3.40)$$

$$\mathcal{D} e^{ikz'} \frac{\hbar v_g}{2k} 2ik = 1 \Rightarrow \mathcal{D} e^{ikz'} = \frac{1}{i\hbar v_g} \quad (3.41)$$

Therefore, it is possible to write the retarded Green's function as:

$$\mathcal{G}^R(z, z') = \frac{1}{i\hbar v_g} e^{ik|z-z'|} \quad (3.42)$$

where the group velocity is determined by differentiating the dispersion relation and is written as:

$$v_g = \frac{\hbar k}{m} \quad (3.43)$$

This shows that the discrete and continuum Green's function have the same form, provided one uses the appropriate group velocities in each case.

The literature provides a more comprehensive derivation [3, 14, 15]. Additionally, it is important to note that a different solution to this problem also exists. The solution

discussed above is the retarded Green's function, denoted  $\mathcal{G}^R(z, z')$ . The advanced (also known as source) Green's function,  $\mathcal{G}^A(z, z')$ , is a solution that has equal validity:

$$\mathcal{G}^A(z, z') = \frac{-1}{i\hbar v_g} e^{-ik|z-z'|} = \frac{i}{\hbar v_g} e^{-ik|z-z'|} \quad (3.44)$$

As opposed to the retarded Green's function that describes waves moving outward from the point of excitation ( $z = z'$ ), the advanced Green's function describes two waves moving in an inward direction, which then disappear at the point of excitation. In the context of the current thesis, the retarded Green's function will be used and for simplicity the superscript  $R$  will be dropped.

Thus,  $\mathcal{G}(z, z') = \mathcal{G}^R(z, z')$ .

Since the likelihood that an electron will propagate between two points on this optimal lattice (i.e. the transmission coefficient) is unity when its energy is between  $(\varepsilon_0 - 2\gamma)$  and  $(\varepsilon_0 + 2\gamma)$ , the system offers minimal benefits in this case. Nevertheless, if a certain flaw is generated in the lattice, it will serve as a scatterer and modifications will be made to the transmission coefficient.

### 3.4.2 One-Dimensional Scattering Solution

The following section will consider two one-dimensional tight-binding semi-infinite leads linked with a coupling element  $(-\alpha)$ . The on-site potentials  $(\varepsilon_0)$  and hopping elements  $(-\gamma)$  of both leads are the same. However, although it appears to be simple, the system is of great interest because it is possible to reduce one-dimensional setups back to this topology. Taking this into account, obtaining analytical solutions for the reflection and transmission coefficients would be highly beneficial.

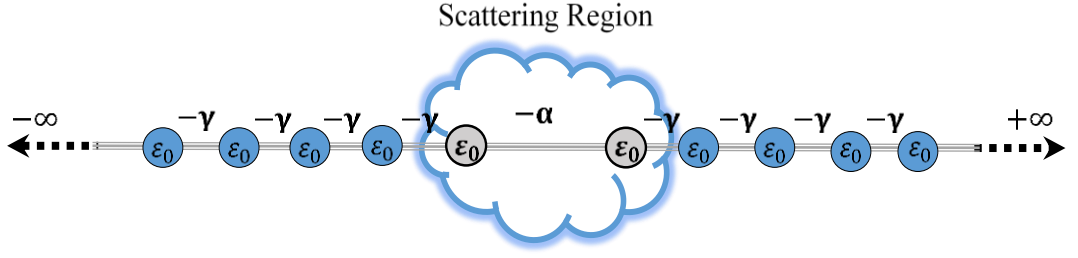


Figure 3.4: Tight-binding model of a one-dimensional scatterer connected to one-dimensional leads.

First we define the Hamiltonian which consists of an infinite matrix,

$$H = \begin{pmatrix} \bullet & \bullet & 0 & 0 & 0 & 0 & 0 & 0 \\ \bullet & \bullet & -\gamma & 0 & 0 & 0 & 0 & 0 \\ 0 & -\gamma^* & \varepsilon_o & -\gamma & 0 & 0 & 0 & 0 \\ 0 & 0 & -\gamma^* & \varepsilon_o & -\alpha & 0 & 0 & 0 \\ 0 & 0 & 0 & -\alpha^* & \varepsilon_o & -\gamma & 0 & 0 \\ 0 & 0 & 0 & 0 & -\gamma^* & \varepsilon_o & -\gamma & 0 \\ 0 & 0 & 0 & 0 & 0 & -\gamma^* & \bullet & \bullet \\ 0 & 0 & 0 & 0 & 0 & 0 & \bullet & \bullet \end{pmatrix} = \begin{pmatrix} H_L & V_c \\ V_c^\dagger & H_R \end{pmatrix} \quad (3.45)$$

where  $H_L$  and  $H_R$  refer to the Hamiltonian's leads, which are the semi-infinite equivalents of the Hamiltonian demonstrated in equation (3.7), while  $V_c$  represents the coupling parameter. For a real  $\gamma$ , the dispersion relation that corresponds to these leads is given by equation (3.29), and the group velocity by equation (3.43):

$$E(k) = \varepsilon_o - 2\gamma \cos k \quad (3.46)$$

and

$$v_g = \frac{1}{\hbar} \frac{\partial E}{\partial k} \quad (3.47)$$

To determine the scattering amplitudes, the system's Green's function should be calculated, which is defined by

$$(E - H)G = I \implies G = (E - H)^{-1} \quad (3.48)$$

If the energy  $E$  equals the Hamiltonian  $H$ , it is singular. For such an issue to be avoided and circumvented, the logical step is to take the limit:

$$G_{\mp} = \lim_{\eta \rightarrow 0} (E - H \mp i\eta)^{-1} \quad (3.49)$$

where  $\eta$  is a small positive number and  $G_-$  ( $G_+$ ) denotes the retarded (advanced) Green's function. For the purpose of the current thesis, only the retarded Green's functions will be used and therefore the negative sign will be selected. Equation (3.42) shows the retarded Green's function for an infinite one-dimensional chain that has identical parameters

$$g_{ml} = \frac{1}{i\hbar v_g} e^{ik|m-l|} \quad (3.50)$$

where  $m$  and  $l$  label the sites of the chain. To determine a semi-infinite lead's Green's function, it is necessary for suitable boundary conditions to be introduced. In this example, it is a semi-infinite lattice, so the chain must end at a specific point ( $i_o$ ), indicating that every point for which  $i \leq i_o$  is missing. This can be accomplished via the introduction of a wave function to the Green's function, which enables this condition to be represented mathematically. In this instance, the wave function is given as:

$$\psi_{ml}^{i_o} = -\frac{e^{ik(2i_o-m-l)}}{i\hbar v_g} \quad (3.51)$$

The Green's function is obtained by summing (3.50) and (3.51) ( $g_{ml} = g_{ml}^{\infty} + \psi_{ml}^{i_o}$ ), which yields the following at the boundary ( $m = l = i_o - 1$ ):

$$\mathcal{G}_{i_o-1, i_o-1} = -\frac{e^{ik}}{\gamma} \quad (3.52)$$

If the example of decoupled leads is considered ( $\alpha = 0$ ), the system's overall Green's function is basically represented by the decoupled Green's function:

$$\mathcal{G} = \begin{pmatrix} -\frac{e^{ik}}{\gamma} & 0 \\ 0 & -\frac{e^{ik}}{\gamma} \end{pmatrix} = \begin{pmatrix} \mathcal{G}_L & 0 \\ 0 & \mathcal{G}_R \end{pmatrix} \quad (3.53)$$

If the interaction is then activated ( $\alpha \neq 0$ ), then in order to obtain the coupled system's Green's function  $G$  to be obtained, Dyson's equation is employed:

$$G = (\mathcal{G}^{-1} - V)^{-1} \quad (3.54)$$

where the operator  $V$  that describes the interaction linking the pair of leads takes the form

$$V = \begin{pmatrix} 0 & V_c \\ V_c^\dagger & 0 \end{pmatrix} = \begin{pmatrix} 0 & \alpha \\ \alpha^* & 0 \end{pmatrix} \quad (3.55)$$

Equation (3.54) shows the solution to Dyson's equation, which is

$$G = \frac{1}{\gamma^2 e^{-2ik} - \alpha^2} \begin{pmatrix} -\gamma e^{-ik} & \alpha \\ \alpha^* & -\gamma e^{-ik} \end{pmatrix} \quad (3.56)$$

All that remains is that the reflection ( $\tilde{r}$ ) and transmission ( $\tilde{t}$ ) amplitudes should be calculated using the Green's function from equation (3.56). This is achieved with the Fisher-Lee relation [3, 16], which establishes a relationship between the scattering problem's scattering amplitudes and the problem's Green's function. In this case, the Fisher-Lee relations determine that:

$$\tilde{r} = G_{1,1} v_g - 1 \quad (3.57)$$

and

$$\vec{t} = G_{1,2} v_g e^{ik} \quad (3.58)$$

The above amplitudes are related to particles moving from the left. If particles entering from the right are considered, then analogous expressions could be derived from the transmission ( $\vec{t}$ ) and reflection ( $\vec{r}$ ) amplitudes.

As we now have the complete scattering matrix, the Landauer formula (equation (3.4)) can be used for the purpose of calculating the zero-bias conductance. It is possible to generalise the process employed for finding this analytical solution for a one-dimensional scatterer's conductance to geometries with increased complexity. Hence, the steps can be briefly summarised as follows:

1. The initial step involves the calculation of the Green's function that describes the leads' surface sites.
2. The overall Green's function when a scatterer is present is determined using the Dyson's equation.
3. The Fisher-Lee relation yields the scattering matrix from the Green's function.
4. Then, the zero-bias conductance can be determined according to the Landauer formula.

In section 3.5, it will be shown that the setup described here, although it appears to be simple, is in fact relatively general, due to the fact that it is possible to reduce all kinds of scattering regions back to the example of a pair of one-dimensional leads by employing a method known as decimation.

### **3.5 Generalisation of the Scattering Formalism**

This section will demonstrate a generalised method that can be used for transport calculations based on the approach proposed by Lambert *et al.*, described in [5,17-18].

This has similarities to the aforementioned approach. The first step is to compute the surface Green's function of crystalline leads, followed by the introduction of the decimation technique for the purpose of reducing the scattering region's dimensionality. The last step is to recover the scattering amplitudes by using a generalisation of the Fisher-Lee relation.

### 3.5.1 Hamiltonian and Green's Function of the Leads

Firstly, it is necessary to provide an accurate definition of a lead. It is generally an object with perfect crystallinity that serves as an optimal wave-guide for the transportation of excitations between reservoirs and the scattering region. This section will review a general semi-infinite crystalline electrode with arbitrary complexity. Due to the crystalline nature of the leads, the Hamiltonian's structure is a generalisation of the one-dimensional electrode represented in equation (3.25).

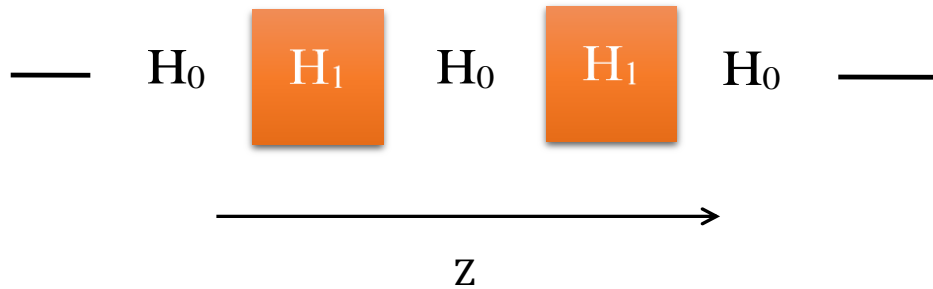


Figure 3.5: Schematic representation of semi-infinite generalised leads. States described by the Hamiltonian  $H_0$  are linked by a generalised hopping matrix  $H_1$ . The direction  $z$  is defined to be parallel to the chain axis. A label  $z$  can be assigned to every slice.

Rather than site energies, a Hamiltonian exists for every repeating layer of the bulk electrode ( $H_0$ ), as well as a coupling matrix that describes the hopping parameters between adjacent layers ( $H_1$ ).

This system has a Hamiltonian as follows:

$$H = \begin{pmatrix} \bullet & \bullet & 0 & 0 & 0 & 0 & 0 & 0 \\ \bullet & \bullet & H_1 & 0 & 0 & 0 & 0 & 0 \\ 0 & H_1^\dagger & H_o & H_1 & 0 & 0 & 0 & 0 \\ 0 & 0 & H_1^\dagger & H_o & H_1 & 0 & 0 & 0 \\ 0 & 0 & 0 & H_1^\dagger & H_o & H_1 & 0 & 0 \\ 0 & 0 & 0 & 0 & H_1^\dagger & H_o & H_1 & 0 \\ 0 & 0 & 0 & 0 & 0 & H_1^\dagger & \bullet & \bullet \\ 0 & 0 & 0 & 0 & 0 & 0 & \bullet & \bullet \end{pmatrix} \quad (3.59)$$

where  $H_o$  and  $H_1$  are generally complex matrices and the only limitation is that the full Hamiltonian ( $H$ ) must be Hermitian. In this section, the initial objective is for the Green's function of this type of lead to be calculated for general  $H_1$  and  $H_o$ . For the Green's function to be calculated, it is necessary for the Hamiltonian's spectrum to be calculated by finding a solution for the lead's Schrödinger equation:

$$H_1^\dagger \Psi_{(z-1)} + H_o \Psi_{(z)} + H_1 \Psi_{(z+1)} = E \Psi_{(z)} \quad (3.60)$$

where  $\Psi_{(z)}$  represents the wave function that describes the layer  $z$ . The assumption is made that the system is infinitely periodic but only in the  $z$  direction; hence, it is possible to represent the on-site wave function  $\Psi_{(z)}$  in Bloch form; this comprises a product of a propagating plane wave as well as a wave function ( $\Phi_{(k)}$ ), which exists perpendicular to the direction of transport ( $z$ ). If the dimensions of the layer Hamiltonian ( $H_o$ ) are  $M \times M$  (i.e., it comprises  $M$  site energies and corresponding hopping elements), then the perpendicular wave function ( $\Phi_{(k)}$ ), will possess  $M$  degrees of freedom and assumes the form of a  $1 \times M$  dimensional vector. Therefore, the wave function  $\Psi_{(z)}$  is

$$\Psi_{(z)} = \sqrt{n_{(k)}} e^{ikz} \Phi_{(k)} \quad (3.61)$$

where  $n_k$  denotes an arbitrary normalisation parameter. If this is substituted into equation (3.60), this yields:

$$(H_o + e^{ik}H_1 + e^{-ik}H_1^\dagger)\Phi_{(k)} = E\Phi_{(k)} \quad (3.62)$$

$$H(k)\Phi_{(k)} = E\Phi_{(k)}$$

$$H(k) = H_o + e^{ik}H_1 + e^{-ik}H_1^\dagger$$

In general, for a band structure of this type of problem to be found, values of  $k$  would be selected and then the eigenvalues would be calculated [ $E = E_l(k)$ ], where  $l = 1, 2, \dots, M$  is the band index. For every  $k$  value, the eigenvalue problem will have  $M$  solutions, and thus,  $M$  energy values. Consequently, if multiple values are selected for  $k$ , the process of constructing a band structure is comparatively straightforward.

The opposite approach is taken for scattering problems; rather than determining the  $E$  values at a specific  $k$ , the values of  $k$  are found at a specific  $E$ . For this to be achieved, a root-finding technique could have been adopted, but this would have necessitated significant computational work as the wave numbers generally have high complexity. Rather, an alternative eigenvalue problem is written down where the energy is the input and the wave numbers are generated after the introduction of the function

$$\theta_{(k)} = e^{-ikz} \Phi_{(k)} \rightarrow \Phi_{(k)} = e^{ikz} \theta_{(k)} \quad (3.63)$$

which is then combined with equation (3.62):

$$\begin{pmatrix} -H_1^{-1}(H_o - E) & -H_1^{-1}H_1^\dagger \\ I & 0 \end{pmatrix} \begin{pmatrix} \Phi_{(k)} \\ \theta_{(k)} \end{pmatrix} = e^{ik} \begin{pmatrix} \Phi_{(k)} \\ \theta_{(k)} \end{pmatrix} \quad (3.64)$$

Given a layer Hamiltonian ( $H_o$ ) that has dimensions of  $M \times M$ , equation (3.64) will produce  $2M$  eigenvalues ( $e^{ik_l}$ ) and eigenvectors ( $\Phi_{(k_l)}$ ) with magnitude  $M$ . These states

can then be sorted into four categories based on whether they are propagating or decaying, in addition to whether they are moving to the left ( $z \rightarrow -\infty$ ) or to the right ( $z \rightarrow \infty$ ). A state is considered to be propagating when it has a real  $k_l$  value. Where the wave number has a positive imaginary part, it is defined as a left decaying state, whereas if the imaginary part is negative, it is defined as a right decaying state. The sorting of propagating states is based on the state's group velocity, which is given by

$$v_g^{k_l} = \frac{1}{\hbar} \frac{\partial E_{k,l}}{\partial k} \quad (3.65)$$

A positive group velocity ( $v_g^{k_l}$ ) indicates that the state is right propagating, and it is left propagating otherwise. This sorting is summarised in Table 3.1.

Table 3.1: Sorting the eigenstates into left and right propagating or decaying states based on the wave number and group velocity.

	Left	Right
Decaying	$Im(k_l) > 0$	$Im(k_l) < 0$
Propagating	$Im(k_l) = 0, v_g^{k_l} < 0$	$Im(k_l) = 0, v_g^{k_l} > 0$

For simplicity, the wave numbers ( $k_l$ ) belonging to the left propagating/decaying set of wave numbers will now be represented by  $\bar{k}_l$ , while the right propagating/decaying wave numbers will still be simply  $k_l$ . Hence,  $\Phi_{(k_l)}$  denotes a wave function related to the "right" state, whereas  $\Phi_{(\bar{k}_l)}$  is linked to the "left" state. It should be noted that if  $H_1$  can be inverted, the number ( $M$ ) of left and right moving states must be exactly the same. It is evident that when  $H_1$  is singular, it is not possible to construct the matrix in equation (3.64) as it is dependent on  $H_1$  being inverted. Nevertheless, any of the various

available techniques can be employed for this problem to be resolved. In the first [18], a decimation approach is employed so that an effective, non-singular  $H_1$  can be created. A different method of solving this problem could involve populating a singular  $H_1$  with small random numbers, which would introduce an explicit numerical error. This is a plausible approach as the size of the numerical error introduced could be as small as the numerical error introduced by decimation. An alternative solution is to rewrite equation (3.64) in such a way that it is not necessary to invert  $H_1$ :

$$\begin{pmatrix} -(H_o - E) & -H_1^\dagger \\ I & 0 \end{pmatrix} \begin{pmatrix} \Phi_{(k)} \\ \theta_{(k)} \end{pmatrix} = e^{ik} \begin{pmatrix} H_1 & 0 \\ 0 & I \end{pmatrix} \begin{pmatrix} \Phi_{(k)} \\ \theta_{(k)} \end{pmatrix} \quad (3.66)$$

However, the process of solving this generalised eigen-problem leads to increased computational expense. All of the abovementioned techniques are relatively effective when attempting to tackle the problem involving a singular  $H_1$  matrix, while the same applies to the condition stipulating that the number ( $M$ ) of left and right moving states must be identical, regardless of whether  $H_1$  is singular or not.

For a given choice of  $k$ , the solutions to the eigen-problem equation (3.62) will generate an orthogonal basis set; nevertheless, whereas for a given  $E$ , an orthogonal set of states is generally not formed by the eigenstates ( $\Phi_{(k_l)}$ ) acquired by solving the eigen-problem (equation (3.64)). This has particular importance due to the fact that the non-orthogonality must be addressed in the construction of the Green's function. Hence, it is essential the duals are introduced to  $\Phi_{(k_l)}$  and  $\Phi_{(\bar{k}_l)}$  in such a manner that they conform to

$$\tilde{\Phi}_{(k_l)}^\dagger \Phi_{(k_j)} = \tilde{\Phi}_{(\bar{k}_l)}^\dagger \Phi_{(\bar{k}_j)} = \delta_{ij} \quad (3.67)$$

The generalised completeness relation this yields is:

$$\sum_{l=1}^M \tilde{\Phi}_{(k_l)}^\dagger \Phi_{(k_l)} = \sum_{l=1}^M \tilde{\Phi}_{(\bar{k}_l)}^\dagger \Phi_{(\bar{k}_l)} = I \quad (3.68)$$

After the entire set of eigenstates at a given energy has been obtained, the Green's function can firstly be calculated for the infinite system and subsequently, if suitable boundary conditions are satisfied, for the semi-infinite leads at their surfaces. Due to the fact that the Schrödinger equation is satisfied by the Green's function when  $z \neq z'$ , the Green's function can be built up from the combination of the eigenstates  $\Phi_{(k_l)}$  and  $\Phi_{(\bar{k}_l)}$ :

$$g(z, z') = \begin{cases} \sum_{l=1}^M \Phi_{(k_l)} e^{ik_l(z-z')} \omega_{k_l}^\dagger, & z \geq z' \\ \sum_{l=1}^M \Phi_{(\bar{k}_l)} e^{i\bar{k}_l(z-z')} \omega_{\bar{k}_l}^\dagger, & z \leq z' \end{cases} \quad (3.69)$$

where the  $M$ -component vectors  $\omega_{k_l}$  and  $\omega_{\bar{k}_l}$  are to be ascertained. It should be noted that the structure of this equation is similar to that of equation (3.31), while the degrees of freedom in the transverse direction are also included within the vectors  $\Phi_{(k)}$  and  $\omega_k$ . The next step focuses on obtaining the  $\omega$  vectors. Similar to Section 3.4.1, it is known that equation (3.69) has to be continuous at  $z = z'$  and must satisfy the Green's function equation (equation (3.30)).

The expression for the first condition is:

$$\sum_{l=1}^M \Phi_{(k_l)} \omega_{k_l}^\dagger = \sum_{l=1}^M \Phi_{(\bar{k}_l)} \omega_{\bar{k}_l}^\dagger \quad (3.70)$$

while the second is:

$$\sum_{l=1}^M \left[ (E - H_o) \Phi_{(k_l)} \omega_{k_l}^\dagger + H_1 e^{ik_l} \omega_{k_l}^\dagger + H_1^\dagger \Phi_{(\bar{k}_l)} e^{-i\bar{k}_l} \omega_{\bar{k}_l}^\dagger \right] = I$$

$$\sum_{l=1}^M \left[ (E - H_o) \Phi_{(k_l)} \omega_{k_l}^\dagger + H_1 \Phi_{(k_l)} e^{ik_l} \omega_{k_l}^\dagger + H_1^\dagger \Phi_{(\bar{k}_l)} e^{-i\bar{k}_l} \omega_{\bar{k}_l}^\dagger + H_1^\dagger e^{-ik_l} \omega_{k_l}^\dagger - H_1^\dagger e^{-i\bar{k}_l} \omega_{\bar{k}_l}^\dagger \right] = I$$

$$\sum_{l=1}^N \left[ H_1^\dagger \Phi_{(\bar{k}_l)} e^{i\bar{k}_l} \omega_{\bar{k}_l}^\dagger - H_1^\dagger \Phi_{(k_l)} e^{-ik_l} \omega_{k_l}^\dagger \right] + \sum_{l=1}^M \left[ (E - H_o) + H_1 e^{ik_l} + H_1^\dagger e^{-ik_l} \right] \Phi_{(k_l)} \omega_{k_l}^\dagger = I$$

Additionally, it is known from the Schrödinger equation (equation (3.62)) that:

$$\sum_{l=1}^M \left[ (E - H_o) + H_1 e^{ik_l} + H_1^\dagger e^{-ik_l} \right] \Phi_{(k_l)} = 0 \quad (3.71)$$

These yield

$$\sum_{l=1}^N H_1^\dagger \left[ \Phi_{(\bar{k}_l)} e^{i\bar{k}_l} \omega_{\bar{k}_l}^\dagger + \Phi_{(k_l)} e^{-ik_l} \omega_{k_l}^\dagger \right] = I \quad (3.72)$$

Next, the dual vectors defined in equation (3.67) are used. The multiplication of equation (3.72) by  $\tilde{\Phi}_{(k_p)}^\dagger$  yields

$$\sum_{l=1}^M \tilde{\Phi}_{(k_p)}^\dagger \Phi_{(\bar{k}_l)} \omega_{\bar{k}_l}^\dagger = \omega_{k_p}^\dagger \quad (3.73)$$

Likewise, multiplication by  $\tilde{\Phi}_{(\bar{k}_p)}^\dagger$  produces

$$\sum_{l=1}^M \tilde{\Phi}_{(\bar{k}_p)}^\dagger \Phi_{(k_l)} \omega_{k_l}^\dagger = \omega_{\bar{k}_p}^\dagger \quad (3.74)$$

Utilising the continuity equation (3.70) along with equations (3.73) and (3.74), the Green's function equation (3.72) becomes

$$\sum_{l=1}^M \sum_{p=1}^M H_1^\dagger \left( \Phi_{(\bar{k}_l)} e^{-i\bar{k}_l} \tilde{\Phi}_{(\bar{k}_l)}^\dagger - \Phi_{(k_l)} e^{-ik_l} \tilde{\Phi}_{(k_l)}^\dagger \right) \Phi_{(\bar{k}_p)} \omega_{\bar{k}_p}^\dagger = I \quad (3.75)$$

Hence, it follows that

$$\begin{aligned} \sum_{l=1}^M \left[ H_1^\dagger \left( \Phi_{(\bar{k}_l)} e^{-i\bar{k}_l} \tilde{\Phi}_{(\bar{k}_l)}^\dagger - \Phi_{(k_l)} e^{-ik_l} \tilde{\Phi}_{(k_l)}^\dagger \right) \right]^{-1} \\ = \sum_{p=1}^M \Phi_{(\bar{k}_p)} \omega_{\bar{k}_p}^\dagger = \sum_{p=1}^M \Phi_{(k_p)} \omega_{k_p}^\dagger \end{aligned} \quad (3.76)$$

This immediately yields expressions for  $\omega_k^\dagger$ :

$$\omega_k^\dagger = \tilde{\Phi}_{(k)}^\dagger \nu^{-1} \quad (3.77)$$

where  $\nu$  is defined as:

$$\nu = \sum_{l=1}^M H_1^\dagger \left( \Phi_{(\bar{k}_l)} e^{-i\bar{k}_l} \tilde{\Phi}_{(\bar{k}_l)}^\dagger - \Phi_{(k_l)} e^{-ik_l} \tilde{\Phi}_{(k_l)}^\dagger \right) \quad (3.78)$$

In equation (3.77), the wave number ( $k$ ) denotes both left and moving states. The substitution of equation (3.77) into equation (3.69) produces the Green's function of an infinite system:

$$\mathcal{G}_{z,z'}^{\infty} = \begin{cases} \sum_{l=1}^M \Phi_{(k_l)} e^{ik_l(z-z')} \tilde{\Phi}_{(k_l)}^{\dagger} \nu^{-1}, & z \geq z' \\ \sum_{l=1}^M \Phi_{(\bar{k}_l)} e^{i\bar{k}_l(z-z')} \tilde{\Phi}_{(\bar{k}_l)}^{\dagger} \nu^{-1}, & z \leq z' \end{cases} \quad (3.79)$$

To obtain the Green's function for a semi-infinite lead, a wave function must be added to the Green's function so that the boundary conditions at the lead's edge can be satisfied, similar to the one-dimensional example. In this case, the boundary condition stipulates that the Green's function must disappear at a particular place ( $z = z_o$ ). For this to be achieved,

$$\Delta = - \sum_{l,p=1}^M \Phi_{\bar{k}_l} e^{i\bar{k}_l(z-z_o)} \tilde{\Phi}_{(\bar{k}_l)}^{\dagger} \Phi_{(k_p)} e^{ik_p(z_o-z)} \tilde{\Phi}_{(k_p)}^{\dagger} \nu^{-1} \quad (3.80)$$

is simply added to the Green's function, equation (3.79):  $\mathcal{G} = \mathcal{G}^{\infty} + \Delta$ . This produces the surface Green's function for a semi-infinite lead moving left:

$$\mathcal{G}_L = \left( I - \sum_{l,p=1}^M \Phi_{(\bar{k}_l)} e^{-i\bar{k}_l} \tilde{\Phi}_{(\bar{k}_l)}^{\dagger} \Phi_{(k_p)} e^{ik_p} \tilde{\Phi}_{(k_p)}^{\dagger} \right) \nu^{-1} \quad (3.81)$$

and moving right:

$$\mathcal{G}_R = \left( I - \sum_{l,p=1}^M \Phi_{(k_l)} e^{ik_l} \tilde{\Phi}_{(k_l)}^\dagger \Phi_{(\bar{k}_p)} e^{-i\bar{k}_p} \tilde{\Phi}_{(\bar{k}_p)}^\dagger \right) \mathcal{V}^{-1} \quad (3.82)$$

Hence we have a flexible approach that can be used to calculate the surface Green's functions (equations (3.81) and (3.82)) for a semi-infinite crystalline electrode by utilising the numeral method in equation (3.64). In the following step, this is applied to a scattering problem.

### 3.5.2 Effective Hamiltonian of the Scattering Region

It was demonstrated in Section 3.4.2 that for a coupling matrix between surfaces of semi-infinite leads, it is possible to use the Dyson equation (3.54) for calculating the Green's function of a scatterer. Nevertheless, in general, the scattering region is not simply described as a coupling matrix between the surfaces. Hence, using the decimation technique for reducing the Hamiltonian to this type of structure is advantageous [19-20]. Although different techniques have been proposed [21- 22], for the purposes of the current thesis, the decimation technique will be used.

First, the Schrödinger equation is again considered:

$$\sum_j H_{ij} \Psi_j = E \Psi_i \quad (3.83)$$

If the  $d^{\text{th}}$  degree of freedom in the system is separated from equation (3.83), we have

$$H_{id} \Psi_d + \sum_{j \neq d} H_{ij} \Psi_j = E \Psi_i, \quad i \neq d \quad (3.84)$$

Next, the component  $\Psi_d$  can be examined utilising the latter equation where  $j = d$ ;

$$H_{dd}\Psi_d + \sum_{j \neq d} H_{dj}\Psi_j = E\Psi_d \quad (3.85)$$

According to equation (3.85)  $\Psi_d$  can be expressed as:

$$\Psi_d = \sum_{j \neq d} \frac{H_{dj}\Psi_j}{E - H_{dd}} \quad (3.86)$$

If equation (3.86) is then substituted into equation (3.84), this yields:

$$\sum_{j \neq d} \left[ H_{ij} + \frac{H_{id}H_{dj}}{E - H_{dd}} \right] \Psi_j = E\Psi_i, \quad i \neq d \quad (3.87)$$

Hence, equation (3.87) can be considered an effective equation in which the number of degrees of freedom is lowered by one in comparison to equation (3.83). Therefore, a new effective Hamiltonian ( $\tilde{H}$ ) can be introduced as

$$\tilde{H}_{ij} = H_{ij} + \frac{H_{id}H_{dj}}{E - H_{dd}} \quad (3.88)$$

This refers to the decimated Hamiltonian that is created via basic Gaussian elimination.

A noteworthy aspect of this decimated Hamiltonian is that it is highly dependent on energy, which is therefore very suited to the technique described in the last section [20].

If the decimation technique were not applied, the Hamiltonian that describes the overall system would be expressed as

$$H = \begin{pmatrix} H_L & V_L & 0 \\ V_L^\dagger & H_{scatt} & V_R \\ 0 & V_R^\dagger & H_R \end{pmatrix} \quad (3.89)$$

where  $H_L$  and  $H_R$  refer to the semi-infinite leads,  $H_{scatt}$  represents the scatterer's Hamiltonian and  $V_L$  and  $V_R$  denote the coupling Hamiltonians, which connect the original scattering region with the leads. After implementing the decimation method, an effective equivalent Hamiltonian is produced:

$$H = \begin{pmatrix} H_L & V_c \\ V_c^\dagger & H_R \end{pmatrix} \quad (3.90)$$

where  $V_c$  represents an effective coupling Hamiltonian, which thus describes the entire scattering process.

Next, the identical steps used in the one-dimensional case can be applied employing the Dyson equation (equation (3.54)). Therefore, the surface Green's functions (equations (3.81) and (3.82)) as well as effective coupling Hamiltonian from equation (3.90) describe the Green's function for the entire system:

$$G = \begin{pmatrix} \mathcal{G}_L^{-1} & V_c \\ V_c^\dagger & \mathcal{G}_R^{-1} \end{pmatrix}^{-1} = \begin{pmatrix} G_{00} & G_{01} \\ G_{10} & G_{11} \end{pmatrix} \quad (3.91)$$

### 3.5.3 Scattering Matrix

We can now proceed to calculating the scattering amplitudes. Based on the assumption that states are normalised to transport unit flux, a generalisation of the Fisher-Lee relation [16, 18, 23] provides the transmission amplitude from the left to the right lead in the form

$$\vec{t}_{hl} = \tilde{\Phi}_{(k_h)}^\dagger G_{RL}^{hl} v_L^{hl} \Phi_{(k_l)} \sqrt{\frac{|v_h|}{|v_l|}} \quad (3.92)$$

where  $\Phi_{(k_h)}$  and  $\Phi_{(k_l)}$  represent right moving state vectors in the right and left leads respectively, and  $v_h$  and  $v_l$  denote the corresponding group velocities. In a similar manner, the reflection in the left lead is:

$$\tilde{r}_{hl} = \tilde{\Phi}_{(\bar{k}_h)}^\dagger (G_L^{hl} \nu_L^{hl} - I) \Phi_{(k_l)} \sqrt{\frac{|v_h|}{|v_l|}} \quad (3.93)$$

where  $\Phi_{(\bar{k}_h)}$   $\Phi_{(k_l)}$  respectively represent a left moving and right state moving vector in the left lead. In both instances,  $\nu_{gL}$  stands for the  $\nu$  operator that equation (3.78) defines for the left lead.

Likewise, the scattering amplitudes for particles moving from the right can be defined:

$$\tilde{t}_{hl} = \tilde{\Phi}_{(\bar{k}_h)}^\dagger G_{LR}^{hl} \nu_R^{hl} \Phi_{(\bar{k}_l)} \sqrt{\frac{|v_h|}{|v_l|}} \quad (3.94)$$

$$\vec{r}_{hl} = \tilde{\Phi}_{(k_h)}^\dagger (G_R^{hl} \nu_R^{hl} - I) \Phi_{(\bar{k}_l)} \sqrt{\frac{|v_h|}{|v_l|}} \quad (3.95)$$

which are equivalent to the previous two equations, with the switching of left and right in the notation.

This allows a scattering matrix to be constructed and, by utilising the Landauer formula (equation 3.5) described in Section 3.1, the conductance can be calculated. Since this method applies for any selection of Hamiltonians  $H_0$ ,  $H_1$  and  $H_{\text{scatt}}$ , it is highly general.

### 3.6 Bibliography

1. Leon, S. J., Bica, I., & Hohn, T. (1998). *Linear algebra with applications* (Vol. 6). Upper Saddle River, NJ: Prentice Hall..
2. Landauer, R. (1957). Spatial variation of currents and fields due to localized scatterers in metallic conduction. *IBM Journal of research and development*, *1*(3), 223-231.
2. Büttiker, M., Imry, Y., Landauer, R., & Pinhas, S. (1985). Generalized many-channel conductance formula with application to small rings. *Physical Review B*, *31*(10), 6207.
3. Datta, S. (1997). *Electronic transport in mesoscopic systems*. Cambridge university press.
4. Brouwer, P. W. (1998). Scattering approach to parametric pumping. *Physical Review B*, *58*(16), R10135.
5. Finch, C. M. (2008). *An understanding of the the electrical characteristics of organic molecular devices* (Doctoral dissertation, Lancaster University).
6. Büttiker, M., Imry, Y., Landauer, R., & Pinhas, S. (1985). Generalized many-channel conductance formula with application to small rings. *Physical Review B*, *31*(10), 6207.
7. Maslyuk, V. V., Achilles, S., & Mertig, I. (2010). Spin-polarized transport and thermopower of organometallic nanocontacts. *Solid State Communications*, *150*(11-12), 505-509.

8. García-Suárez, V. M., Ferradás, R., & Ferrer, J. (2013). Impact of Fano and Breit-Wigner resonances in the thermoelectric properties of nanoscale junctions. *Physical review b*, 88(23), 235417.
9. Claughton, N. R., & Lambert, C. J. (1996). Thermoelectric properties of mesoscopic superconductors. *Physical review b*, 53(10), 6605.
10. Sivan, U., & Imry, Y. (1986). Multichannel Landauer formula for thermoelectric transport with application to thermopower near the mobility edge. *Physical review b*, 33(1), 551.
11. Hicks, L. D., & Dresselhaus, M. S. (1993). Effect of quantum-well structures on the thermoelectric figure of merit. *Physical Review B*, 47(19), 12727.
12. Goldsmid, H. J. (1964). Thermoelectric Refrigeration Plenum. *New York*.
13. Athanasopoulos, S. (2005). *Electronic properties of hybrid carbon nanotubes* (Doctoral dissertation, Lancaster University).
14. Economou, E. N. (2006). *Green's functions in quantum physics* (Vol. 7). Springer Science & Business Media.
15. Mello, P. A., Mello, P. A., Kumar, N., & Narendra Kumar, D. (2004). *Quantum transport in mesoscopic systems: complexity and statistical fluctuations: a maximum-entropy viewpoint* (Vol. 4). Oxford University Press on Demand.
16. Fisher, D. S., & Lee, P. A. (1981). Relation between conductivity and transmission matrix. *Physical Review B*, 23(12), 6851.
17. Visontai, D. (2011). Quantum and Classical Dynamics of Molecule Size Systems. *Physics Department 2013, Lancaster University*.

18. Sanvito, S. (1999). *Giant Magnetoresistance and Quantum Transport in Magnetic Hybrid Nanostructures*. Lancaster University.
19. Aoki, H. (1980). Real-space renormalisation-group theory for Anderson localisation: decimation method for electron systems. *Journal of Physics C: Solid State Physics*, 13(18), 3369.
20. Leadbeater, M., & Lambert, C. J. (1998). A decimation method for studying transport properties of disordered systems. *Annalen der physik*, 7(5-6), 498-502.
21. MacKinnon, J. G., & White, H. (1985). Some heteroskedasticity-consistent covariance matrix estimators with improved finite sample properties. *Journal of econometrics*, 29(3), 305-325.
22. Ryndyk, D. A., Gutiérrez, R., Song, B., & Cuniberti, G. (2009). Green function techniques in the treatment of quantum transport at the molecular scale. In *Energy Transfer Dynamics in Biomaterial Systems* (pp. 213-335). Springer, Berlin, Heidelberg.
23. Lambert, C. J., Hui, V. C., & Robinson, S. J. (1993). Multi-probe conductance formulae for mesoscopic superconductors. *Journal of Physics: Condensed Matter*, 5(25), 4187.

## Chapter 4

### 4. Optimised Power Harvesting in Anthracene-Based SAMs Junctions

#### 4.1 Introduction

The work in this chapter was carried out in collaboration with the group of Prof. Nicholas Long (Department of Chemistry, Imperial College London), who synthesised the anthracene molecules and Dr. Benjamin Robinson (Physics Department, Lancaster University), who conducted the experiments. In this Chapter I will present our joint experimental and theoretical work on “Optimised Power Harvesting in Anthracene-Based SAMs Junctions”, and the results presented here were published in the following paper:

*“Optimised power harvesting by controlling the pressure applied to molecular junctions”*

Xintai Wang, Ali Ismael, Ahmad Almutlg, Majed Alshammari, Alaa Al-Jobory, Abdullah Alshehab, Troy L. R. Bennett, Luke A. Wilkinson, Lesley F. Cohen, Nicholas J. Long, Benjamin J. Robinson and Colin Lambert

#### 4.2 Motivation

A major potential advantage of creating thermoelectric devices using self-assembled molecular layers is their mechanical flexibility. Previous reports have discussed the advantage of this flexibility from the perspective of facile skin attachment and the ability to avoid mechanical deformation [1, 2]. In this work, I demonstrate that the thermoelectric properties of such molecular devices can be controlled by taking

advantage of their mechanical flexibility. The thermoelectric properties of self-assembled monolayers (SAMs) fabricated from thiol terminated molecules were measured with a modified atomic force microscopy (AFM) system, and the conformation of the SAMs was controlled by regulating the loading force between the organic thin film and the probe, which changes the tilt angle at the metal-molecule interface. I tracked the thermopower shift versus the tilt angle of the SAM and showed that changes in both the electrical conductivity and the Seebeck coefficient combine to optimise the power factor at a specific angle. This optimisation of thermoelectric performance via applied pressure is confirmed through the use of my theoretical calculations and is expected to be a general method for optimising the power factor of SAMs.

### **4.3 Introduction**

In this chapter, two anthracene based molecules are investigated: **9,10**-di (4-(ethynyl)phenylthioacetate) anthracene and **1,5**-di(4-(ethynyl)phenylthioacetate) anthracene. Both molecules were synthesised at Imperial College London. The two molecules differ by the connectivity (i.e. **1-5** and **9-10**). For the sake of the simplicity, I shall refer to them as **1** and **2** in the rest of this chapter. Figure. 4.1 shows the chemical structure of molecules **1** and **2**.

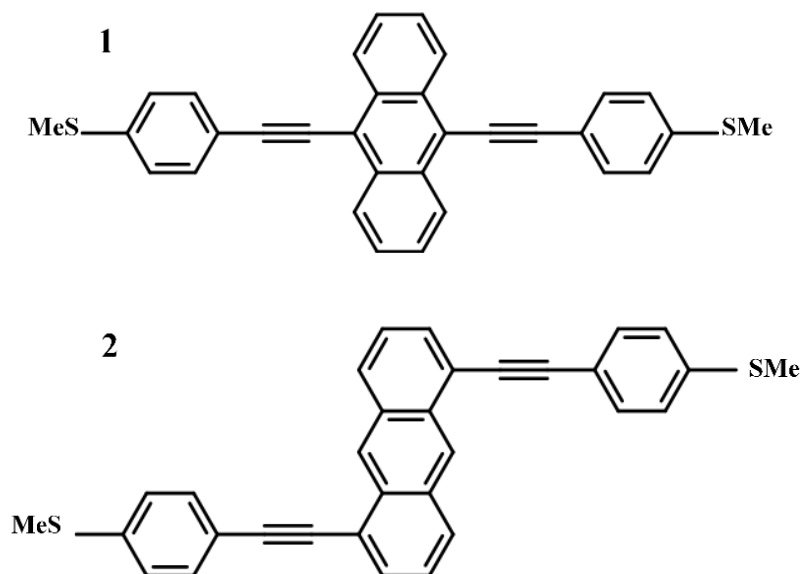


Figure 4.1. Chemical structures of molecules **1** and **2** studied in this chapter. **1** (9,10-di(4-(ethynyl)phenylthioacetate) anthracene and **2** (1,5-di(4-(ethynyl)phenylthioacetate) anthracene).

The thermoelectric properties of such molecular devices can be controlled by taking advantage of their mechanical flexibility. The thermoelectric properties of self-assembled monolayers (SAMs) fabricated from thiol terminated molecules were measured with a modified AFM system, and the conformation of the SAMs were controlled by regulating the loading force between the organic thin film and the probe, which changes the tilt angle at the metal-molecule interface.

Using the density functional code SIESTA [8], the optimum geometries of the isolated molecules **1** and **2** were obtained by relaxing the molecules until all forces on the atoms were less than  $0.01 \text{ eV} / \text{\AA}$  as shown in Figure (4.2) [6-9]. A double-zeta plus polarization orbital basis set was used along with norm-conserving pseudopotentials. An energy cut-off of 250 Rydbergs defined the real space grid and the local density approximation (LDA) was chosen for the exchange correlation functional. I also

computed results using GGA and found that the resulting transmission functions were comparable with those obtained using LDA [10, 11].

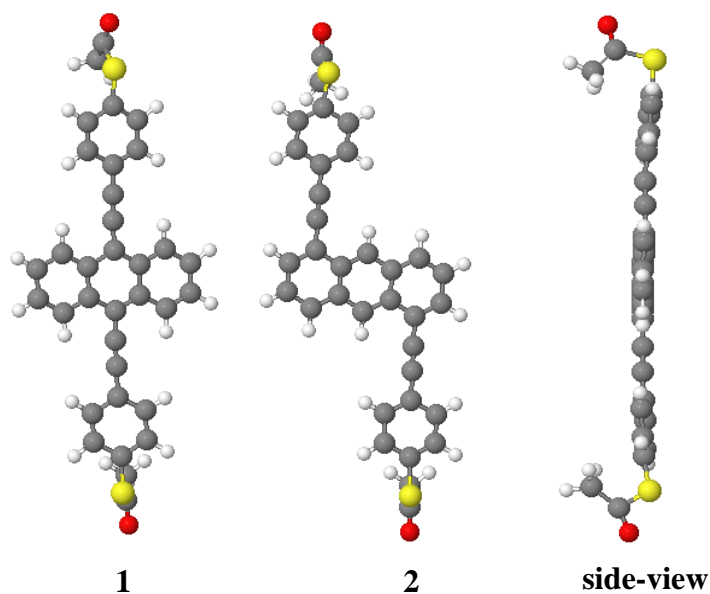


Figure 4.2. Fully relaxed isolated molecules **1** and **2**. Key: C = grey, H = white, O = red, S = yellow (synthesis reported [12, 13]).

#### 4.4 Product Rule

In this section, I will demonstrate how the Product Rule (PR) that was recently reported by Lambert and Lui [13] applies to these molecules. This method can predict the value of the conductance (high or low) without calculating transmission. Lambert and Liu state five conditions that must be satisfied in order for the product rule to work:

**1. Weak coupling:** The studied molecule should weakly couple to the electrodes, otherwise it loses its physical properties and the Product Rule is broken.

**2. Locality:** The current should flow from one reservoir to another through the studied molecule. These reservoirs are known as the source and drain.

**3. Connectivity:** The locations that the current enters and leaves the studied molecule.

**4. Mid-gap transport (Highest occupied molecular orbital (**HOMO**) - lowest occupied molecular orbital (**LUMO**)):** The energy  $E$  of electrons flowing through the molecule is located in the vicinity of the centre of the HOMO–LUMO gap and therefore transport takes place in the co-tunnelling regime. In other words, transport is usually “off-resonance”.

**5. Phase coherence:** It is an intuitive picture shows the electricity flow when the previous conditions are satisfied.

To better understand the of the Product Rule, I shall apply it to a simple molecule, naphthalene ( $C_{10}H_8$ ). Figure 4.3 shows that the naphthalene molecule has 10 carbon atoms. The PR requires two contact points, one to allow the current to enter the lattice and another to exit (I refer to them as a source and drain respectively, as shown in the top panel of Figure. 4.3).

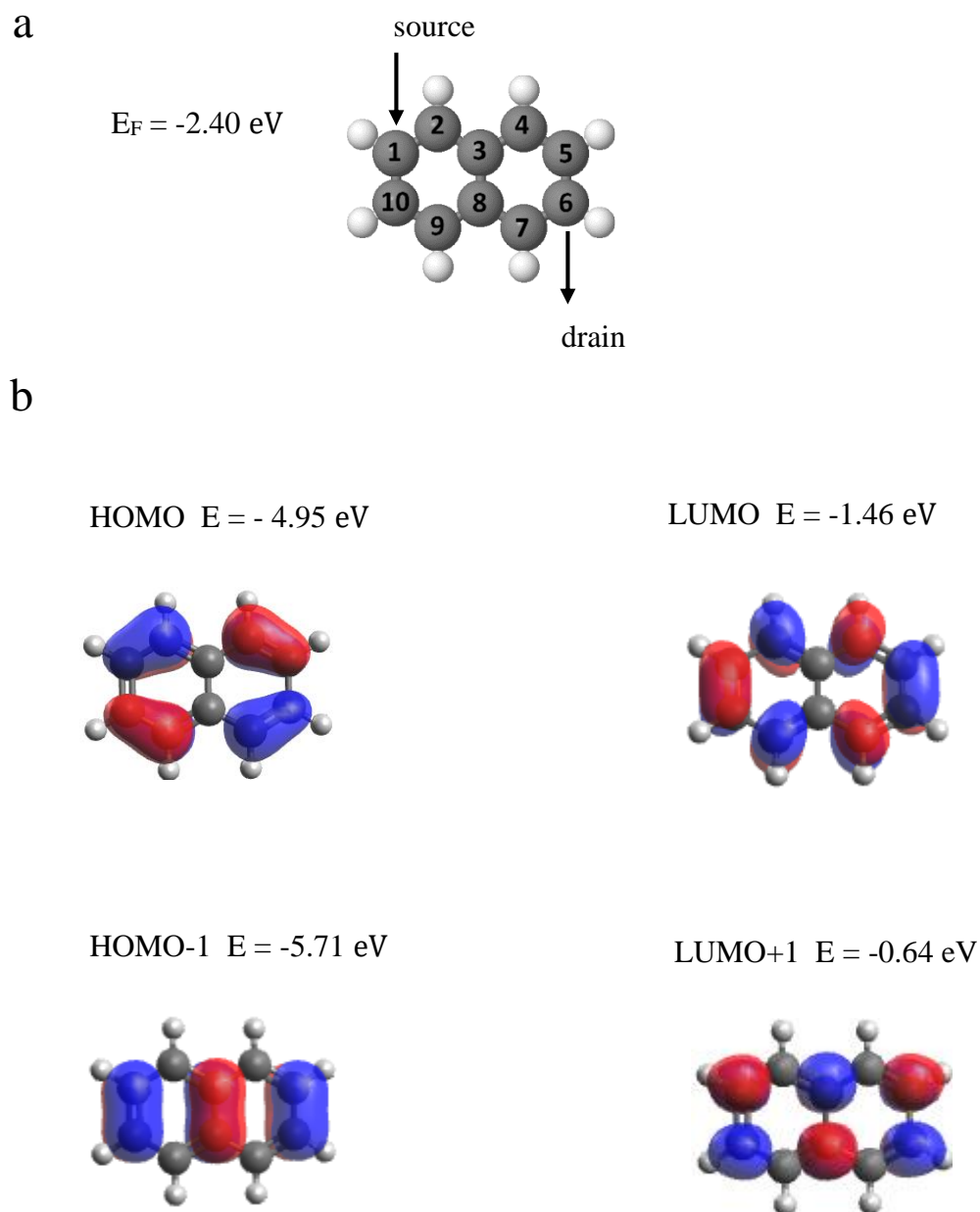


Figure 4.3: **a**: Fully optimised structure of naphthalene. **b**: Wavefunction plots of naphthalene: HOMO (Highest Occupied Molecular Orbital, LUMO (Lowest Occupied Molecular Orbitals), HOMO-1 and LUMO+1 along with their energies.

I apply the PR for 3 different connectivities (*i.e.* 3 choices of source and drain, as shown in the first column of Table 4.1) and in each case consider three regions. Region 1 covers the HOMO-1 and HOMO, region 2 covers the HOMO and LUMO, and region 3 covers the LUMO and LUMO+1 (see the last three columns of Table 4.1). Usually, the wavefunction plots show two colours, in this case red and blue; for simplicity I refer to the red as positive (+) and blue as negative (-). Based on the sign of the wavefunctions at the source and drain positions, either constructive (c) or destructive (d) constructive quantum interference for each region can be predicted. These are shown in Table 4.1.

Table 4.1: Product Rule applied to a naphthalene molecule for three different connectivities: **1-5**, **1-6** and **1-10**. PR applies on three regions: reg.1, reg.2 and reg.3, (red colour is +ive, blue -ive, c=constructive, d=destructive, H: HOMO, H-1: HOMO-1, L: LUMO, L+1: LUMO+1, G: Conductance).

Contact point	H-1	H	L	L+1	G reg.1	G reg.2	G reg.3
Case 1 ( <b>1,6</b> )	+ -5.71 eV	+ - 4.95 eV	- -1.46 eV	- -0.64 eV	d	c	d
Case 2 ( <b>1,5</b> )	+ -5.71 eV	- - 4.95 eV	- -1.46 eV	+ -0.64 eV	c	d	c
Case 3 ( <b>1,10</b> )	+ -5.71 eV	- - 4.95 eV	+ -1.46 eV	- -0.64 eV	c	c	c

**How the PR works:** first we choose our source and drain then we look at the colours of the wavefunctions at those points. For example, let us choose the source to be **1** and

the drain to be **6** (see Figure. 4.3a). For the HOMO the colours are blue and blue (at sites **1** and **6**), and blue is -ive, so we multiply -ive by -ive and the outcome is +ive ( $- \times - = +$ ). For the LUMO the colours are red and blue (**1** and **6**) and the multiplication outcome is -ive ( $+ \times - = -$ ). The product rule states that different signs mean constructive quantum interference (CQI), whereas same signs mean destructive quantum interference (DQI). So in this case we expect constructive QI.

Now, by applying the PR to the naphthalene molecule with **1-6** connectivity one can notice two cases of DQI for regions 1 and 3, and one case of CQI for region 2. In contrast, connectivity **1-5** yields two cases of CQI and one DQI, while **1-10** connectivity yields three cases of CQI.

In this example, I chose 3 connectivities, however, due to the symmetry of naphthalene molecule choosing other connectivities would yield the same results. In other words, **5-10** connectivity resembles ( $=$ ) **1-6**, **1-5 = 6-10**, **1-10 = 5-6** and so on. Table 4.1 summarises the PR of the naphthalene molecule for three different connectivities.

#### **4.5 Frontier orbitals of molecules 1 and 2**

In order to apply the PR discussed in section 4.4 to molecules **1** and **2** I show the HOMO, LUMO, HOMO-1 and LUMO+1 wavefunctions in Figures 4.4 and 4.5.

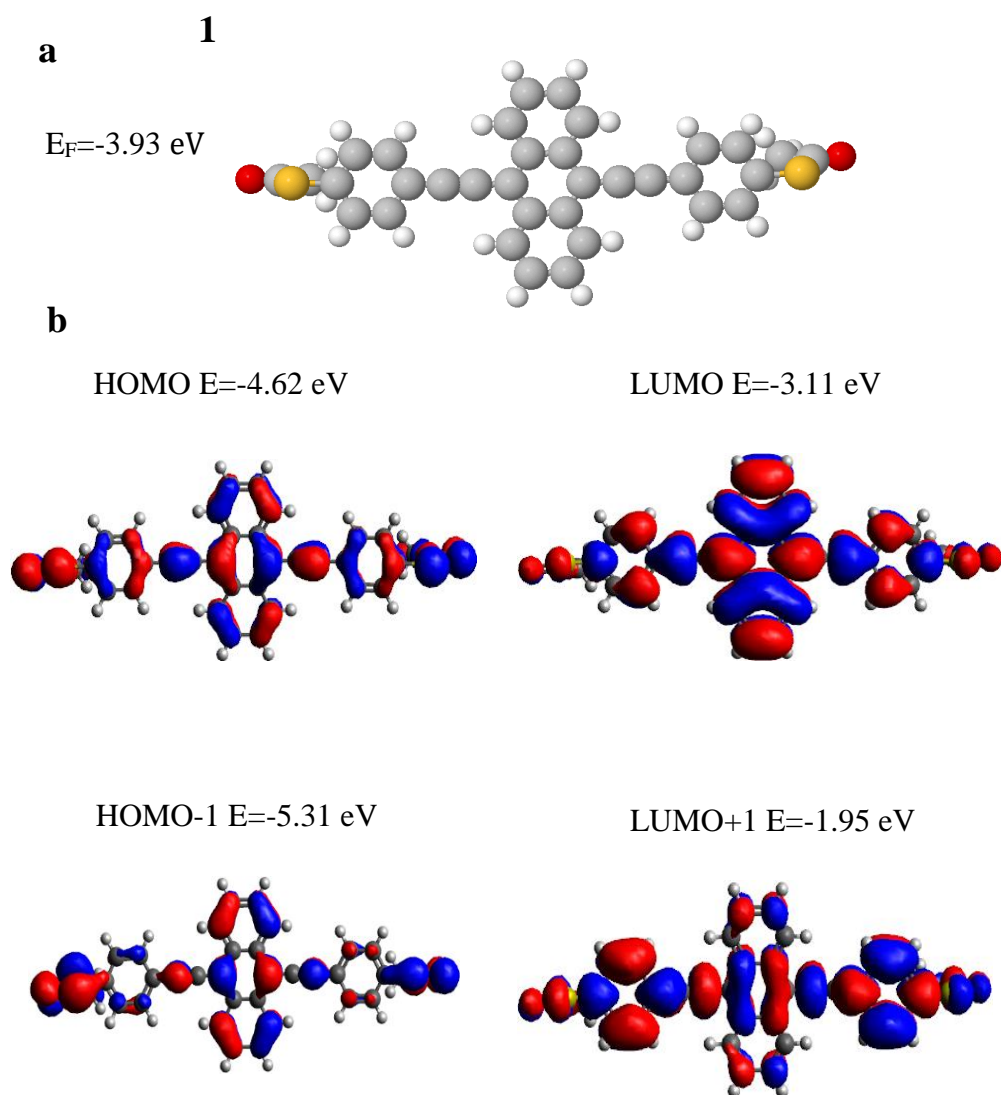
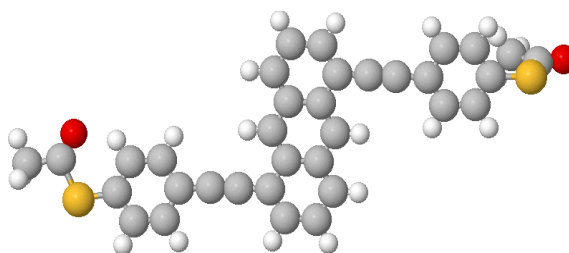


Figure 4.4: **a**: Fully optimised conformation of **1**. **b**: Wavefunction plots of **1** for HOMO (Highest Occupied Molecular Orbitals), LUMO (Lowest Occupied Molecular Orbitals), HOMO-1 and LUMO+1 along with their energies.

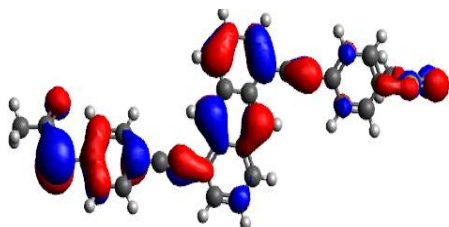
**a** **2**

$E_F = -3.706$  eV

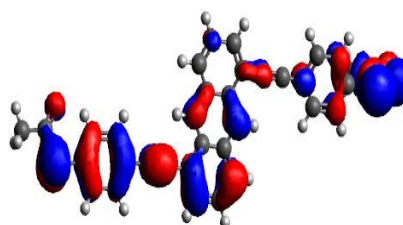


**b**

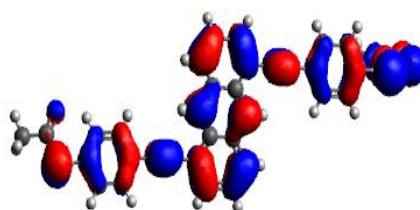
HOMO  $E = -4.59$  eV



LUMO  $E = -3.13$  eV



HOMO-1  $E = -5.01$  eV



LUMO+1  $E = -1.95$  eV

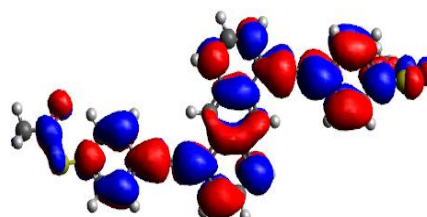


Figure 4.5: **a**: Fully optimised conformation of **2**. **b**: Wavefunction plots of **2** for HOMO (Highest Occupied Molecule Orbitals), LUMO (Lowest Occupied Molecule Orbitals), HOMO-1 and LUMO+1 along with their energies.

Information from Figures 4.4 and 4.5 is then listed in Tables 4.2 and 4.3 along with the results of applying the product rule. Constructive quantum interference is predicted in the HOMO-LUMO gap (region 2) for both molecules.

Table 4.2: Product Rule of **1**. PR applies on three regions: reg.1, reg.2 and reg.3, (red colour is +ive, blue -ive, c=constructive and d=destructive).

Molecule	H-1	H	L	L+1	G reg.1	G reg.2	G reg.3
<b>1</b>	-	-	+	-	d	c	c
Energy	-5.31 eV	-4.62 eV	-3.11 eV	-1.95 eV	$E_F = -3.93$ eV		

Table 4.3: Product Rule of **2**. PR applies on three regions: reg.1, reg.2 and reg.3, (red colour is +ive, blue -ive, c=constructive and d=destructive).

Molecule	H-1	H	L	L+1	G reg.1	G reg.2	G reg.3
<b>2</b>	-	-	+	-	d	c	c
Energy	-5.01 eV	-4.59 eV	-3.13 eV	-1.95 eV	$E_F = -3.706$ eV		

#### 4.6 Binding energy of molecules on Au-substrate

To calculate the optimum binding distance between thiol anchor groups and Au (111) surfaces, I used DFT and the counterpoise method [3], which removes basis set superposition errors (BSSE) [4]. The binding distance  $d$  is defined as the distance between the gold surface and the S terminus of the thiol group. Here, compound **1** is defined as entity A and the gold electrode as entity B. The ground state energy of the total system is calculated using SIESTA and is denoted  $E_{AB}^{AB}$ . The energy of each entity

is then calculated in a fixed basis, which is achieved using ghost atoms in SIESTA. Hence, the energy of **1** in the presence of the fixed basis is defined as  $E_A^{AB}$  and the energy of the gold as  $E_B^{AB}$ . The binding energy (BE) is then calculated using the following equation:

$$\text{Binding Energy} = E_{AB}^{AB} - E_A^{AB} - E_B^{AB} \quad (4.1)$$

We then considered the nature of the binding depending on the gold surface structure. We calculated the binding to a Au pyramid on a surface with the S atom binding at a ‘top’ site and then varied the binding distance  $d$ . Figure 4.6 (left) shows that a value of  $d = 2.4 \text{ \AA}$  gives the optimum distance, at with a binding energy of approximately -0.8 eV. As expected, the thiol anchor group binds favourably to under-coordinated gold atoms.

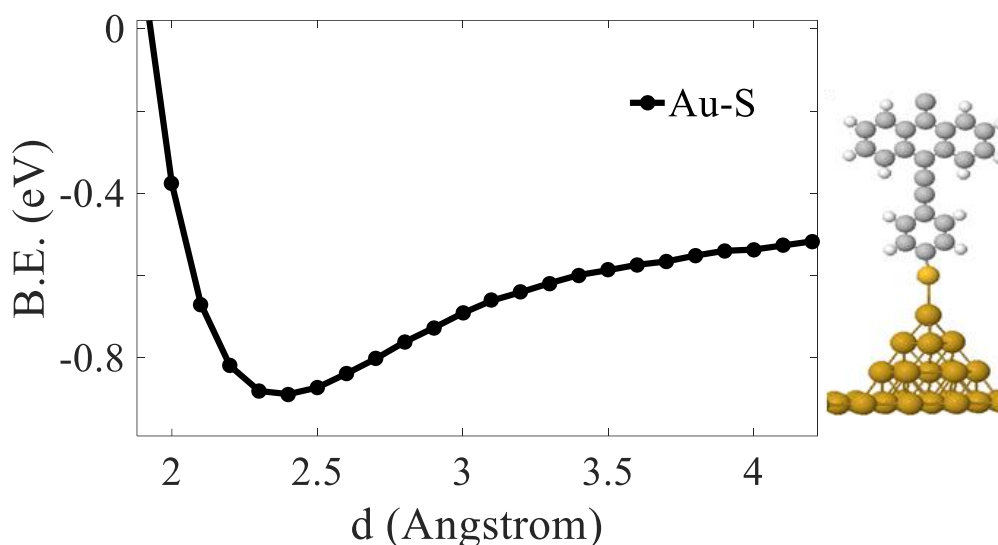


Figure 4.6. Example binding energy plot of **1**, for thiol anchor Au-S (left), with its idealised ad-atom configuration at the Au lead interface Au-S. Key: C = grey, H = white, S = light yellow, Au = dark yellow.

## 4.7 Optimised DFT Structures of Compounds in their Junctions

Using the optimised structures and geometries for the compounds obtained as described in section 4.1, I again employed the SIESTA code to calculate self-consistent optimised geometries, ground state Hamiltonians and overlap matrix elements for each metal-molecule-metal junction. Leads were modelled as 625 atom slabs. The optimised structures were then used to compute the transmission curve for each compound. The DFT optimised geometries are shown in Figure 4.7. Note: there is a tilt angle range for each compound, which is presented in section 4.8.

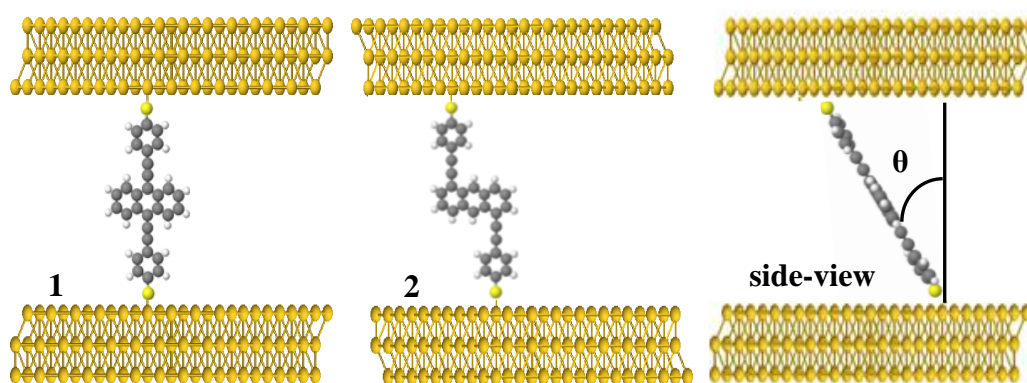


Figure 4.7. Optimised structures of molecules **1** and **2**. Tilt angle (side-view)

## 4.8 The tilt angle ( $\theta$ )

In this section, I determine the tilt angle  $\theta$  of each compound on a gold substrate, which corresponds to the experimentally measured most-probable break-off distance. Table 4.4 shows a range of tilt angles calculated from the film thickness for each molecule. Break-off distance values suggest that compound **1** tilts with angle  $\theta$  ranging from  $57^\circ$  to  $61^\circ$  and compound **2** from  $55^\circ$  to  $63^\circ$ , as shown in Figure 4.8.

Table 4.4: Experimental break-off distance and equivalent theoretical tilt angle ( $\theta$ )

Compound	Experimental film thickness (nm)	Experimental film roughness (nm)	Equivalent experimental tilt angle ( $\theta$ )	Equivalent theoretical tilt angle ( $\theta$ )
<b>1</b>	1.12	0.43	57°-61°	57°-61°
<b>2</b>	1.19	0.09	55°-63°	55°-63°

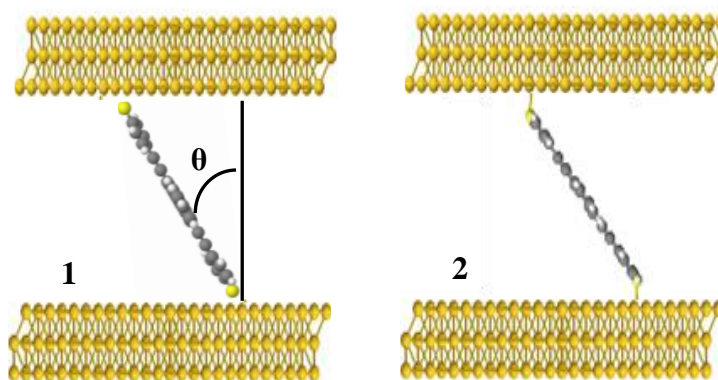


Figure 4.8. Optimised structures of molecules **1** and **2**.

#### 4.9 Beyond the optimised tilt angle ( $\theta$ )

After finding the optimised tilt angle for molecule **1** and molecule **2**, these angles were varied by up to 80° when measuring the conductance, and up to 70° for Seebeck measurements. The difference between  $G$  and  $S$  tilt angles arose from the need to heat up the tip during the Seebeck measurements. The theory models the increase in the tilt angle up to 85° , as shown in Figure 4.9.

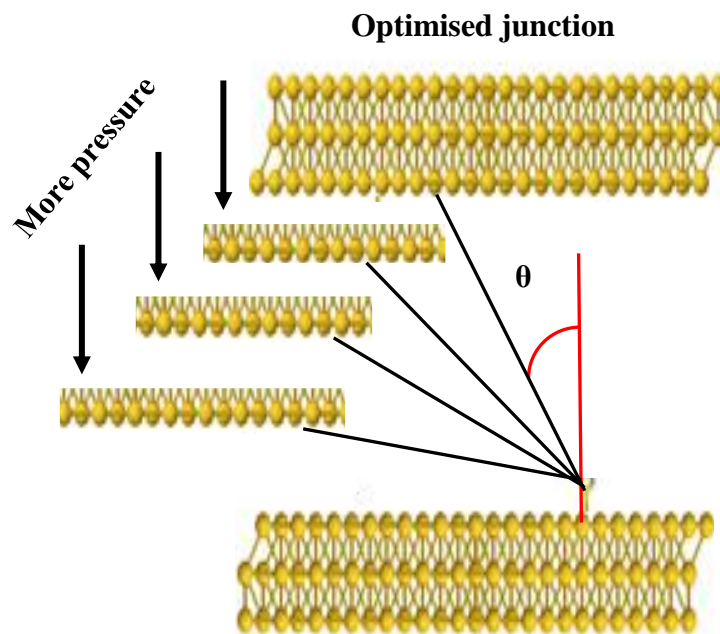


Figure 4.9. Schematic illustrations of modelling an increase in the tilt angle (pressure model).

#### 4.10 DFT Calculations

In the following transport calculations, the ground state Hamiltonian and optimized geometry of each compound was obtained using density functional theory (DFT) [12]. The local density approximation (LDA) exchange correlation functional was used along with double zeta polarized (DZP) basis sets and norm conserving pseudo potentials. The real space grid was defined by a plane wave cut-off of 250 Ry. The geometry optimization was carried out to a force tolerance of 0.01 eV/Å. This process was repeated for a unit cell with the molecule between gold electrodes where the optimized distance between Au and the thiol anchor group was found to be 2.4 Å. From the ground state Hamiltonian, the transmission coefficient, the room temperature electrical

conductance  $G$  and Seebeck coefficient  $S$  were obtained, as described in the sections below. Although we model here the properties of a single molecule in the junction, other studies [13] have shown that the calculated conductance of a SAM differs only slightly from that of single molecules.

Gollum 2 computes the zero-voltage thermo-electric properties of the junction as a function of temperature. Such properties include the Peltier Coefficient, the Thermal conductance, the Thermopower, the Seebeck Coefficient and the Figure of Merit.

Important improvements now enable the user to calculate those spin-dependent thermo-electric properties over a temperature sweep or an energy sweep based upon the Fermi Energy, and under the assumption of charge-spin separation or non-separation.

Gollum starts from a mean-field Hamiltonian provided either by the user or by an outside material-specific DFT code. It then computes the scattering matrix and its related transport properties. When finite voltages are applied to the electrodes, they change the distribution of incoming and outgoing electrons and therefore the underlying Hamiltonian.

#### **4.11 Transport calculations**

The transmission coefficient curves  $T(E)$ , obtained using the Gollum [55] transport code, were calculated for molecules **1** and **2** based on the pressure model (see Figure. 4.9). The HOMO resonance is predicted to be pinned near the Fermi level of the electrodes for the two molecules **1** and **2**, however, I set the Fermi level to be in the mid gap at approximately 0.5 eV (black dashed line), as shown in Figures 4.10 and 4.11.

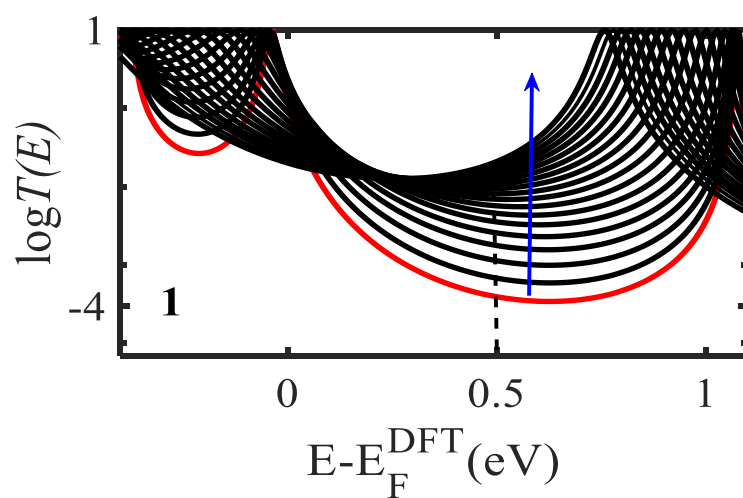


Figure 4.10. Zero bias transmission coefficient  $T(E)$  of molecule **1** as a function of pressure. The tilt angle varies from approximately  $55^\circ$  (red curve, light pressure) to  $80^\circ$ . (The blue arrow points towards heavy pressure; for clarity, not all curves are shown).

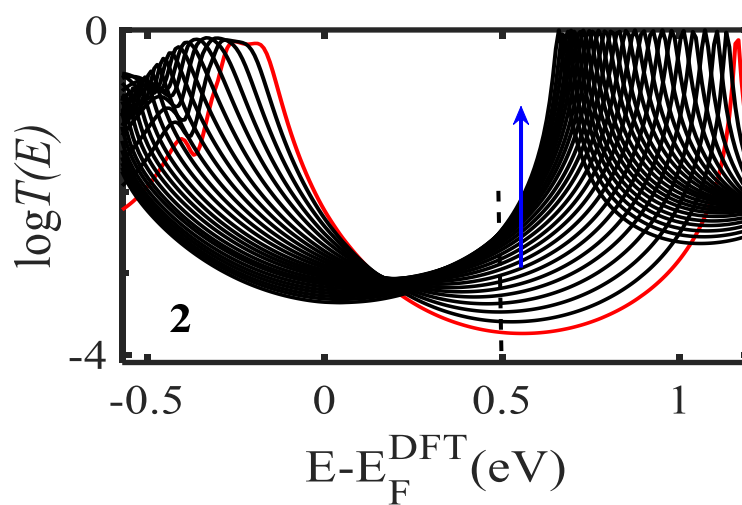


Figure 4.11. Zero bias transmission coefficient  $T(E)$  of molecule **2** as a function of pressure. The tilt angle varies from approximately  $55^\circ$  (red curve, light pressure) to  $80^\circ$ . (The blue arrow points towards heavy pressure; for clarity, not all curves are shown).

Figures. 4.10 and 4.11 above show a linear relation between the tilt angle  $\theta$  and the transmission coefficient  $T(E)$ , meaning the more pressure applied the higher the conductance obtained.

#### 4.12 Seebeck Coefficient Calculations

After computing the electronic transmission coefficients  $T(E)$  for the two molecules, thermoelectric properties such as their Seebeck coefficient  $S$  were computed.

To calculate the Seebeck coefficient of **1** and **2** molecular junctions, it is useful to introduce the non-normalised probability distribution  $P(E)$  defined by

$$P(E) = -T(E) \frac{df(E)}{dE} \quad (4.2)$$

where  $f(E)$  is the Fermi-Dirac function and  $T(E)$  are the transmission coefficients and whose moments  $L_i$  are denoted as follows

$$L_i = \int dE P(E) (E - E_F)^i \quad (4.3)$$

where  $E_F$  is the Fermi energy. The Seebeck coefficient  $S$ , is then given by

$$S(T) = -\frac{1}{|e|T} \frac{L_1}{L_0} \quad (4.4)$$

where  $e$  is the electronic charge.

Figures. 4.12 and 4.13 show the thermopower  $S$  evaluated at room temperature for different energy ranges  $E_F - E_F^{DFT}$  as a function of pressure.

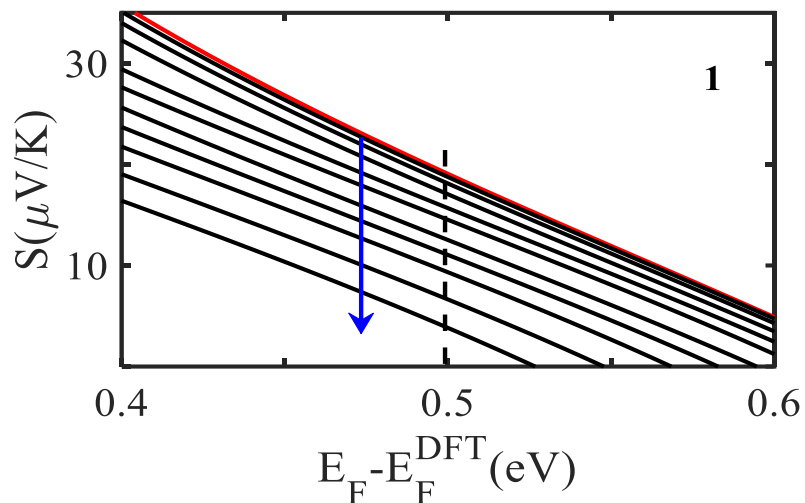


Figure 4.12. Seebeck coefficient  $S$  of molecule **1** as a function of pressure. The tilt angle varies from approximately  $55^\circ$  (red curve, light pressure) to  $80^\circ$ . (The blue arrow points towards heavy pressure; for clarity, not all curves are shown).

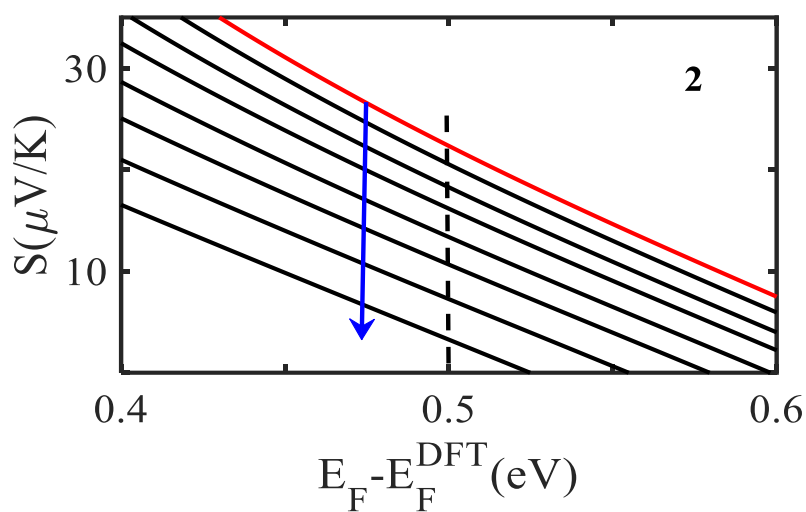


Figure 4.13 Seebeck coefficient  $S$  of molecule **2** as a function of pressure. The tilt angle varies from approximately  $55^\circ$  (red curve, light pressure) to  $80^\circ$ . (The blue arrow points towards heavy pressure; for clarity, not all curves are shown).

Figures. (4.12) and (4.13) above show a clear decrease in the Seebeck coefficient  $S$  with increased tilt angle  $\theta$ , meaning the more pressure is applied the lower the Seebeck coefficient obtained. This is the opposite behaviour to the transmission coefficient (see Figures. (4.10) and (4.11) above).

### 4.13 Mechanical Gating Charge Transport in Molecular Junctions

In this section, the  $I - V$  curves were calculated for each tilt angle for both molecules **1** and **2** as shown in Figure 4.14. The next step is to divide  $I$  by  $V$  to obtain  $I/V$  for **1** and **2** as shown in Figure 4.15.

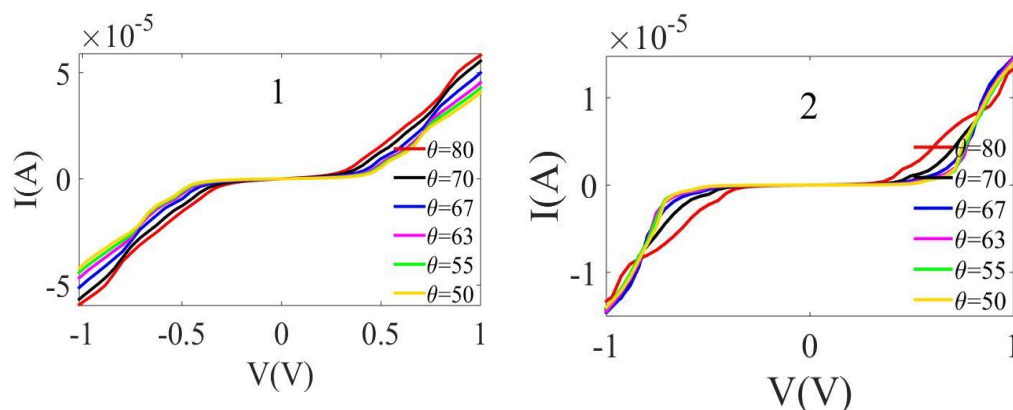


Figure 4.14. Current transport in molecular junctions **1** and **2**. Current plotted versus bias voltage for **1** and **2** (left and right respectively).

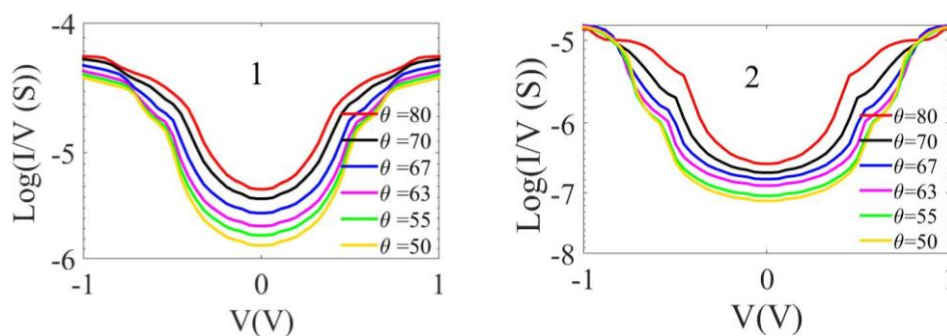


Figure 4.15.  $I/V$  plotted versus bias voltage for **1** and **2** (left and right respectively).

#### 4.14 2-D Histogram

In this section 2-D histograms have been generated for both **1** and **2**. Figure 4.16 shows how the tilt angle varies with the applied bias voltage for **1** and **2**. These plots indicate that molecule **2** is more sensitive to the bias voltage than molecule **1**. Finally, Figure 4.16 shows a two-dimensional of  $I/V$  plotted versus the bias voltage for both **1** and **2**.

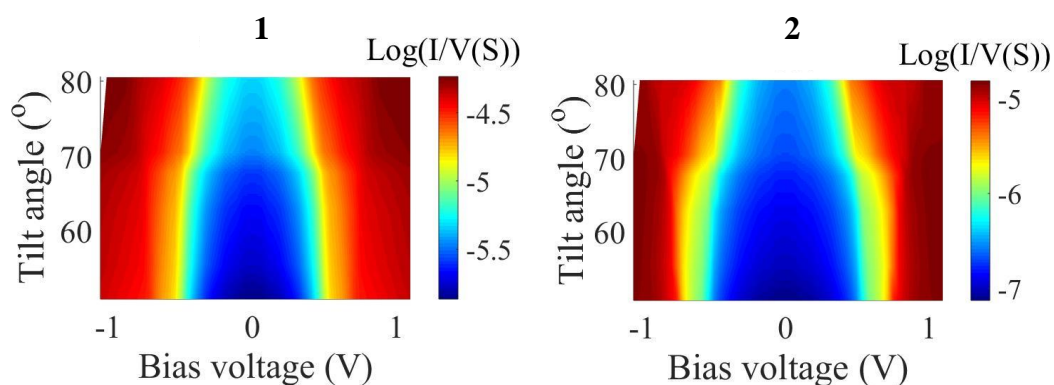


Figure 4.16. Two-dimensional visualization of  $I/V$  versus bias voltage for **1** and **2**.

#### 4.15 Theory Versus Experiment

As mentioned above, this work is a joint study between theory and experiment. In this section, I will make comparisons between theory and experiment for some electronic and thermoelectric properties including conductance  $G$ , the conductance ratio  $\frac{G_1}{G_2}$ , Seebeck coefficient  $S$ , Power factor  $P$  and charge transport.

## 4.16 Conductance G

Figures 4.17 and 4.18 present theoretical calculations of the transmission coefficient  $T(E)$ , for **1** and **2**, and show how  $T(E)$ , increases with increased tilt angle  $\theta$ . Here, the conductance is calculated using the Landauer formula. Figure. 4.17 shows how  $G$  changes with increasing  $\theta$ .

Figure. 4.17 also shows a comparison between the DFT-predicted conductance (brown-circle), and measured conductance (red-circle), by AFM for SAM **1**. Since the number of molecules contacting the probe increases with increasing loading force (tilt angle  $\theta$ ) [50, 51], our collaborators calibrated the measured conductance at different loading force approximately  $57^\circ$ ,  $65^\circ$ ,  $70^\circ$  and  $80^\circ$ . It is worth mentioning, experimentalists calibrated the measured conductance to the single molecular scale. Figure. 4.17 proves my simulations to predict the measurement trend very well.

For SAM **2**, conductance measured at different loading force approximately  $57^\circ$ ,  $65^\circ$ ,  $70^\circ$  and  $80^\circ$ . Again, my simulations predict the measurement trend as shown in Figure. 4.13. A clear enhancement in electrical conductivity is observed as the tilt angle increases. The experimental measurements were made at four different tilt angles for **1** and five for **2** (excluding vdW gap), and are compared with DFT simulations over a range of tilt angles (see Figures 4.17,4.18). My simulations reveal a gradual enhancement in electrical conductance with increasing tilt angle, which is in excellent agreement with the measurements shown in Figures. 4.17 and 4.18.

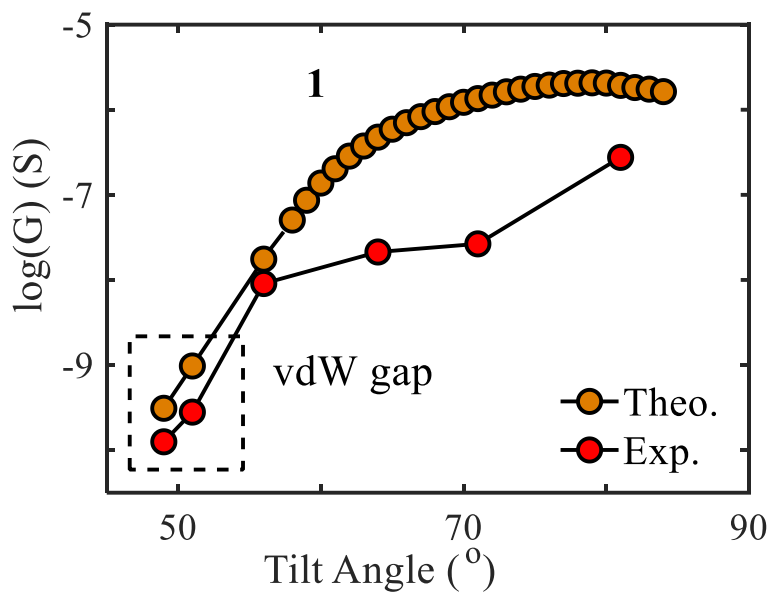


Figure 4.17. Electrical conductance of SAM of molecule **1** at different tilt angles  $\theta$ , including a comparison between theory and experiment.

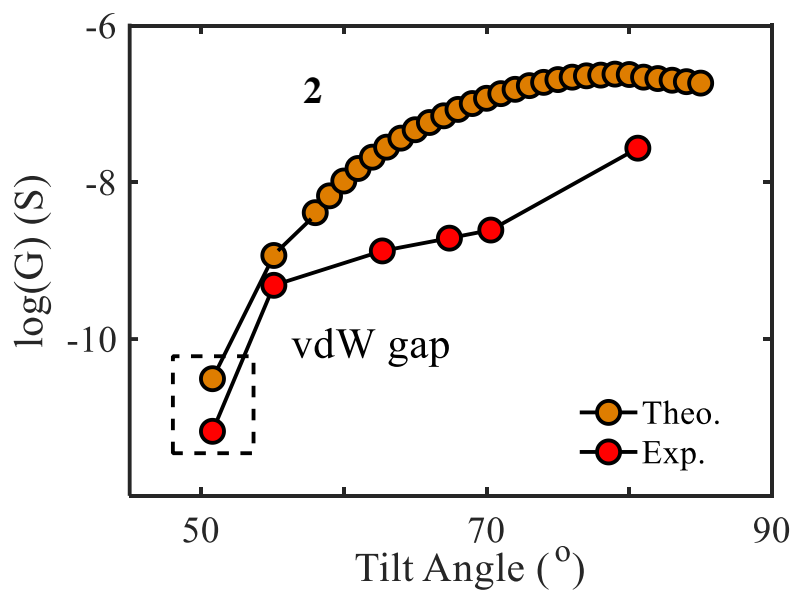


Figure 4.18. Electrical conductance of SAM of molecule **2** at different tilt angles  $\theta$ , including a comparison between theory and experiment.

#### 4.17 The Conductance Ratio $\frac{G_1}{G_2}$

The Magic Ratio Theory (MRT) [52-54], provides an intuitive way to predict the conductance ratio of molecular junctions with different connectivities to a large conjugated  $\pi$  system. MRT predicts that the conductance ratio  $\frac{G_1}{G_2}$  of SAMs **1** and **2**, should be approximately 16, in agreement with recent experiments [45].

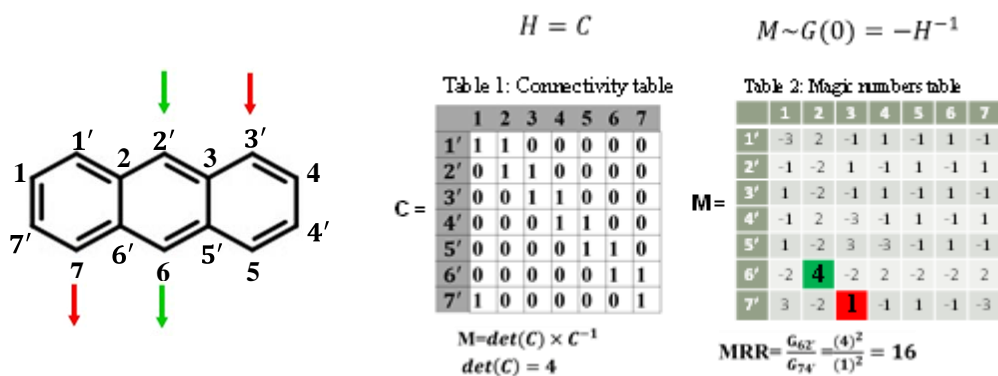


Figure 2.19. A lattice of sites representing anthracene. The connectivity table of anthracene.

Figure 4.20 is a plot of experimentally measured and theoretically predicted values of  $\frac{G_1}{G_2}$  at different tilt angles. Theory predicts that the conductance ratio is  $\sim 16$  when SAMs are in their natural form (tilt angle,  $\theta \approx 55^\circ$ ), and decreases slightly (to  $\sim 14$ ) as the tilt angle is increased (brown-circles). The experimental results exhibit a similar decreasing trend in this ratio versus the tilt angle, but with a larger decrease in the intensity (18.5-10, red-circles). This reduction in the conductance ratio is due to enhancement of intermolecular interactions that arise because of the larger loading force applied by the tip, which acts to quench the conductance ratio between the two SAMs.

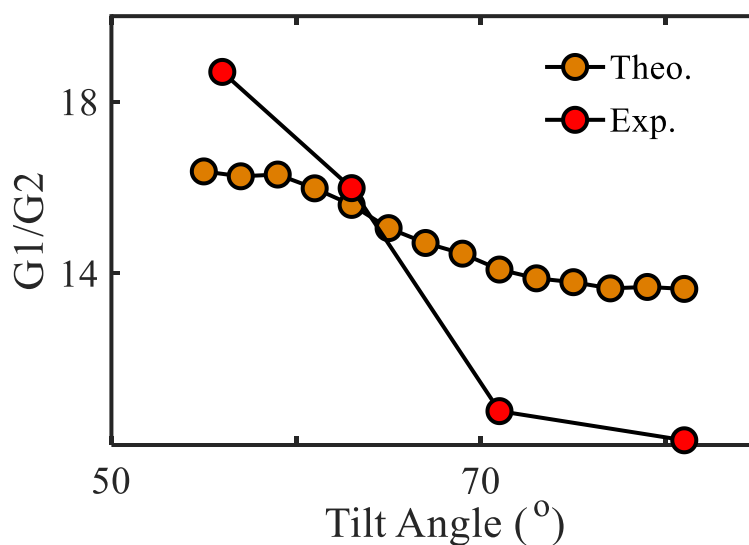


Figure 4.20. Conductance ratio between SAMs of molecule **1** and molecule **2** at different tilt angle.

#### 4.18 Seebeck Coefficient

The third comparison to be made is for the Seebeck coefficient  $S$ . Theoretical simulations predict a decrease in  $S$  when the tilt angle  $\theta$  increases as shown in Figures. 4.21 and 4.22 above. The Seebeck coefficient of the SAMs were measured using a thermoelectric force microscopy (ThEFM) system, (for more detail see [38]).

Figures. 4.21 and 4.22 show a clear decrease in the Seebeck coefficient as the tilt angle increases for SAMs of **1** and **2**. The DFT calculations exhibit a smooth reduction of the Seebeck value and an increase in conductance with increasing  $\theta$  for both SAMs, which agrees with the measured experimental trends.

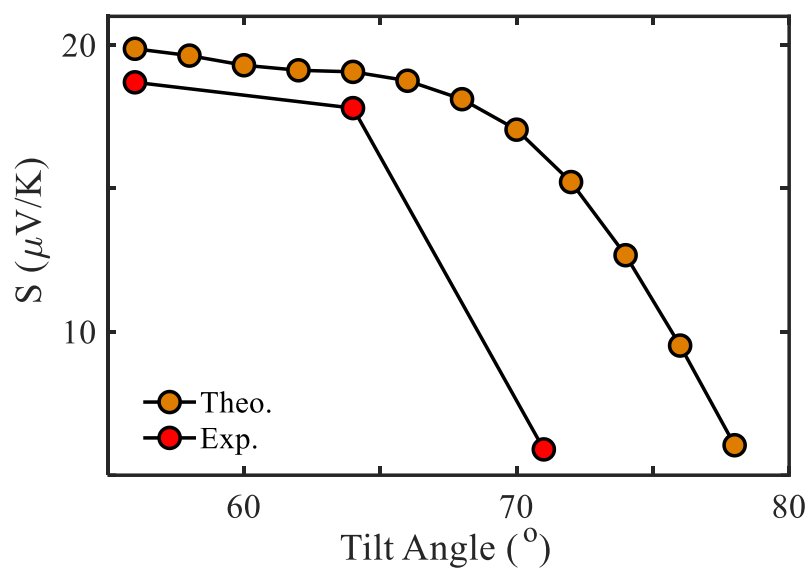


Figure 4.21. Seebeck coefficient of SAM of **1** at different tilt angles.

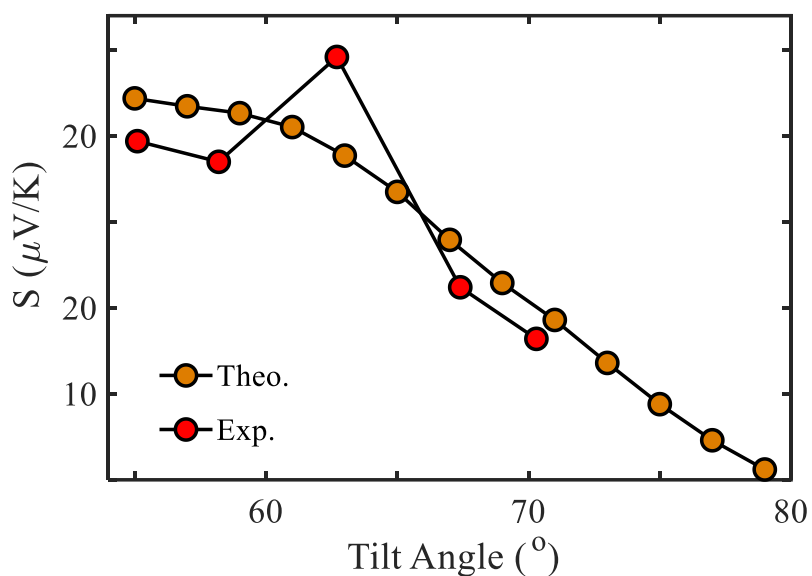


Figure 4.22 Seebeck coefficient of SAM of **2** at different tilt angles.

#### 4.19 Power Factor

The fourth parameter to be compared is the power factor of the molecular junction, defined as  $P = G S^2$ , which is calculated for SAMs of **1** and **2** at different tilt angles both experimentally and theoretically as shown Figures. 4.23 and 4.24. At low tilt angles (SAMs in their native form, with a tilt angle of  $\theta = 55^\circ$ ), the power factor is

limited by the electrical conductance of the junction,  $G$ , whereas at high tilt angles (where the SAMs are compressed by the probe), the power factor is limited by the Seebeck coefficient  $S$ .

At intermediate the tilt angles ( $\theta = 65^\circ$ ) the power factor is optimised. Figures 4.23 and 4.24 show that as the angle increases from approximately  $55^\circ$  to  $80^\circ$ , the transmission coefficient at the Fermi energy (and hence the conductance  $G$ ) increases, but the slope at the Fermi energy (and hence the Seebeck coefficient  $S$ ) decreases. Since the power factor is a product of  $G$  and  $S^2$ , there is a competition between these two opposing trends and an optimum angle at which the product is maximised. The crucial point is that pressure (tilt angle) can be used to tune the power factor, which we expect to be a generic property of SAMs. The precise value of the optimum angle, will of course depend on the chemical makeup of the monolayer and can only be obtained through a detailed DFT simulation.

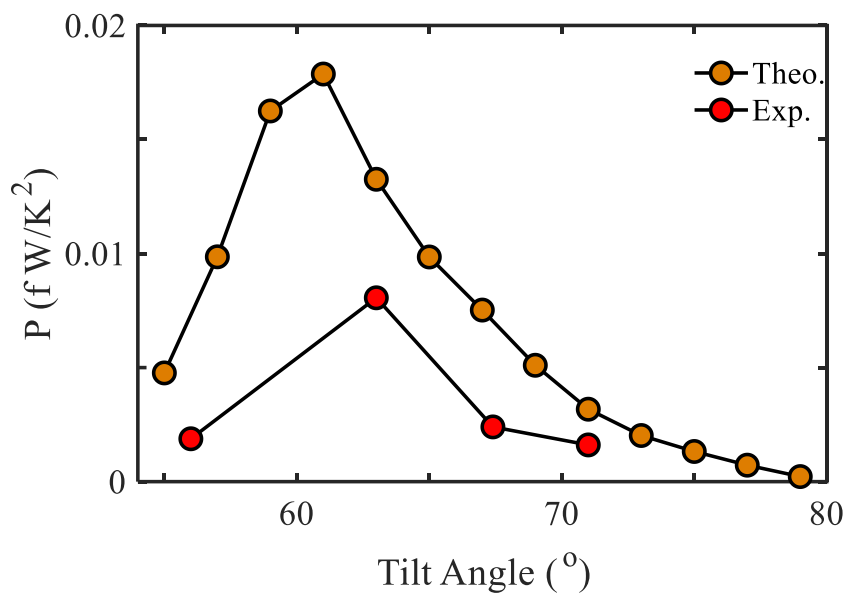


Figure 4.23. The experimentally measured and theoretical predicted power factor of a SAM of molecule 1.

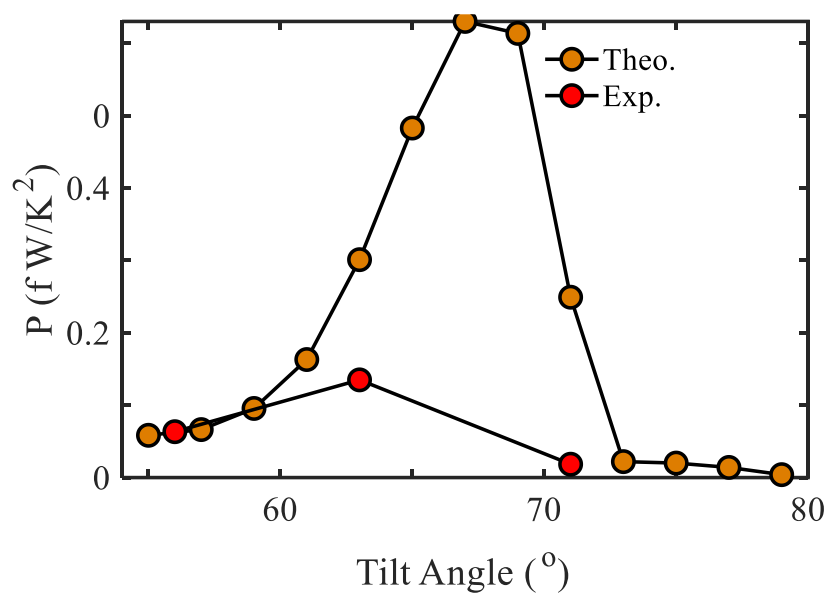


Figure 4.24. The experimentally measured and theoretical predicted power factor of a SAM of molecule 2

## 4.20 Charge Transport

The final parameter to be compared is the charge transport of the molecular junction. Figure 4.25 shows that charge transport at finite biases through the SAMs is also sensitive to the tilt angle. Increasing the applied pressure leads to a higher conductance and this behaviour is present at finite biases in Figure 4.25 both experimentally and theoretically.

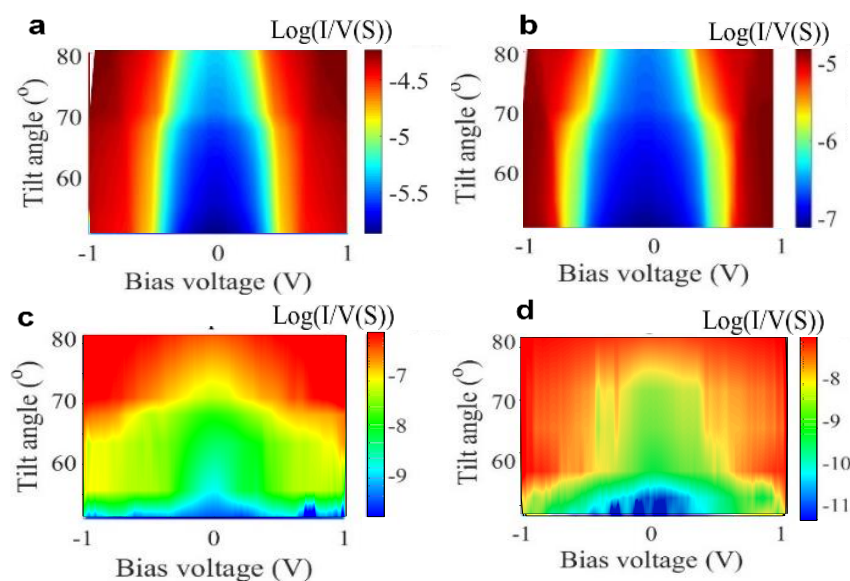


Figure 4.25. Mechanical gating of charge transport in molecular junctions. Two-dimensional visualization of  $I/V$  versus bias voltage for SAMs of **1** and **2**. The top panels (a-b) are DFT calculations, while the lower panels (c-d) are experimental results.

## 4. 11 Conclusions

In this chapter, I have demonstrated that both the Seebeck coefficient  $S$  and electrical conductivity  $G$  of anthracene-SAM-based thermoelectric junctions can be effectively tuned through variation of an external applied pressure on two different molecular wires **1** and **2**. Furthermore, I show that the power factor  $P$  of these systems can be

optimised through controlling the tilt-angle  $\theta$  between a monolayer and its underlying substrate, with the application of 'intermediate' levels of pressure demonstrating the highest power factors. This work not only increases our understanding of how thermal voltages can be conducted through ultra-thin film materials, but also opens the way towards new methods of optimising the thermoelectrical performance of organic devices through controlling the conformation of their self-assembled monolayers. I am currently examining the tilt-angle dependence of electrical conductivity and Seebeck coefficient of SAMs formed from molecules with different structures to probe whether altering the molecule-substrate interface can achieve higher power factors.

## 4.21 Bibliography

1. Heo, J. S., Eom, J., Kim, Y. H., & Park, S. K. (2018). Recent progress of textile-based wearable electronics: a comprehensive review of materials, devices, and applications. *Small*, *14*(3), 1703034.
2. Zhang, Y., & Park, S. J. (2019). Flexible organic thermoelectric materials and devices for wearable green energy harvesting. *Polymers*, *11*(5), 909.
3. Reddy, P., Jang, S. Y., Segalman, R. A., & Majumdar, A. (2007). Thermoelectricity in molecular junctions. *Science*, *315*(5818), 1568-1571.
4. Bergfield, J. P., & Stafford, C. A. (2009). Thermoelectric signatures of coherent transport in single-molecule heterojunctions. *Nano letters*, *9*(8), 3072-3076.
5. Li, Q., Strange, M., Duchemin, I., Donadio, D., & Solomon, G. C. (2017). A strategy to suppress phonon transport in molecular junctions using  $\pi$ -stacked systems. *The Journal of Physical Chemistry C*, *121*(13), 7175-7182.
6. Zhang, Y., & Park, S. J. (2017). Enhanced interfacial interaction by grafting carboxylated-macromolecular chains on nanodiamond surfaces for epoxy-based thermosets. *Journal of Polymer Science Part B: Polymer Physics*, *55*(24), 1890-1898.
7. Sangtarash, S., Sadeghi, H., & Lambert, C. J. (2018). Connectivity-driven bi-thermoelectricity in heteroatom-substituted molecular junctions. *Physical Chemistry Chemical Physics*, *20*(14), 9630-9637.
8. Rincón-García, L., Ismael, A. K., Evangeli, C., Grace, I., Rubio-Bollinger, G., Porfyakis, K., ... & Lambert, C. J. (2016). Molecular design and control of fullerene-based bi-thermoelectric materials. *Nature materials*, *15*(3), 289-293.

9. Tan, A., Sadat, S., & Reddy, P. (2010). Measurement of thermopower and current-voltage characteristics of molecular junctions to identify orbital alignment. *Applied Physics Letters*, 96(1), 013110.
10. Ismael, A. K., Wang, K., Vezzoli, A., Al-Khaykane, M. K., Gallagher, H. E., Grace, I. M., ... & Higgins, S. J. (2017). Side-Group-Mediated Mechanical Conductance Switching in Molecular Junctions. *Angewandte Chemie International Edition*, 56(48), 15378-15382.
11. Al-Galiby, Q. H., Sadeghi, H., Algharagholy, L. A., Grace, I., & Lambert, C. (2016). Tuning the thermoelectric properties of metallo-porphyrins. *Nanoscale*, 8(4), 2428-2433.
12. Herrero, I. L., Ismael, A. K., Milan, D. C., Vezzoli, A., Martín, S., González-Orive, A., ... & Cea, P. (2018). Unconventional single-molecule conductance behavior for a new heterocyclic anchoring group: pyrazolyl. *The journal of physical chemistry letters*, 9(18), 5364-5372.
13. Cui, L., Miao, R., Jiang, C., Meyhofer, E., & Reddy, P. (2017). Perspective: Thermal and thermoelectric transport in molecular junctions. *The Journal of Chemical Physics*, 146(9), 092201.
14. Ismael, A. K., & Lambert, C. J. (2020). Molecular-scale thermoelectricity: a worst-case scenario. *Nanoscale Horizons*, 5(7), 1073-1080.
15. Milan, D. C., Krempe, M., Ismael, A. K., Movsisyan, L. D., Franz, M., Grace, I., ... & Nichols, R. J. (2017). The single-molecule electrical conductance of a rotaxane-hexayne supramolecular assembly. *Nanoscale*, 9(1), 355-361.
16. Gantenbein, M., Wang, L., Al-Jobory, A. A., Ismael, A. K., Lambert, C. J., Hong, W., & Bryce, M. R. (2017). Quantum interference and heteroaromaticity

- of para-and meta-linked bridged biphenyl units in single molecular conductance measurements. *Scientific reports*, 7(1), 1-9.
17. Carlotti, M., Kovalchuk, A., Wächter, T., Qiu, X., Zharnikov, M., & Chiechi, R. C. (2016). Conformation-driven quantum interference effects mediated by through-space conjugation in self-assembled monolayers. *Nature communications*, 7(1), 1-7.
  18. Naghibi, S., Ismael, A. K., Vezzoli, A., Al-Khaykane, M. K., Zheng, X., Grace, I. M., ... & Nichols, R. J. (2019). Synthetic Control of Quantum Interference by Regulating Charge on a Single Atom in Heteroaromatic Molecular Junctions. *The journal of physical chemistry letters*, 10(20), 6419-6424.
  19. Kronemeijer, A. J., Akkerman, H. B., Kudernac, T., van Wees, B. J., Feringa, B. L., Blom, P. W., & de Boer, B. (2008). Reversible conductance switching in molecular devices. *Advanced Materials*, 20(8), 1467-1473.
  20. Yzambart, G., Rincón-García, L., Al-Jobory, A. A., Ismael, A. K., Rubio-Bollinger, G., Lambert, C. J., ... & Bryce, M. R. (2018). Thermoelectric Properties of 2, 7-Dipyridylfluorene Derivatives in Single-Molecule Junctions. *The Journal of Physical Chemistry C*, 122(48), 27198-27204.
  21. Ismael, A. K., Grace, I., & Lambert, C. J. (2015). Increasing the thermopower of crown-ether-bridged anthraquinones. *Nanoscale*, 7(41), 17338-17342.
  22. Basch, H., Cohen, R., & Ratner, M. A. (2005). Interface geometry and molecular junction conductance: Geometric fluctuation and stochastic switching. *Nano letters*, 5(9), 1668-1675.
  23. Ulrich, J., Esrail, D., Pontius, W., Venkataraman, L., Millar, D., & Doerr, L. H. (2006). Variability of conductance in molecular junctions. *The Journal of Physical Chemistry B*, 110(6), 2462-2466.

24. Love, J. C., Estroff, L. A., Kriebel, J. K., Nuzzo, R. G., & Whitesides, G. M. (2005). Self-assembled monolayers of thiolates on metals as a form of nanotechnology. *Chemical reviews*, *105*(4), 1103-1170.
25. Sizov, A. S., Agina, E. V., & Ponomarenko, S. A. (2018). Self-assembled semiconducting monolayers in organic electronics. *Russian Chemical Reviews*, *87*(12), 1226.
26. Casalini, S., Bortolotti, C. A., Leonardi, F., & Biscarini, F. (2017). Self-assembled monolayers in organic electronics. *Chemical Society Reviews*, *46*(1), 40-71.
27. Williams, J. A., & Gorman, C. B. (2007). Alkanethiol reductive desorption from self-assembled monolayers on gold, platinum, and palladium substrates. *The Journal of Physical Chemistry C*, *111*(34), 12804-12810.
28. Frederiksen, T., Munuera, C., Ocal, C., Brandbyge, M., Paulsson, M., Sánchez-Portal, D., & Arnau, A. (2009). Exploring the tilt-angle dependence of electron tunneling across molecular junctions of self-assembled alkanethiols. *ACS nano*, *3*(8), 2073-2080.
29. Qi, Y., Ratera, I., Park, J. Y., Ashby, P. D., Quek, S. Y., Neaton, J. B., & Salmeron, M. (2008). Mechanical and charge transport properties of alkanethiol self-assembled monolayers on a Au (111) surface: The role of molecular tilt. *Langmuir*, *24*(5), 2219-2223.
30. Song, H., Lee, H., & Lee, T. (2007). Intermolecular chain-to-chain tunneling in metal– alkanethiol– metal junctions. *Journal of the American Chemical Society*, *129*(13), 3806-3807.

31. Akkerman, H. B., Blom, P. W., De Leeuw, D. M., & De Boer, B. (2006). Towards molecular electronics with large-area molecular junctions. *Nature*, *441*(7089), 69-72.
32. Wang, G., Kim, Y., Choe, M., Kim, T. W., & Lee, T. (2011). A new approach for molecular electronic junctions with a multilayer graphene electrode. *Advanced Materials*, *23*(6), 755-760.
33. Zhang, Y., Zhao, Z., Fracasso, D., & Chiechi, R. C. (2014). Bottom-up molecular tunneling junctions formed by self-assembly. *Israel Journal of Chemistry*, *54*(5-6), 513-533.
34. Ismael, A., Wang, X., Bennett, T. L., Wilkinson, L. A., Robinson, B. J., Long, N. J., ... & Lambert, C. J. (2020). Tuning the thermoelectrical properties of anthracene-based self-assembled monolayers. *Chemical science*, *11*(26), 6836-6841.
35. Ismael, A., Al-Jobory, A., Wang, X., Alshehab, A., Almutlg, A., Alshammari, M., ... & Lambert, C. (2020). Molecular-scale thermoelectricity: as simple as 'ABC'. *Nanoscale Advances*, *2*(11), 5329-5334.
36. Chiodini, S., Ruiz-Rincón, S., Garcia, P. D., Martin, S., Kettelhoit, K., Armenia, I., ... & Cea, P. (2020). Bottom Effect in Atomic Force Microscopy Nanomechanics. *Small*, *16*(35), 2000269.
37. DelRio, F. W., Jaye, C., Fischer, D. A., & Cook, R. F. (2009). Elastic and adhesive properties of alkanethiol self-assembled monolayers on gold. *Applied Physics Letters*, *94*(13), 131909.

38. Zhang, Y., Qiu, X., Gordiichuk, P., Soni, S., Krijger, T. L., Herrmann, A., & Chiechi, R. C. (2017). Mechanically and electrically robust self-assembled monolayers for large-area tunneling junctions. *The Journal of Physical Chemistry C*, *121*(27), 14920-14928.
39. Wei, Z., Hansen, T., Santella, M., Wang, X., Parker, C. R., Jiang, X., ... & Laursen, B. W. (2015). Molecular Heterojunctions of Oligo (phenylene ethynylene) s with Linear to Cruciform Framework. *Advanced Functional Materials*, *25*(11), 1700-1708.
40. Jia, C., Famili, M., Carlotti, M., Liu, Y., Wang, P., Grace, I. M., ... & Duan, X. (2018). Quantum interference mediated vertical molecular tunneling transistors. *Science advances*, *4*(10), eaat8237.
41. Weiss, E. A., Kaufman, G. K., Kriebel, J. K., Li, Z., Schalek, R., & Whitesides, G. M. (2007). Si/SiO<sub>2</sub>-templated formation of ultraflat metal surfaces on glass, polymer, and solder supports: Their use as substrates for self-assembled monolayers. *Langmuir*, *23*(19), 9686-9694.
42. Tran Khac, B. C., DelRio, F. W., & Chung, K. H. (2018). Interfacial strength and surface damage characteristics of atomically thin h-BN, MoS<sub>2</sub>, and graphene. *ACS applied materials & interfaces*, *10*(10), 9164-9177.
43. Rezek, B., Čermák, J., Kromka, A., Ledinský, M., Hubík, P., Mareš, J. J., ... & Kočka, J. (2011). Synthesis, structure, and opto-electronic properties of organic-based nanoscale heterojunctions. *Nanoscale research letters*, *6*(1), 1-12.

44. Szwajca, A., Wei, J., Schukfeh, M. I., & Tornow, M. (2015). Self-assembled monolayers of alkyl-thiols on InAs: A Kelvin probe force microscopy study. *Surface Science*, *633*, 53-59.
45. Wang, X., Bennett, T. L., Ismael, A., Wilkinson, L. A., Hamill, J., White, A. J., ... & Lambert, C. J. (2020). Scale-up of room-temperature constructive quantum interference from single molecules to self-assembled molecular-electronic films. *Journal of the American Chemical Society*, *142*(19), 8555-8560.
46. Wang, G., Kim, T. W., Jo, G., & Lee, T. (2009). Enhancement of field emission transport by molecular tilt configuration in metal– molecule– metal junctions. *Journal of the American Chemical Society*, *131*(16), 5980-5985.
47. Slowinski, K., Chamberlain, R. V., Miller, C. J., & Majda, M. (1997). Through-bond and chain-to-chain coupling. Two pathways in electron tunneling through liquid alkanethiol monolayers on mercury electrodes. *Journal of the American Chemical Society*, *119*(49), 11910-11919.
48. Johnson, K. L., Kendall, K., & Roberts, A. (1971). Surface energy and the contact of elastic solids. *Proceedings of the royal society of London. A. mathematical and physical sciences*, *324*(1558), 301-313.
49. Dokukin, M. E., & Sokolov, I. (2012). On the measurements of rigidity modulus of soft materials in nanoindentation experiments at small depth. *Macromolecules*, *45*(10), 4277-4288.
50. Burnham, N. A., Colton, R. J., & Pollock, H. M. (1992). Work-function anisotropies as an origin of long-range surface forces. *Physical review letters*, *69*(1), 144.

51. Gomar-Nadal, E., Ramachandran, G. K., Chen, F., Burgin, T., Rovira, C., Amabilino, D. B., & Lindsay, S. M. (2004). Self-assembled monolayers of tetrathiafulvalene derivatives on Au (111): Organization and electrical properties. *The Journal of Physical Chemistry B*, *108*(22), 7213-7218.
52. Lambert, C. J., & Liu, S. X. (2018). A magic ratio rule for beginners: a chemist's guide to quantum interference in molecules. *Chemistry—A European Journal*, *24*(17), 4193-4201.
53. Sangtarash, S., Huang, C., Sadeghi, H., Sorohhov, G., Hauser, J., Wandlowski, T., ... & Lambert, C. J. (2015). Searching the hearts of graphene-like molecules for simplicity, sensitivity, and logic. *Journal of the American Chemical Society*, *137*(35), 11425-11431.
54. Geng, Y., Sangtarash, S., Huang, C., Sadeghi, H., Fu, Y., Hong, W., ... & Liu, S. X. (2015). Magic ratios for connectivity-driven electrical conductance of graphene-like molecules. *Journal of the American Chemical Society*, *137*(13), 4469-4476.
55. Ferrer, J., Lambert, C. J., García-Suárez, V. M., Manrique, D. Z., Visontai, D., Oroszlany, L., ... & Algharagholy, L. A. (2014). GOLLUM: a next-generation simulation tool for electron, thermal and spin transport. *New Journal of Physics*, *16*(9), 093029.

## Chapter 5

### 5. ABC Theory of Molecular-Scale Thermoelectricity

#### 5.1 Introduction

The following work was carried out in collaboration with the group of Professor. Nicholas Long (Department of Chemistry, Imperial College London), who synthesised the anthracene molecules and Dr. Benjamin Robinson (Physics Department, Lancaster University), who conducted the experiments. In this chapter, I will present our joint experimental and theoretical work on the Molecular-scale thermoelectricity, and the results presented here were published in the following paper:

*“Molecular-scale thermoelectricity: as simple as ‘ABC’”*

*Ismael, A., Al-Jobory, A., Wang, X., Alshehab, A., Almutlg, A., Alshammari, M., Grace, I., Bennett, T.L., Wilkinson, L.A., Robinson, B.J. and Long, N.J., 2020. Nanoscale Advances, 2(11), pp.5329-5334.*

The Seebeck coefficient or thermopower  $S$  of a nanojunction or of a material is defined as  $S = -\Delta V/\Delta T$ , where  $\Delta V$  is the voltage difference between the two electrodes when a temperature difference  $\Delta T$  is established between them. My goal was to find a new strategy for predicting the Seebeck coefficient at the molecular scale from a simple measured  $I - V$  curve. This approach could save significant amount of efforts and costs.

In this chapter, I am going to describe this method in more detail. I will introduce the curve fitting procedure on an  $I - V$  characteristic and link that to the Taylor expansion [1]. From the parabola shape (the outcome of the fitting procedure), I determine the 3

constants  $a$ ,  $b$  and  $c$ , which form the ABC theory. I will mathematically prove that  $I(V, a, b, c) = I(V, a, -b, c)$ , which means the ABC theory predicts the magnitude of the coefficient  $b$ . Put differently, the ABC theory cannot predict the sign of the Seebeck coefficient, because it can only predict the magnitude of the coefficient  $b$ . I will also demonstrate the effect of the parameter  $c$  on the predicted Seebeck coefficient values. Finally, I will test the ABC theory results against the direct scanning tunnelling microscope (STM) measured Seebeck coefficient.

## 5.2 Motivation

If the Seebeck coefficient  $S$  of single molecules or self-assembled monolayers (SAMs) could be predicted from measurements of their conductance-voltage ( $G - V$ ) characteristics alone, then the experimentally more difficult task of creating a set-up to measure their thermoelectric properties could be avoided. This work highlights a novel strategy for predicting an upper bound to the Seebeck coefficient of single molecules or SAMs, from measurements of their  $G - V$  characteristics. The theory begins by making a fit to measured  $G - V$  curves using three fitting parameters, denoted  $a$ ,  $b$  and  $c$ . This ‘ABC’ theory then predicts a maximum value for the magnitude of the corresponding Seebeck coefficient. This is a useful material parameter, because if the predicted upper bound is large, then the material would warrant further investigation using a full Seebeck-measurement setup. On the other hand, if the upper bound is small, then the material would not be promising and this much more technically demanding set of measurements would be avoided. Histograms of predicted Seebeck coefficients are compared with histograms of measured Seebeck coefficients for six different SAMs

formed from anthracene-based molecules with different anchor groups. These histograms and are shown to be in excellent agreement.

### 5.3 Studied Molecules

In this chapter, 6 anthracene-based molecules were selected, the chemical structures of which are shown in Figure 5.1. These systems demonstrate both positive and negative Seebeck coefficients and were selected to compare their measured STM Seebeck values to those predicted by the ABC model. Note that Molecules **3** and **4** were studied in the previous chapter.

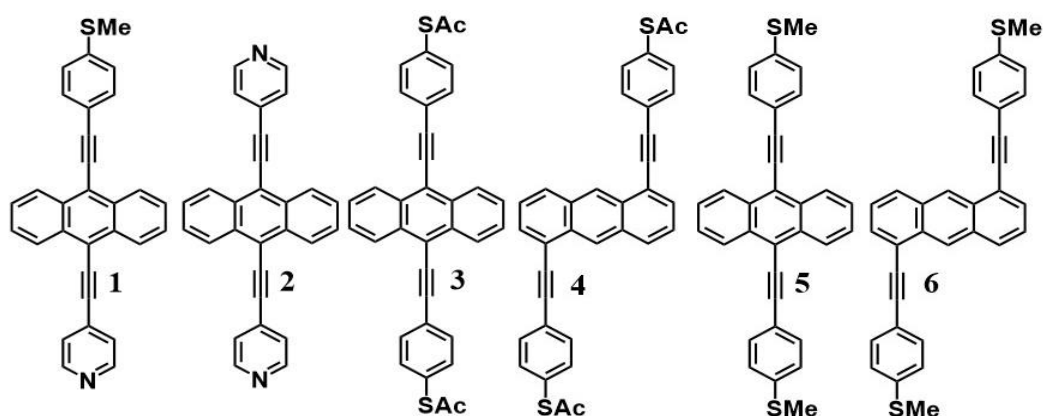


Figure 5.1: Structures of studied anthracene-based molecular wires. **1**, **2**, **3** and **5** correspond to the 7,2' connectivity, while **4** and **6** correspond to the 1,5' connectivity around the central anthracene core. These molecules also differ in the anchor groups through which they bind to a terminal electrode, with the binding groups denoted as follows; **1** = PySMe, **2** = 2Py, **3** and **4** = 2SAc, **5** and **6** = 2SMe.

From Figure 5.1 one can see that there are two connectivities: molecules **1**, **2**, **3** and **5** correspond to the 7,2' connectivity, whereas molecules **4** and **6** correspond to the 1,5'

connectivity around the central anthracene core. These 6 molecules also differ in the anchor groups through which they bind to a terminal electrode, with the binding groups denoted as follows; **1** = PySMe, **2** = 2Py, **3** and **4** = 2SAc, **5** and **6** = 2SMe.

#### 5.4 ABC Theory

My starting point is the Landauer-Buttiker theory of phase-coherent transport, which utilises the transmission coefficient,  $T(E)$  describing the propagation of electrons of energy  $E$  from one electrode to the other via a single molecule or a SAM. A large body [35, 36] of experimental evidence suggests that when a molecule is placed between two metallic electrodes, the highest occupied molecular orbital (HOMO) and lowest unoccupied molecular orbital (LUMO) adjust themselves, such that the Fermi energy  $E_F$  of the electrodes lies within the HOMO-LUMO gap of the molecule. Furthermore, DFT simulations often reveal that the logarithm of the transmission function is a smooth function of energy near  $E_F$  and therefore it is reasonable to approximate  $T(E)$  by a Taylor expansion of the form

$$\ln T(E) = a + b(E - E_F) + c(E - E_F)^2 \quad (5.1)$$

In what follows, the coefficients  $a, b, c$  of this ‘ABC’ theory will be determined by fitting the above expression to measured low-voltage conductance-voltage curves, under the assumption that  $a, b$  and  $c$  do not change with voltage. Information about  $T(E)$  has been extracted from experimental measurements previously.[37, 38] ABC theory is aimed at describing off-resonance transport, since this is the most common case in molecular junctions and self-assembled monolayers. Of course, by applying an electrostatic or electrochemical gate, one could move transport towards resonance, but

this is not relevant from the point of view of identifying thermoelectric materials. Our approach also applies to non-symmetric junctions, as demonstrated by molecule **1**, and is not limited to the wide band approximation. In fact, equation (5.1) can describe many molecular junctions, but it could fail at high bias, because the proposed  $I - V$  fitting assumes that  $I - V$  curves are symmetric and therefore it should not be applied to junctions exhibiting strong rectification. However, it should be noted that the Seebeck effect is a low bias phenomenon, because typical values of the Seebeck coefficient are in the range of microvolts per Kelvin.

To acquire this fitting, we measure the current versus voltage at  $M$  different locations (labelled  $j$ ) across a SAM. At each location, the current  $I_{exp}^j(V_i)$  is measured at a series of  $N$  voltages labelled  $V_i$  between  $-1$  V and  $+1$  V, where  $N$  is typically several hundred. The corresponding conductance is defined to be  $G_{exp}^j(V_i) = I_{exp}^j(V_i)/V_i$ . For each location  $j$ , we then computed the mean square deviations

$$\chi_j^2(a, b, c) = \frac{1}{N} \sum_{i=1}^N [G(V_i, a, b, c) - G_{exp}^j(V_i)]^2 \quad (5.2)$$

In this expression,  $G(V_i, a, b, c) = I(V_i, a, b, c)/V_i$  where  $I(V_i, a, b, c)$  is the theoretical current obtained from the Landauer formula:

$$I(V, a, b, c) = \left(\frac{2e}{h}\right) \int_{-\infty}^{\infty} T(E, a, b, c) dE [f_{left}(E) - f_{right}(E)] \quad (5.3)$$

where  $f_{left}(E)$  and  $f_{right}(E)$  are the Fermi distributions of the left and right leads, with Fermi energies  $E_F \pm \frac{eV}{2}$  respectively,  $e$  is the electronic charge,  $h$  is Planck's constant and  $T(E)$  is the transmission coefficient of equation (5.1). The parameters

$a, b, c$  were then varied to locate the minimum of  $\chi_j^2(a, b, c)$ . The resulting values of  $a, b, c$  are denoted  $a_j, b_j, c_j$ . From these fitted values, we obtained the predicted Seebeck coefficient for location  $j$  from the formula [30]

$$S_j = -\frac{L_1(a_j, b_j, c_j)}{|e|TL_0(a_j, b_j, c_j)} \quad (5.4)$$

where

$$L_n(a_j, b_j, c_j) = \int_{-\infty}^{\infty} dE (E - E_F)^n T_{el}(E) \left( -\frac{\partial f(E, T)}{\partial E} \right) \quad (5.5)$$

and  $f(E) = 1/[\exp(E - E_F)/k_B T + 1]$  is the Fermi distribution.

To demonstrate the validity of this ‘ABC’ theory, we then formed a histogram of these predicted values and compared these with histograms of experimentally measured Seebeck coefficients. In fact, we found that in all cases,  $c$  was small and in many cases setting  $c = 0$  yielded an acceptable fit.

It should be noted that ABC theory cannot predict the sign of the Seebeck coefficient, because it can only predict the magnitude of the coefficient  $b$  (see section 5.8). To illustrate this point, note that at low-enough temperatures, the current  $I$  due to a source-drain bias voltage  $V$ , and the Seebeck coefficient  $S$  are given by

$$I = \frac{2e}{h} \int_{E_F - \frac{eV}{2}}^{E_F + \frac{eV}{2}} T(E) dE \quad (5.6)$$

$$S \approx -\alpha |e| T \left( \frac{d \ln T(E)}{dE} \right)_{E=E_F} \quad (5.7)$$

where  $\alpha$  is the Lorentz number  $\alpha = \left(\frac{k_B}{e}\right)^2 \frac{\pi^2}{3} = 2.44 \times 10^{-8} W\Omega K^{-2}$ ,  $e$  is the electronic charge and  $T$  is the temperature.

This yields for the low-bias electrical conductance  $G$ ,

$$G = G_0 e^a \quad (5.8)$$

Assuming that an adequate fit can be obtained with  $c = 0$ , integration of equation (5.6) yields

$$G = \frac{I}{V} = G_0 e^a \frac{\sinh y}{y}, \quad \text{where } y = \frac{beV}{2} \quad (5.9)$$

which reduces to equation (5.8) in the limit  $V \rightarrow 0$ . Alternatively, if  $c$  is non-zero, by differentiating equation (5.6) one could fit to the differential conductance

$$\frac{1}{G_0} \frac{dI}{dV} = e^{[a+c\frac{V^2}{4}]} \cosh\left(b\frac{V}{2}\right) \quad (5.10)$$

In section 5.4, it is demonstrated that the current  $I(V, a, b, c)$  in equation (5.3) is an even function of  $b$ . This is also evident in the low-temperature equations (5.9) and (5.10), since  $\frac{\sinh y}{y}$  and  $\cosh y$  are even functions of  $y$ . Therefore, a fit to these formulae cannot determine the sign of  $b$ , because in equation (5.2),  $\chi_j^2(a, b, c) = \chi_j^2(a, -b, c)$ . In other words, if a minimum of  $\chi_j^2(a, b, c)$  is found for a particular value of  $b$ , then there will also be a minimum at  $-b$ .

From equations (5.7) and (5.1), this fitting yields the modulus of the Seebeck coefficient via the relation

$$|S| = -\alpha|e||b|T \quad (5.11)$$

If  $S$  is a random variable, then the average of  $|S|$  is greater than or equal to the average of  $S$ . Therefore, from the average of  $|S|$ , ABC theory yields an upper bound for the average Seebeck coefficient.

Equations (5.6) to (5.10) are valid at low temperatures only. At finite temperatures, the exact formula (5.3) is used to perform the fitting. In what follows, by simultaneously measuring both current-voltage relations and Seebeck coefficients, we demonstrate that ‘ABC’ theory indeed predicts an upper bound for the Seebeck coefficient from  $I - V$  curves.

### 5.5 Proof that $I(V, a, b, c) = I(V, a, -b, c)$

In this section, I am going to demonstrate a mathematical proof to show that

$$I(V, a, b, c) = I(V, a, -b, c).$$

From equations (5.1) and (5.3) above.

$$I(V, a, b, c) = \left(\frac{2e}{h}\right) \int_{-\infty}^{\infty} dx e^{(a+bx+cx^2)} \left[ \frac{1}{e^{\frac{x-v}{k_B T}} + 1} - \frac{1}{e^{\frac{x+v}{k_B T}} + 1} \right] \quad (5.12)$$

where  $x = E - E_F$  and  $v = eV/2$ . ie

$$I(V, a, b, c) = \left(\frac{2e}{h}\right) \int_{-\infty}^{\infty} dx e^{(a+bx+cx^2)} \left[ \frac{e^{\frac{x+v}{k_B T}} - e^{\frac{x-v}{k_B T}}}{\left[ e^{\frac{x-v}{k_B T}} + 1 \right] \left[ e^{\frac{x+v}{k_B T}} + 1 \right]} \right] \quad (5.13)$$

After making the substitution  $y = -x$  and replacing  $b$  by  $-b$ , equation (5.12)

becomes

$$I(V, a, -b, c) = \left(\frac{2e}{h}\right) \int_{+\infty}^{-\infty} (-dy) e^{(a+by+cy^2)} \left[ \frac{1}{e^{\frac{-y-v}{k_B T}} + 1} - \frac{1}{e^{\frac{-y+v}{k_B T}} + 1} \right]$$

*i.e.*

$$I(V, a, -b, c) = \left(\frac{2e}{h}\right) \int_{-\infty}^{+\infty} dy e^{(a+by+cy^2)} \left[ \frac{e^{\frac{y+v}{k_B T}}}{e^{\frac{y+v}{k_B T}} + 1} - \frac{e^{\frac{y-v}{k_B T}}}{e^{\frac{y-v}{k_B T}} + 1} \right]$$

*i.e.*

$$I(V, a, -b, c) = \int_{-\infty}^{+\infty} dy e^{(a+by+cy^2)} \left[ \frac{e^{\frac{y+v}{k_B T}} - e^{\frac{y-v}{k_B T}}}{[e^{\frac{y+v}{k_B T}} + 1][e^{\frac{y-v}{k_B T}} + 1]} \right] \quad (5.14)$$

Since equations (5.13) and (5.14) are identical, this completes the proof and demonstrates that only  $|b|$  can be predicted by ABC theory.

## 5.6 Curve Fitting

In this study, our experimental collaborators gathered several hundred  $I - V$  curves for each molecule utilising an STM device, and then applied the fitting procedure to calculate the modulus of the corresponding Seebeck coefficients. Figure 5.2 shows an example of a single  $I - V$  curve.

It can be performed data fitting interactively using the MATLAB Basic Fitting tool, or programmatically using MATLAB functions for fitting. Here in this chapter the function that has been used is  $\chi^2$  fit.

The first step in the curve fitting procedure is to divide the current  $I$  by the voltage  $V$  to obtain the ratio  $I/V$  which gives the finite-voltage conductance  $G$ . When obtaining  $I/V$  a spike occurs at  $V = 0$  as the ratio tends to infinity, as shown in Figure 5.3. After eliminating the spike close to zero voltage (red-dashed rectangle), the resulting  $G - V$  curve is smooth, as shown in Figure 5.4. The next step is to make a fit to this data, using

the ABC theory described in detail in section 5.4. Figure 5.5 shows an example of a comparison between experimental data and the fitted curve from ABC theory. This process is applied to each individual  $I - V$  curve of the 6 molecules in this study.

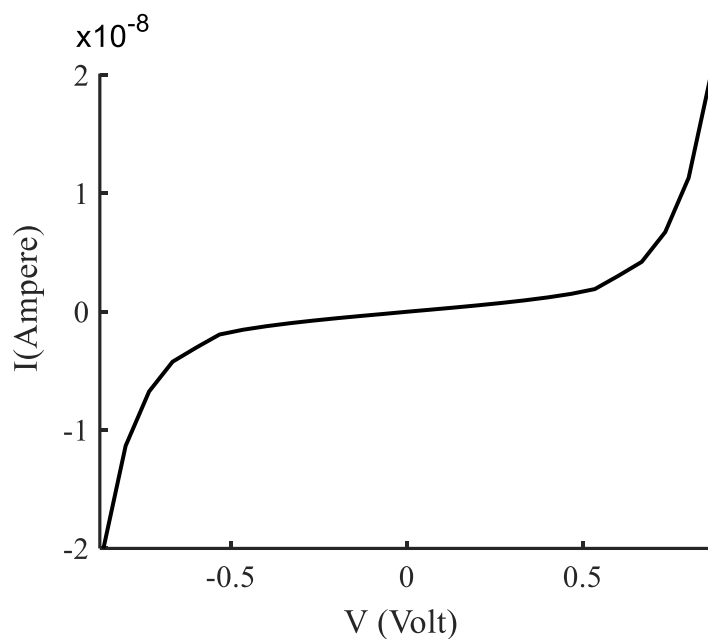


Figure 5.2: Example of an experimental  $I - V$  curve.

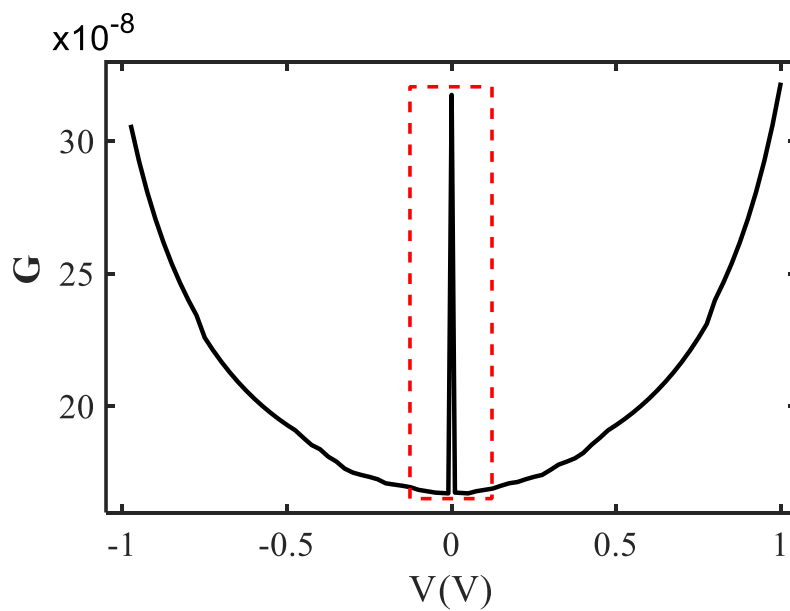


Figure 5.3: Example  $G - V$  curve; the spike occurs due to dividing by zero.

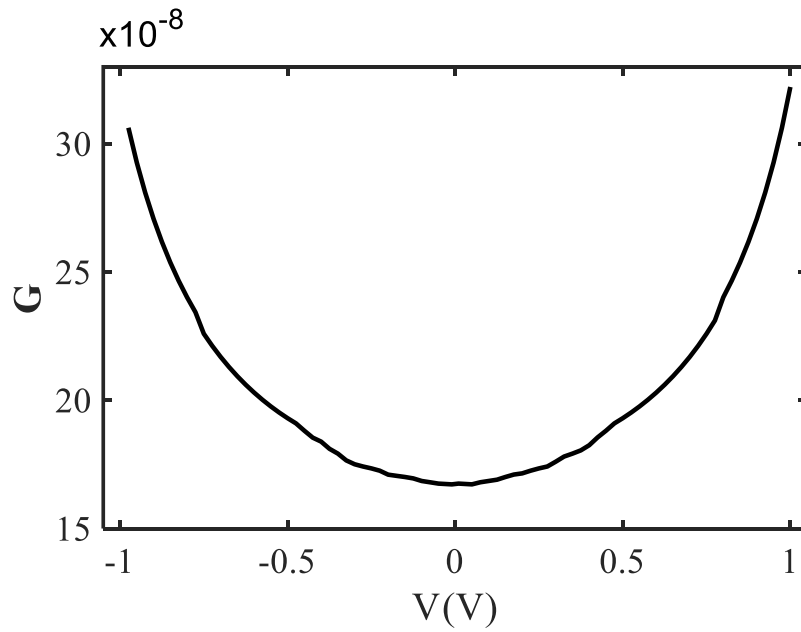


Figure 5.4: Example of a smooth  $G - V$  curve after deleting the spike close to zero volts.

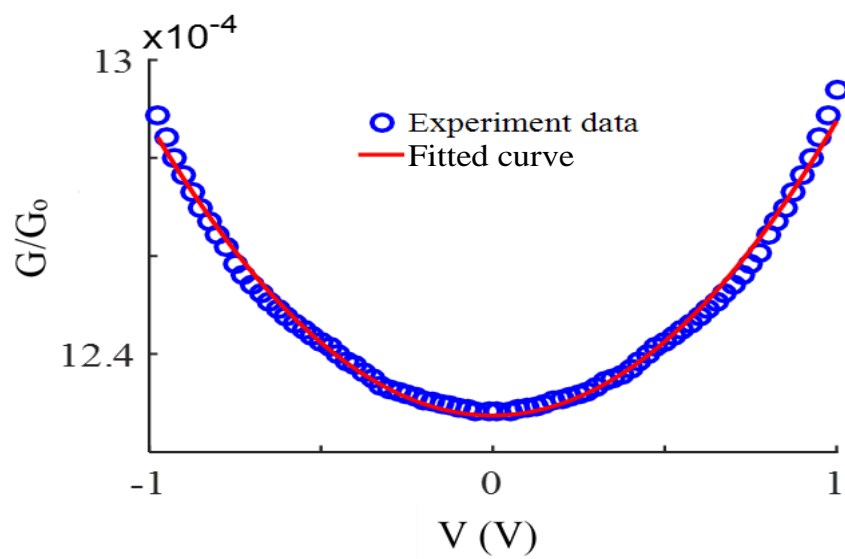


Figure 5.5: Example of a comparison between experimental values of  $G/G_0$  versus voltage  $V$  (blue-circles) and the fitted curve from ABC theory (red-solid line).

## 5.7 Experimental Data (*I – V* Characterisation)

Molecular conductance was characterized by conductive AFM (cAFM). Single molecule equivalence values were calculated by dividing the total conductance by the number of molecules in the junction. The number of molecules contacted by the probe was estimated by taking contact area between the sample and probe and dividing by the occupation area of a single molecule derived from Quartz Crystal Microbalance (QCM). The contact area between sample and probe was estimated by the Hertzian model:

$$r = (F \times R \times \frac{1}{Y})^{\frac{1}{3}}$$

$$\frac{1}{Y} = \frac{3}{4} \times \left( \frac{1 - \nu_1^2}{E_1} + \frac{1 - \nu_2^2}{E_2} \right)$$

where  $r$  is the contact radius,  $F$  the loading force from probe to sample,  $R$  the radius of the probe ( $\sim 18$  nm from the supplier),  $\nu_1$  and  $\nu_2$  the Poisson ratio of the material,  $E_1$  and  $E_2$  the Young's Modulus for probe ( $\sim 100$  GPa) and SAMs ( $\sim 10$  GPa).

The electrical transport properties of the SAMs were characterized using a custom cAFM system. The cAFM setup is based on a multi-mode8 AFM system (Bruker nanoscience). The bottom gold substrate was used as the source, and a *Pt/Cr* coated probe (Spark 70Pt, Nunano Ltd) was used as the drain. The force between probe and molecule was controlled at 2 nN, as this force is strong enough for the probe to penetrate through the water layer on the sample surface but not too strong so as to destroy the molecular thin film. The driven bias was added between the source and drain by a voltage generator (Aglient 33500B), the source to drain current was amplified by a current pre-amplifier (SR570, Stanford Research Systems), and the characteristics of the sample was collected by the computer.

In this study, nearly a thousand  $I - V$  characteristic curves were collected for each molecule, examples of which are shown in Figures 5.6-5.11.

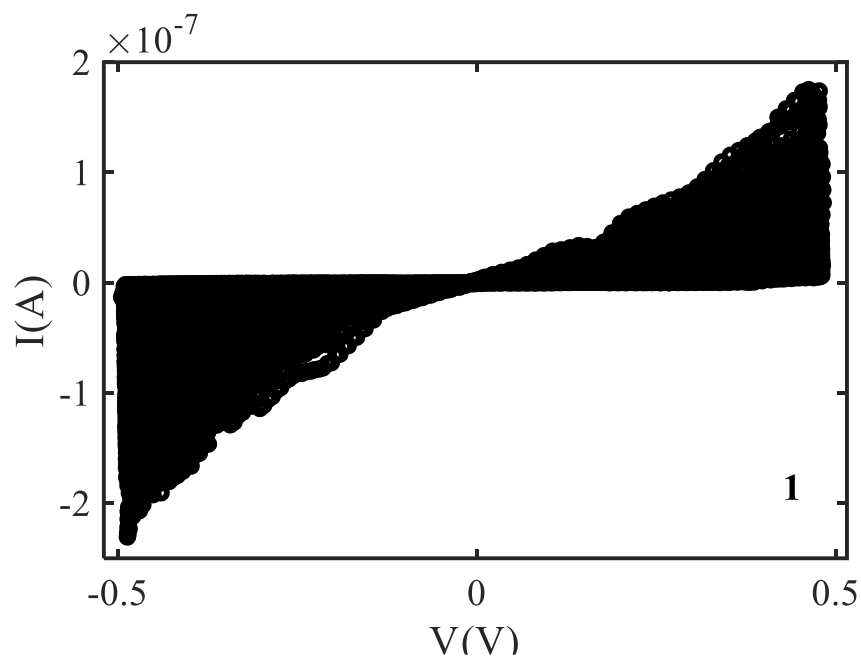


Figure 5.6:  $I - V$  curves obtained from STM device of molecule 1.

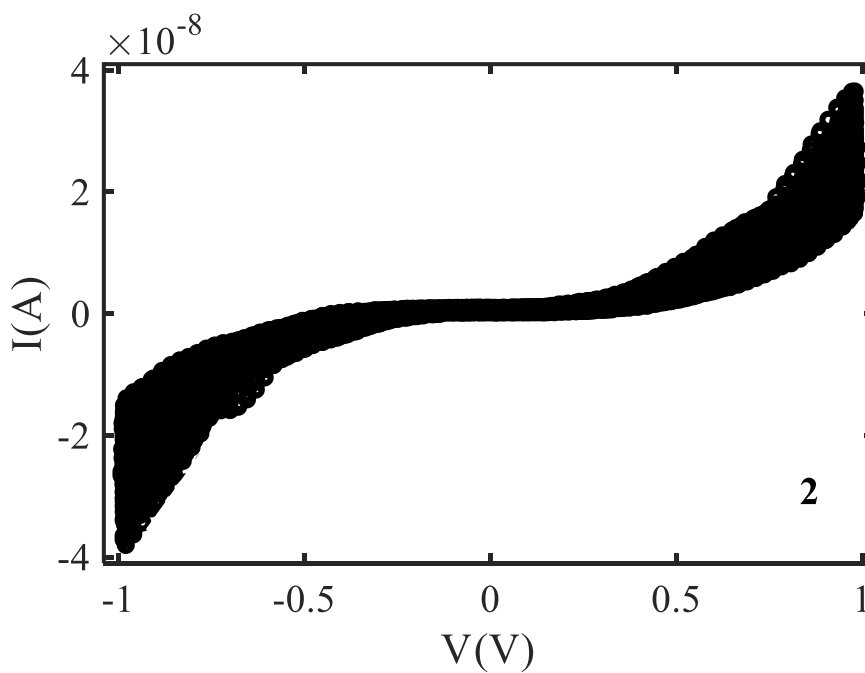


Figure 5.7:  $I - V$  curves obtained from STM device of molecule 2.

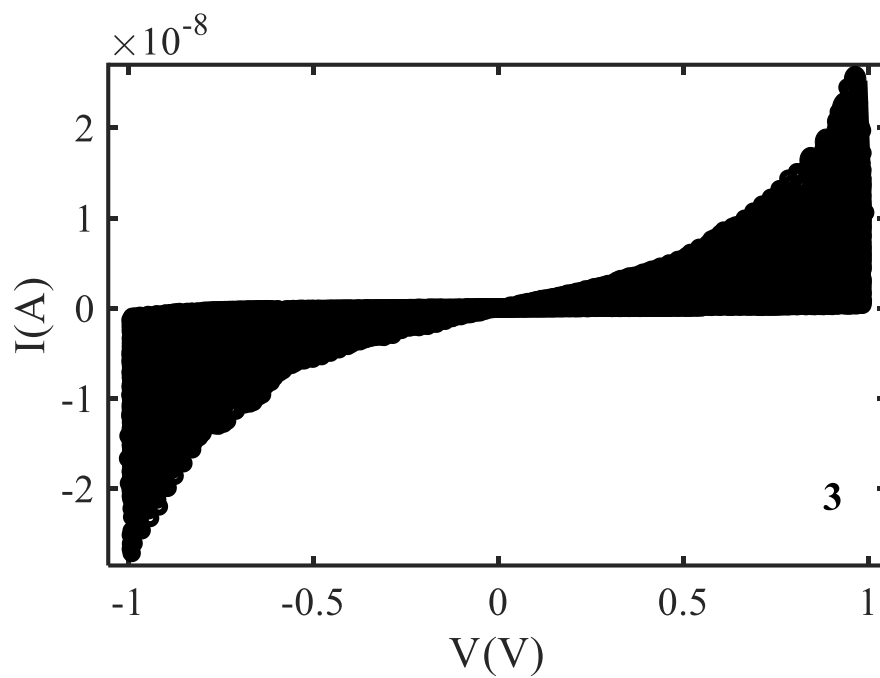


Figure 5.8:  $I - V$  characterisation experimental curves obtain from STM device of molecule 3.

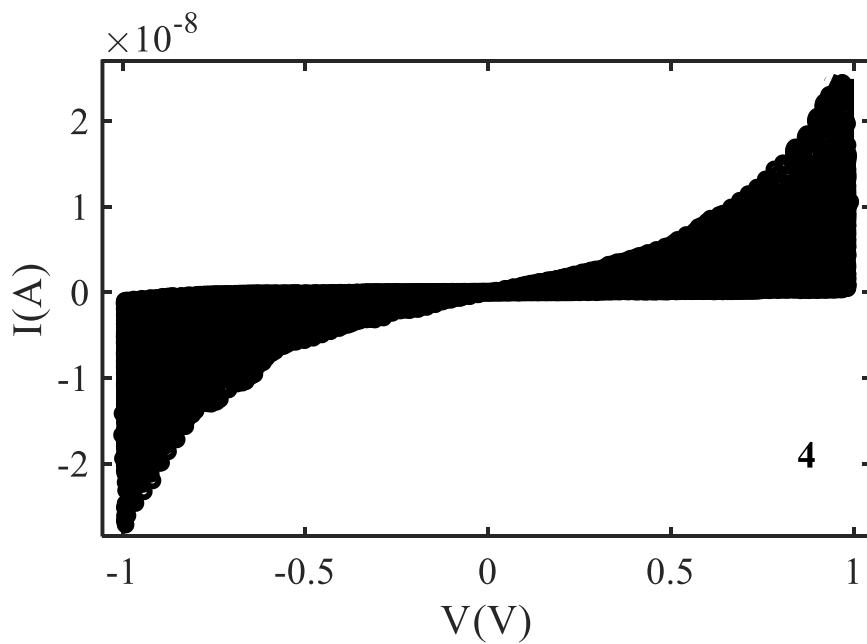


Figure 5.9:  $I - V$  characterisation experimental curves obtain from STM device of molecule 4.

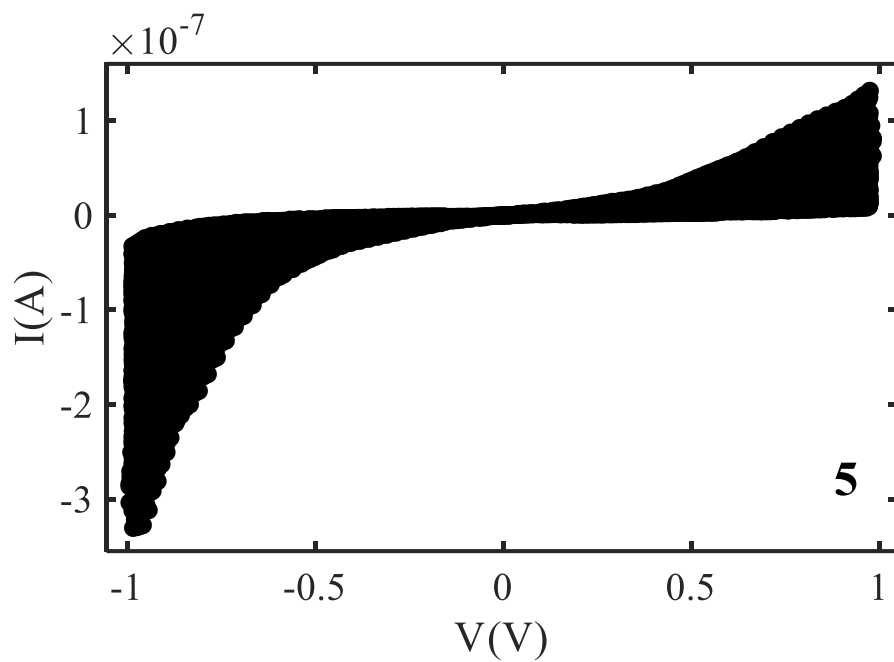


Figure 5.10:  $I - V$  characterisation experimental curves obtain from STM device of molecule 5.

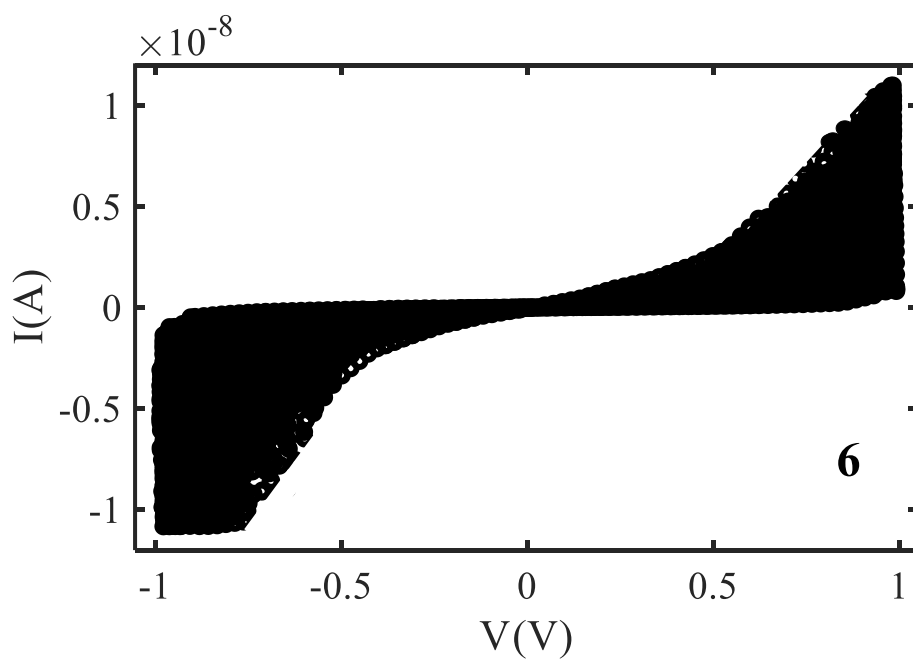


Figure 5.11:  $I - V$  characterisation experimental curves obtain from STM device of molecule 6.

## 5.8 Applying the Curve fitting procedure

After demonstrating the curve fitting procedure in section 5.6. Here, I present an example of fitting to an  $I - V$  characteristics curve for each molecule. This fitting was achieved using the MATLAB routine 'FIT' to find the minimum of  $\chi_j^2(a, b, c)$ , defined in equation (5.2).

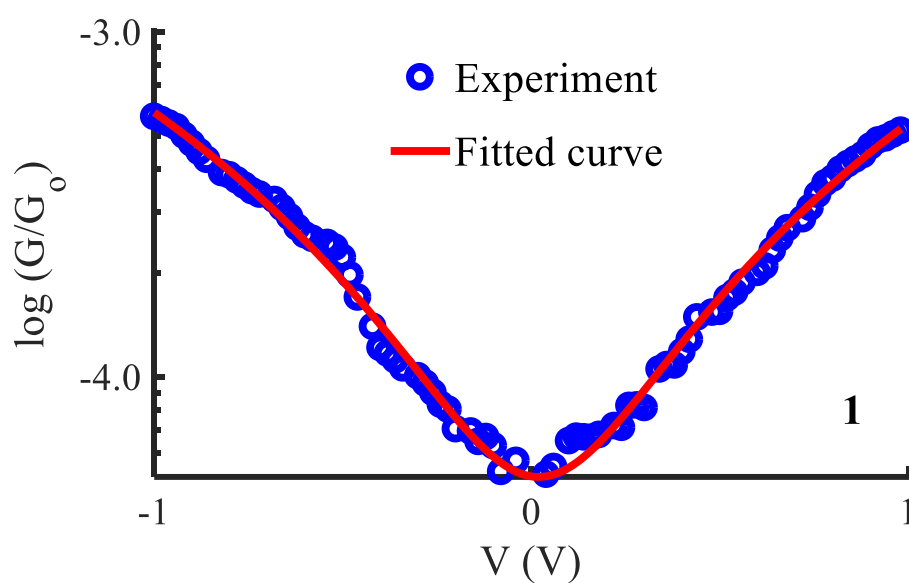


Figure 5.12: A comparison between experimental values of  $\log(G/G_0)$  versus voltage  $V$  (blue-circles) obtained from STM and the fitted curve from ABC theory (red-solid line) for molecule **1**.

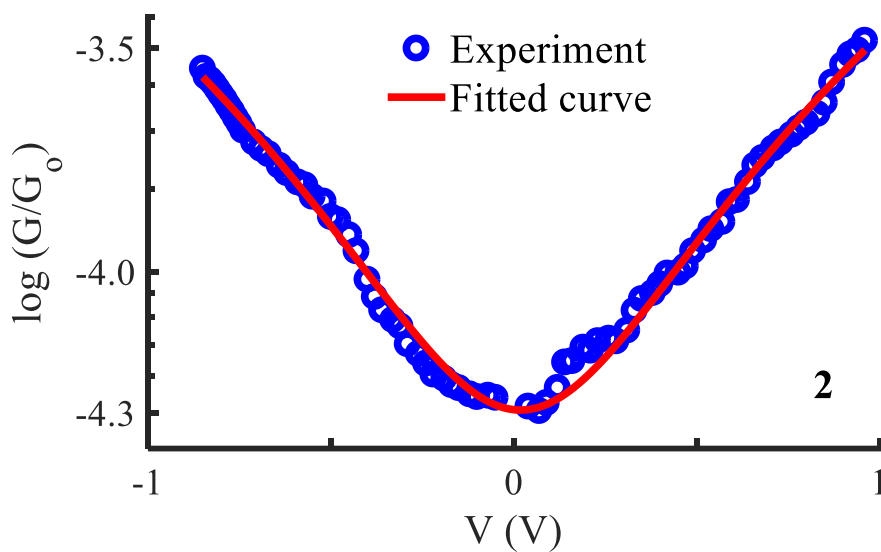


Figure 5.13: A comparison between experimental values of  $\log(G/G_0)$  versus voltage  $V$  (blue-circles) and the fitted curve from ABC theory (red-solid line) for molecule **2**.

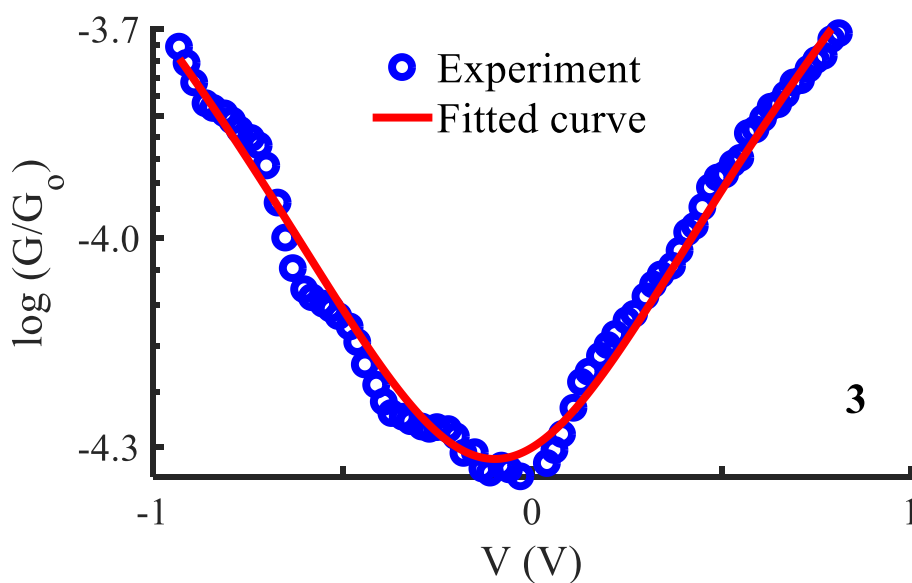


Figure 5.14: A comparison between experimental values of  $\log(G/G_0)$  versus voltage  $V$  (blue-circles) and the fitted curve from ABC theory (red-solid line) for molecule **3**.

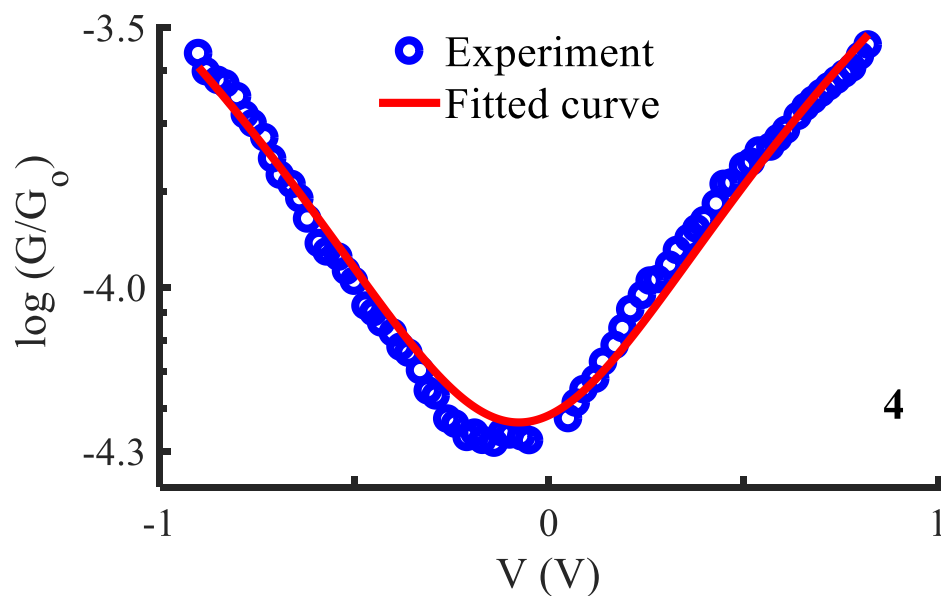


Figure 5.15: A comparison between experimental values of  $\log(G/G_0)$  versus voltage  $V$  (blue-circles) and the fitted curve from ABC theory (red-solid line) for molecule 4.

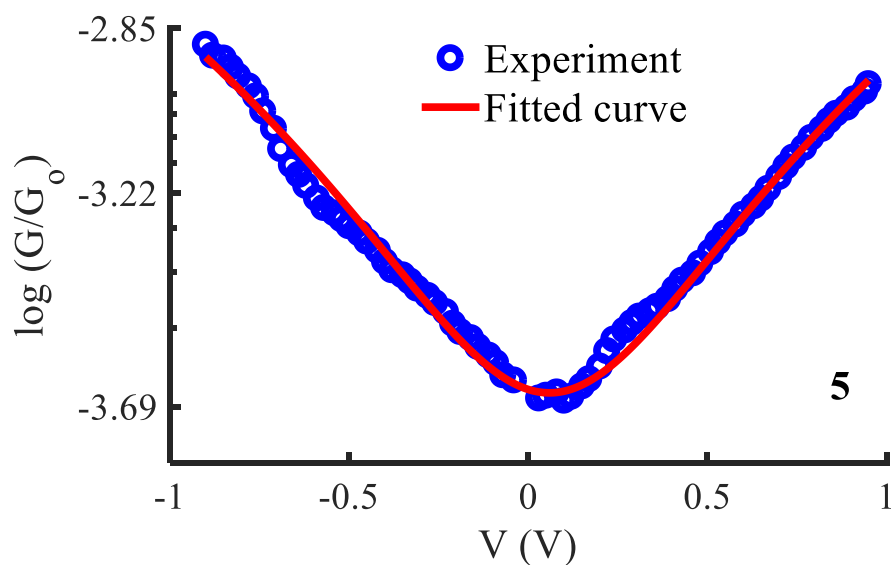


Figure 5.16: A comparison between experimental values of  $\log(G/G_0)$  versus voltage  $V$  (blue-circles) and the fitted curve from ABC theory (red-solid line) for molecule 5.

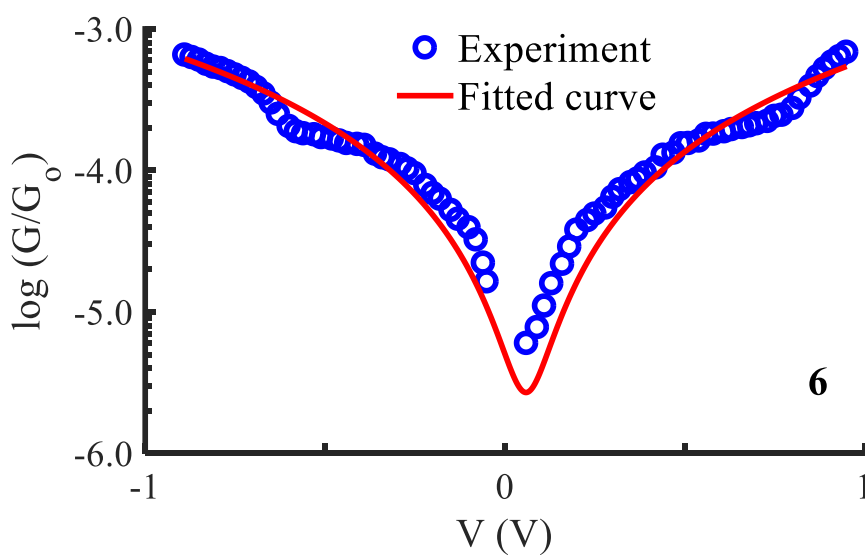


Figure 5.17: A comparison between experimental values of  $\log(G/G_0)$  versus voltage  $V$  (blue-circles) and the fitted curve from ABC theory (red-solid line) for molecule **6**.

### 5.9 Histograms of Seebeck coefficients

Experimental measurements provide histograms for molecules **1-6** (green histograms of Figures 5.18-5.23). By applying the fitting process on each  $G - V$  curve and using equation (5.4), we obtain the Seebeck coefficient values. From that data, a histogram has been generated for each molecule (red histograms of Figures 5.18-5.23), from the  $I - V$  experiment data (see Figures 5.11-5.16). It is worth mentioning that the ‘ABC’ model predicts the absolute value of the Seebeck histogram  $|S|$  (see section 5.7), whereas experimentally-measured Seebeck histograms can be positive or negative as shown in the green histograms of Figures 5.18-5.23. To compare theory predicted Seebeck histograms against experimentally-measured Seebeck histograms the absolute value has been taken for the experimental results (yellow histograms). Figures 5.18-

5.23 show a comparison between the experiment and theory predicted histograms of  $|S|$  (yellow and red histograms).

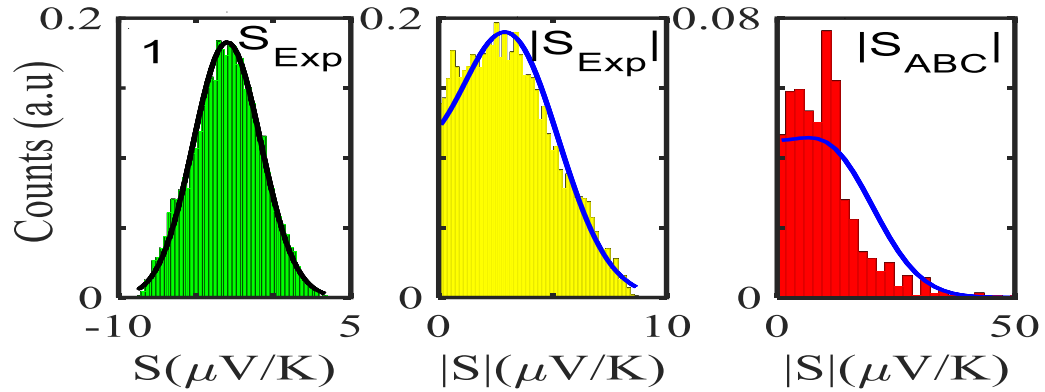


Figure 5.18: Experimentally derived and predicted ABC theory histograms along with their Gaussian and folded fit curves (black- and blue-solid lines) for **1** (green experiment, yellow absolute experiment and red absolute theory).

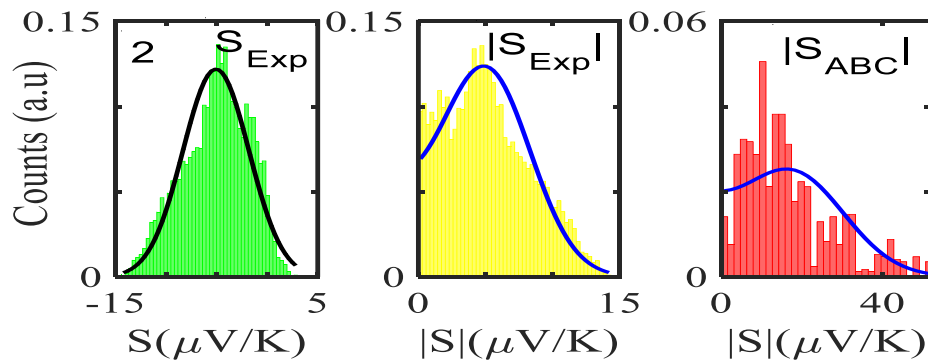


Figure 5.19: Experimentally derived and predicted ABC theory histograms along with their Gaussian and folded fit curves (black- and blue-solid lines) for **2** (green experiment, yellow absolute experiment and red absolute theory).

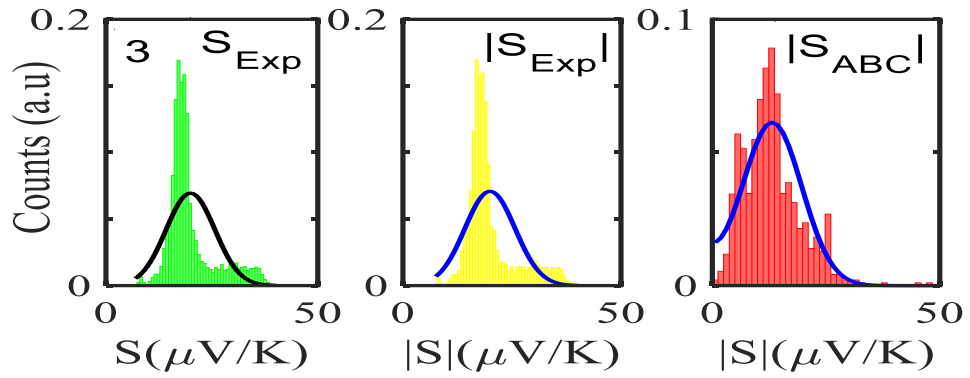


Figure 5.20: Experimentally derived and predicted ABC theory histograms along with their Gaussian and folded fit curves (black- and blue-solid lines) for **3** (green experiment, yellow absolute experiment and red absolute theory).

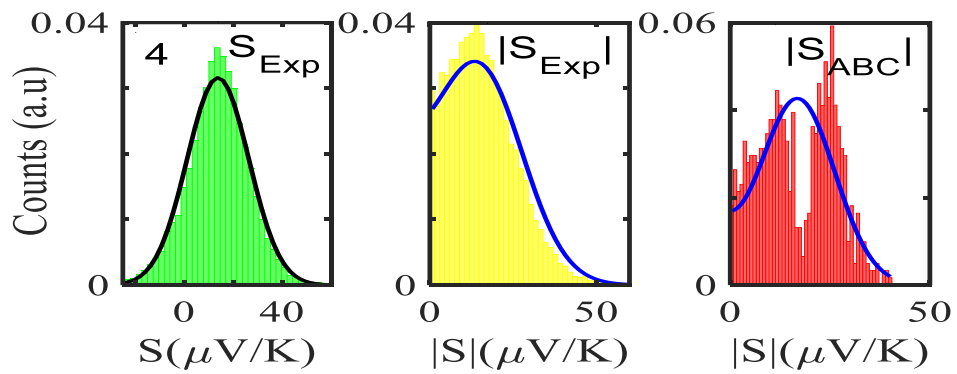


Figure 5.21: Experimentally derived and predicted ABC theory histograms along with their Gaussian and folded fit curves (black- and blue-solid lines) for **4** (green experiment, yellow absolute experiment and red absolute theory).

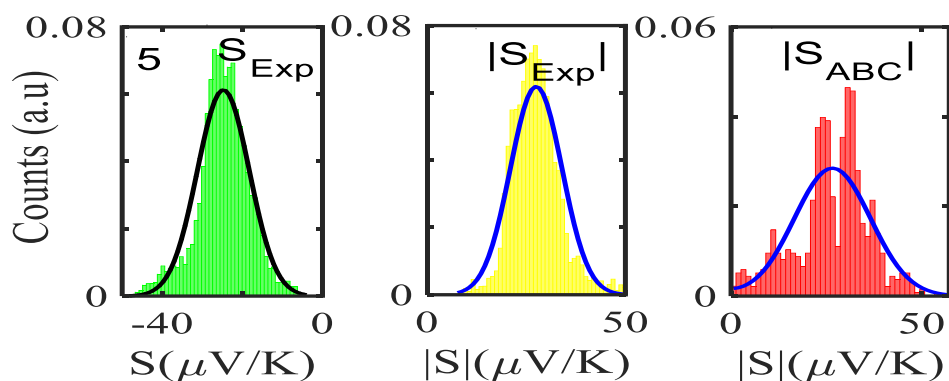


Figure 5.22: Experimentally derived and predicted ABC theory histograms along with their Gaussian and folded fit curves (black- and blue-solid lines) for **5** (green experiment, yellow absolute experiment and red absolute theory).

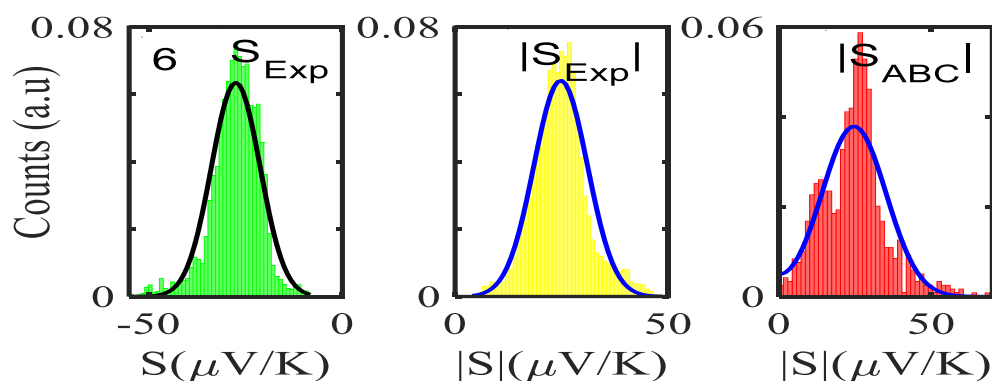


Figure 5.23: Experimentally derived and predicted ABC theory histograms along with their Gaussian and folded fit curves (black- and blue-solid lines) for **6** (green experiment, yellow absolute experiment and red absolute theory).

Figures 5.18-5.23 show that the experimental and predicted histograms are in qualitative agreement. To make a quantitative comparison, I first computed the average  $|S|$  (denoted  $|S_{ABC}|$ ) from the red histograms and compared this with the average  $|S|$  (denoted  $|S_{Exp}|$ ) from the yellow histograms. These values are shown in Figure 5.25, for each of the **6** molecules. This plot demonstrates strong overlap between

experimental and ABC-theory values, clearly demonstrating the predictive ability of ABC theory. My aim is to compare theory with experiment and since the experimental histograms are fitted to a single Gaussian, I follow the same approach for the theoretical histograms. There are two peaks in the theoretical histograms of Figures 5.21 and 5.22. For molecule **5** these occur at  $|S| = 32.7$  and  $|S| = 41.8$ . Taking the average of these yields  $|S| = 37.2$  which is very close to our quoted value for the most-probable  $|S|$  (ie  $|S| = 37.3$ ). Similarly, for molecule **4** these occur at  $|S| = 11.4$  and  $|S| = 24.3$  taking the average of these yields  $|S| = 17.8$ , which is close to our quoted value ( $|S| = 17.5$ ). Therefore, fitting to a single Gaussian provides an adequate prediction for  $|S|$  for the studied molecules.

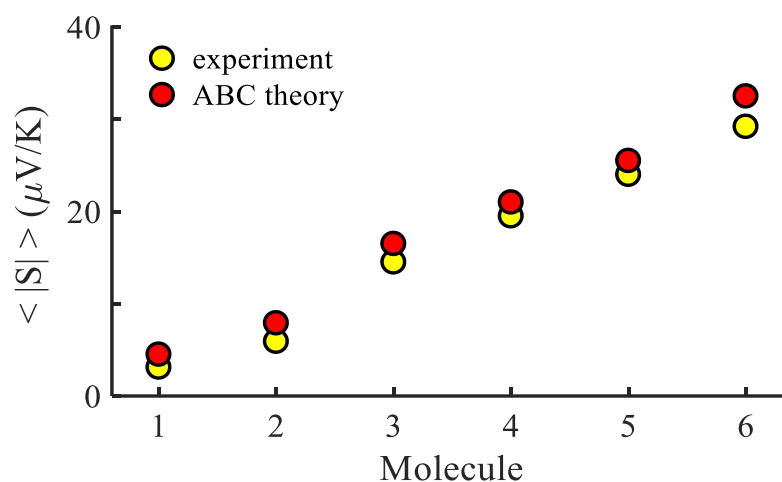


Figure 5.24 Experimental and ABC-theory predictions for average of the magnitudes of Seebeck coefficients  $\langle |S| \rangle$  (yellow- and red-circles respectively).

The averages in Figure 5.24 were obtained by making a Gaussian fit to the experimentally-measured (green) histograms, as is common practice in the literature. If each of the green histograms of measured values of  $S$  is assumed to approximate a Gaussian distribution of the form

$$p(S) = \frac{e^{-(S-S_0)^2/2\sigma^2}}{\sqrt{2\pi\sigma^2}} \quad (5.15)$$

where  $S_0$  is the average of  $S$ , and  $\sigma$  is the standard deviation, then  $\langle S \rangle = \int_{-\infty}^{\infty} dS S p(S) = S_0$  and  $\langle (S - S_0)^2 \rangle = \int_{-\infty}^{\infty} dS (S - S_0)^2 p(S) = \sigma^2$ .

This means that measured values of  $|S|$  possess a folded Gaussian distribution of the form  $f(|S|) = p(|S|) + p(-|S|)$ . *i.e.*

$$f(|S|) = \frac{e^{-(|S|-S_0)^2/2\sigma^2} + e^{-(|S|+S_0)^2/2\sigma^2}}{\sqrt{2\pi\sigma^2}} \quad (5.16)$$

or equivalently

$$f(|S|) = \frac{e^{-(|S|-S_0)^2/2\sigma^2} [2 \cosh\left(\frac{SS_0}{\sigma^2}\right)]}{\sqrt{2\pi\sigma^2}} \quad (5.17)$$

For  $|S_0| < \sigma$ ,  $f(|S|)$  has a maximum at  $|S| = 0$ , whereas for  $|S_0| > \sigma$ , the maximum occurs at  $|S| \neq 0$ . The blue curves in Figures 5.18 – 5.23 show a fit of this function to each of the red histograms. The black curves show plots of the corresponding Gaussian distributions. For the experimental averages corresponding to the yellow points in Figure 5.25 and for the ABC-predicted averages corresponding to the red points in figure 5.25, the average was computed by fitting a folded Gaussian  $f(|S|)$  to the histogram of predicted values of  $|S|$  and then using the formula

$$\langle |S| \rangle = \int_0^{\infty} dS |S| f(|S|)$$

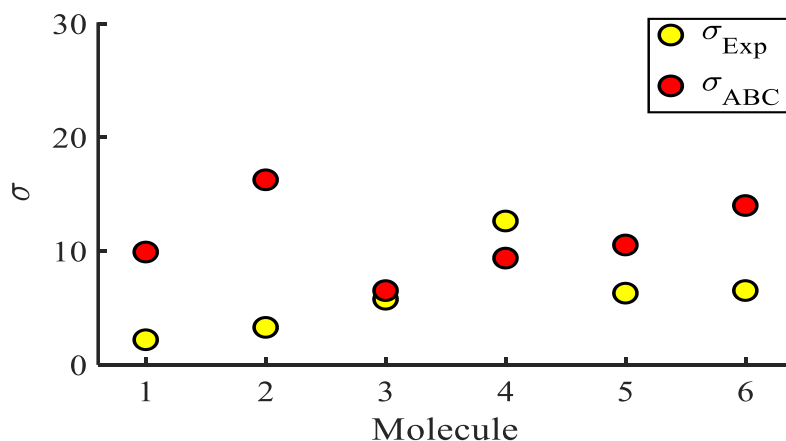


Figure 5.25. Standard deviations  $\sigma$  obtained from experiment and predicted ABC theory data (yellow- and red-circles).

Figure 5.25 shows a comparison between the resulting  $\sigma$  values for each of the molecules, obtained by fitting equation (5.16) to the red histograms and by fitting equation (5.15) to the green histograms. This shows that qualitative information about the widths of the distributions can also be obtained from ABC theory. Figure 5.25 shows similar results for the ABC standard deviations  $\sigma_{ABC}$  and the experimental  $\sigma_{Exp}$  for most molecules, whereas there is a larger difference for molecules **1** and **2**. To address this point, I shall calculate the mean square deviation  $\chi$  and compare it to the standard deviation  $\sigma$  in the next section.

### 5.10 Mean Square Deviations $\chi$ Versus Standard Deviations $\sigma$

Distributions of the root mean square deviations  $\chi_i$  (see equation. 5.2) from each individual  $G - V$  fit ( $i$ ), for the 6 molecules, are shown in Figure 5.26. The mean values  $\langle\chi\rangle$  of these values of  $\chi_i$  are shown in Table 5.1 for each molecule. Fitting parameter  $\langle\chi\rangle$  is an indicator of the accuracy of the predicted value of  $|S|$  made by ABC theory.

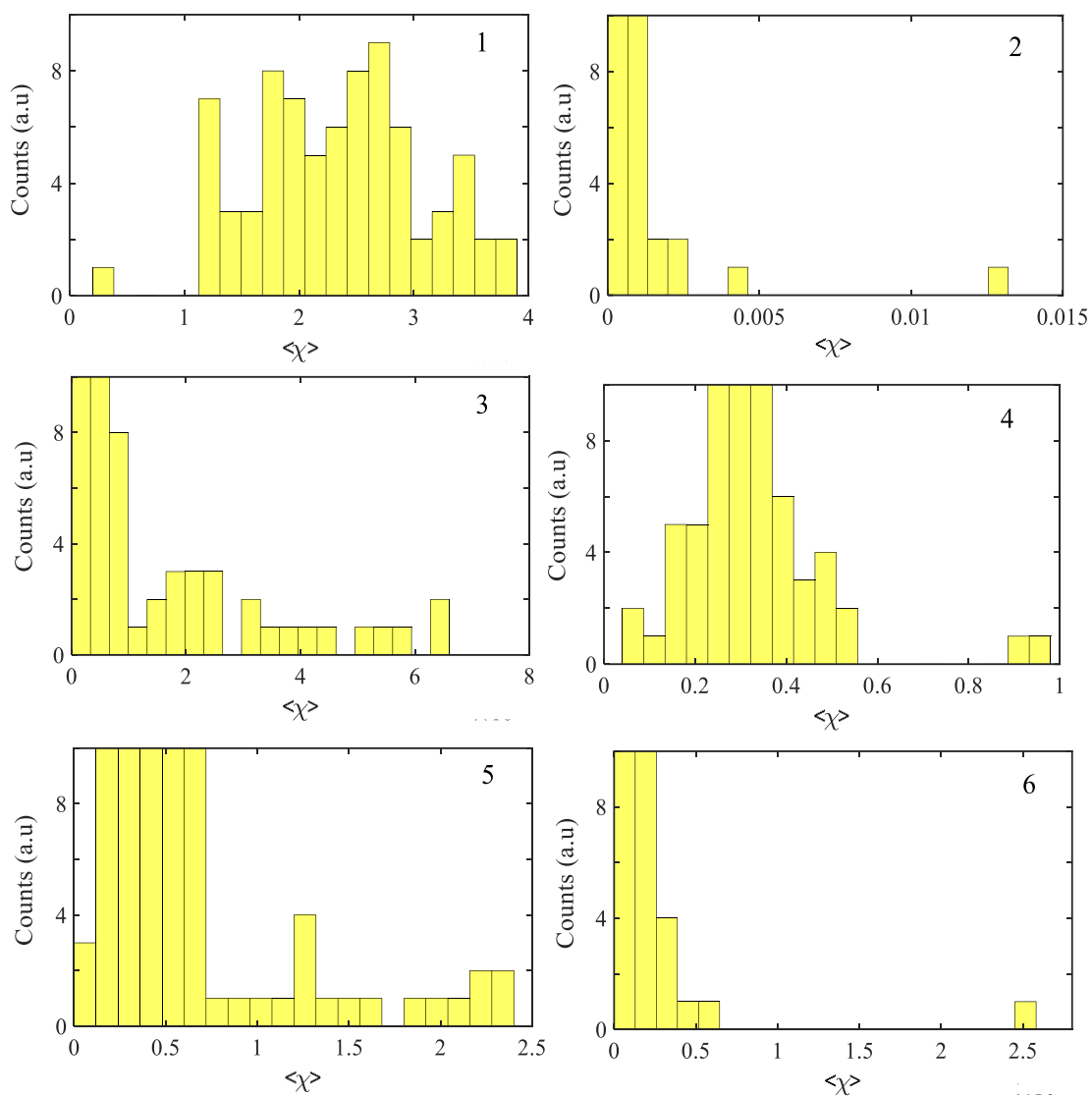


Figure 5.26: Distributions of root mean square deviations ( $\chi$ ) from individual  $G - V$  fits for molecules 1-6.

Table 5.1: A comparison between the differences in standard deviations between theory and experiment ( $\Delta\sigma$ ), and the average root mean square deviations ( $\langle\chi\rangle$ ) from  $G - V$  fits.

Molecule	$\Delta\sigma = \sigma_{ABC} - \sigma_{Exp}$	$\langle\chi\rangle$
<b>1</b>	7.71	4.0E-03
<b>2</b>	12.97	1.5E-02
<b>3</b>	0.75	6.0E-05
<b>4</b>	-3.26	1.0E-04
<b>5</b>	4.23	2.3E-03
<b>6</b>	7.47	2.5E-03

This shows that molecule **2** has the largest root mean square deviations  $\langle\chi\rangle = 1.5 \times 10^{-2}$  and this corresponds to the largest difference  $\Delta\sigma = \sigma_{ABC} - \sigma_{Exp}$  between standard deviations of the theory and experiment. Similarly, molecule **1** has the next highest value of  $\langle\chi\rangle$  and the next highest value of  $\Delta\sigma$ . Molecule **3** has the lowest value of  $\Delta\sigma$  and the lowest value of  $\langle\chi\rangle$ . This correlation between  $\langle\chi\rangle$  and  $\Delta\sigma$  is shown more clearly in Figure 5.26 and demonstrates that the fitting parameter  $\langle\chi\rangle$  is an indicator of the accuracy of the predicted value of  $|S|$  made by ABC theory.

### 5.11 Parameter $c$

In this section, I compare predicted Seebeck coefficients generated when the parameter  $c$  is set to zero, with the values obtained when  $c$  is allowed to be non-zero. For the purpose of a comparison Table 5.2 is created, where I choose 10 ( $I - V$ ) characteristic curves out of nearly a thousand curves for each molecule **1-6**. A curve fitting procedure is applied and the Seebeck coefficient is generated in two cases: when the parameter  $c$  is set to zero and when  $c$  is allowed to be non-zero ( $c = 0$  and  $c \neq 0$ ).

Table 5.2 Absolute ABC predicted theory Seebeck coefficients  $|S|$  ( $\mu\text{V/K}$ ) in two cases  $c = 0$  and  $c \neq 0$  for 10 ( $I - V$ ) characteristic curves for each molecule **1-6** (numbers in parentheses when  $c \neq 0$ ), and experimental Seebeck coefficients.

$I - V$ curve \ M	<b>1</b>	<b>2</b>	<b>3</b>	<b>4</b>	<b>5</b>	<b>6</b>
	$ S_{ABC} $	$ S_{ABC} $	$ S_{ABC} $	$ S_{ABC} $	$ S_{ABC} $	$ S_{ABC} $
1	4.1 (3.6)	7.0 (6.9)	15.6 (15.2)	21.3 (21.0)	25.4 (25.2)	32.5 (32.0)
2	4.5 (4.1)	6.7 (6.5)	16.2 (15.9)	21.2 (20.9)	25.6 (25.4)	32.4 (31.8)
3	4.6 (4.2)	7.1 (6.9)	16.0 (15.7)	20.5 (20.2)	25.5 (25.3)	32.7 (32.4)
4	4.2 (3.7)	7.2 (7.0)	15.9 (15.6)	21.5 (21.2)	25.8 (25.6)	32.6 (32.3)
5	4.1 (3.6)	7.5 (7.4)	16.1 (15.8)	20.6 (20.3)	25.9 (25.7)	32.5 (32.2)
6	4.4 (3.9)	7.4 (7.3)	16.2 (15.9)	20.7 (20.4)	25.5 (25.3)	32.7 (32.4)
7	3.8 (3.4)	7.0 (6.9)	16.1 (15.8)	20.8 (20.5)	25.3 (25.1)	32.2 (31.8)
8	4.3 (3.8)	7.8 (7.6)	16.0 (15.7)	20.9 (20.6)	25.2 (25.0)	32.3 (32.0)
9	4.2 (3.7)	7.4 (7.3)	16.2 (15.9)	21.1 (20.8)	25.9 (25.7)	32.6 (32.3)
10	4.5 (4.1)	7.7 (7.6)	15.8 (15.5)	20.4 (20.1)	26.0 (25.8)	32.5 (32.2)
$ S_{Exp} $	3.0	5.0	14.5	19.5	24.0	29.7

Table 5.2 shows that allowing  $c$  to be non-zero improves the agreement with experiment, though the improvement is rather slight.

By comparing the results of the two cases ( $c = 0$  and  $c \neq 0$ ), one can notice that the difference between them  $\Delta|S| = |S_{c=0}| - |S_{c \neq 0}|$  is the smallest for **2** and the average difference is 0.14, whereas  $\Delta S$  is the largest for **1** (0.46). The biggest and smallest  $\Delta S$  of the studied molecules (**1-6**), can be explained by the  $I - V$  characterisation curves of the studied molecules (see Figures 5.6-5.10). It is clear that the dispersion current ( $I$ ) of **2** is the smallest among the 6 dispersions, whereas, the dispersion current ( $I$ ) of **1** is the largest as shown Figures (5.6-5.10).

In Table 5.3 the average of the absolute Seebeck coefficient of nearly a thousand  $I - V$  characteristic curves has been taken for each molecule in two cases ( $c = 0$  and  $c \neq 0$ ).

Table 5.3: Absolute theoretical Seebeck coefficient  $|S|$  ( $\mu\text{V}/\text{K}$ ) of nearly a thousand ( $I - V$ ) characteristics curve in two cases when ( $c = 0$ ) and ( $c \neq 0$ ) alongside the absolute experimental Seebeck coefficient.

M	$ S_{Exp} $	$ S_{ABC} $ ( $c = 0$ )	$ S_{ABC} $ ( $c \neq 0$ )
<b>1</b>	3.0	4.5	3.8
<b>2</b>	5.0	7.5	7.2
<b>3</b>	14.5	16.5	15.7
<b>4</b>	19.5	21.0	20.0
<b>5</b>	24.0	25.5	25.0
<b>6</b>	29.7	32.5	31.5

It is worth mentioning that in the above analysis, absolute Seebeck coefficients have been calculated by fitting to  $G - V$  curves rather than  $I - V$  curves. In the next section, I show a comparison between the results obtained from  $I - V$  fits and  $G - V$  fits for

twelve different sets of  $I - V$  measurements and demonstrate that the results are comparable.

### 5.12 ( $I - V$ ) Fit Versus ( $G - V$ ) Fit

The above results are obtained from fitting to  $G - V$  curves (see curve fitting section (5.6)). In this section, I choose 12 ( $I - V$ ) characterisation curves (two for each molecule) and directly apply the fitting procedure to each  $I - V$  curve to find the coefficients  $a, b, c$  that are used to calculate the absolute Seebeck coefficient. Table 5.4 shows a comparison between absolute Seebeck coefficients obtained from different fitting to  $G - V$  to those obtained from fitting to  $I - V$ . Clearly, the two fits  $S_{G-V fit}$  and  $S_{I-V fit}$  are comparable.

Table 5.4: Absolute Seebeck coefficient  $|S|$  ( $\mu\text{V}/\text{K}$ ) obtained from two fits, ( $G - V$ ) and ( $I - V$ ).

Molecule	Sample ( $I - V$ curve)	$ S_{G-V \text{ fit}} $	$ S_{I-V \text{ fit}} $	$\Delta S $
<b>1</b>	1	2.0	2.6	0.6
<b>1</b>	2	1.9	2.7	0.8
<b>2</b>	3	3.8	4.1	0.3
<b>2</b>	4	2.6	3.2	0.6
<b>3</b>	5	2.2	2.8	0.6
<b>3</b>	6	2.1	2.6	0.5
<b>4</b>	7	7.6	8.0	0.1
<b>4</b>	8	1.0	1.5	0.5
<b>5</b>	9	3.2	3.7	0.5
<b>5</b>	10	3.6	4.6	1.0
<b>6</b>	11	3.1	3.8	0.7
<b>6</b>	12	2.1	2.5	0.4

### 5.13 Conclusion

By making simultaneous measurements of the Seebeck coefficients and conductance-voltage characteristics of SAMs formed from six anthracene-based molecules with different anchor groups, I have demonstrated that ‘ABC’ theory allows for the prediction of magnitudes of Seebeck coefficients by making fits to measured conductance-voltage relations using three fitting parameters, denoted  $a$ ,  $b$  and  $c$ . This is advantageous because it means that by measuring the  $G - V$  characteristics of single molecules or SAMs, their potential for high-performance thermoelectricity can be assessed without the need for experimentally derived Seebeck coefficients. In addition to this, if measurements of the latter are available, then ‘ABC’ theory can be applied as a consistency check between the two sets of measurements. The theory presented within this work represents an important step forward in the study of molecular thermoelectrics, greatly easing accessibility of the field to those without access to the specialist equipment usually needed to perform such complex thermal measurements.

## 5.14 Bibliography

1. Ren, Y., Zhang, B., & Qiao, H. (1999). A simple Taylor-series expansion method for a class of second kind integral equations. *Journal of Computational and Applied Mathematics*, 110(1), 15-24.
2. Lambert, C. J. (2015). Basic concepts of quantum interference and electron transport in single-molecule electronics. *Chemical Society Reviews*, 44(4), 875-888.
2. Rincón-García, L., Evangeli, C., Rubio-Bollinger, G., & Agraït, N. (2016). Thermopower measurements in molecular junctions. *Chemical Society Reviews*, 45(15), 4285-4306.
3. Cui, L., Miao, R., Jiang, C., Meyhofer, E., & Reddy, P. (2017). Perspective: Thermal and thermoelectric transport in molecular junctions. *The Journal of Chemical Physics*, 146(9), 092201.
4. Williams, C. C., & Wickramasinghe, H. K. (1990). Microscopy of chemical-potential variations on an atomic scale. *Nature*, 344(6264), 317-319.
5. Poler, J. C., Zimmermann, R. M., & Cox, E. C. (1995). Scanning thermopower microscopy of guanine monolayers. *Langmuir*, 11(7), 2689-2695.
6. Paulsson, M., & Datta, S. (2003). Thermoelectric effect in molecular electronics. *Physical Review B*, 67(24), 241403.
7. Reddy, P., Jang, S. Y., Segalman, R. A., & Majumdar, A. (2007). Thermoelectricity in molecular junctions. *Science*, 315(5818), 1568-1571.

8. Baheti, K., Malen, J. A., Doak, P., Reddy, P., Jang, S. Y., Tilley, T. D., ... & Segalman, R. A. (2008). Probing the chemistry of molecular heterojunctions using thermoelectricity. *Nano letters*, 8(2), 715-719.
9. Malen, J. A., Doak, P., Baheti, K., Tilley, T. D., Segalman, R. A., & Majumdar, A. (2009). Identifying the length dependence of orbital alignment and contact coupling in molecular heterojunctions. *Nano letters*, 9(3), 1164-1169.
10. Finch, C. M., Garcia-Suarez, V. M., & Lambert, C. J. (2009). Giant thermopower and figure of merit in single-molecule devices. *Physical review b*, 79(3), 033405.
11. Yee, S. K., Malen, J. A., Majumdar, A., & Segalman, R. A. (2011). Thermoelectricity in fullerene-metal heterojunctions. *Nano letters*, 11(10), 4089-4094.
12. Tan, A., Balachandran, J., Sadat, S., Gavini, V., Dunietz, B. D., Jang, S. Y., & Reddy, P. (2011). Effect of length and contact chemistry on the electronic structure and thermoelectric properties of molecular junctions. *Journal of the American Chemical Society*, 133(23), 8838-8841.
13. Balachandran, J., Reddy, P., Dunietz, B. D., & Gavini, V. (2012). End-group-induced charge transfer in molecular junctions: effect on electronic-structure and thermopower. *The Journal of Physical Chemistry Letters*, 3(15), 1962-1967.
14. Widawsky, J. R., Chen, W., Vazquez, H., Kim, T., Breslow, R., Hybertsen, M. S., & Venkataraman, L. (2013). Length-dependent thermopower of highly conducting Au-C bonded single molecule junctions. *Nano letters*, 13(6), 2889-2894.

15. Chang, W. B., Mai, C. K., Kotiuga, M., Neaton, J. B., Bazan, G. C., & Segalman, R. A. (2014). Controlling the thermoelectric properties of thiophene-derived single-molecule junctions. *Chemistry of Materials*, 26(24), 7229-7235.
16. Evangeli, C., Gillemot, K., Leary, E., Gonzalez, M. T., Rubio-Bollinger, G., Lambert, C. J., & Agrait, N. (2013). Engineering the thermopower of C60 molecular junctions. *Nano letters*, 13(5), 2141-2145.
17. Kim, Y., Jeong, W., Kim, K., Lee, W., & Reddy, P. (2014). Electrostatic control of thermoelectricity in molecular junctions. *Nature nanotechnology*, 9(11), 881.
18. Rincón-García, L., Ismael, A. K., Evangeli, C., Grace, I., Rubio-Bollinger, G., Porfyraakis, K., ... & Lambert, C. J. (2016). Molecular design and control of fullerene-based bi-thermoelectric materials. *Nature materials*, 15(3), 289-293.
19. Zerah-Harush, E., & Dubi, Y. (2015). Enhanced Thermoelectric Performance of Hybrid Nanoparticle–Single-Molecule Junctions. *Physical Review Applied*, 3(6), 064017.
20. Yzambart, G., Rincón-García, L., Al-Jobory, A. A., Ismael, A. K., Rubio-Bollinger, G., Lambert, C. J., ... & Bryce, M. R. (2018). Thermoelectric Properties of 2, 7-Dipyridylfluorene Derivatives in Single-Molecule Junctions. *The Journal of Physical Chemistry C*, 122(48), 27198-27204.
21. Bergfield, J. P., Solis, M. A., & Stafford, C. A. (2010). Giant thermoelectric effect from transmission supernodes. *ACS nano*, 4(9), 5314-5320.

22. Leijnse, M., Wegewijs, M. R., & Flensberg, K. (2010). Nonlinear thermoelectric properties of molecular junctions with vibrational coupling. *Physical Review B*, 82(4), 045412.
23. Ismael, A. K., Grace, I., & Lambert, C. J. (2015). Increasing the thermopower of crown-ether-bridged anthraquinones. *Nanoscale*, 7(41), 17338-17342.
24. Nozaki, D., Sevinçli, H., Li, W., Gutiérrez, R., & Cuniberti, G. (2010). Engineering the figure of merit and thermopower in single-molecule devices connected to semiconducting electrodes. *Physical Review B*, 81(23), 235406.
25. Karlström, O., Linke, H., Karlström, G., & Wacker, A. (2011). Increasing thermoelectric performance using coherent transport. *Physical Review B*, 84(11), 113415.
26. Bürkle, M., Zotti, L. A., Viljas, J. K., Vonlanthen, D., Mishchenko, A., Wandlowski, T., ... & Pauly, F. (2012). Ab initio study of the thermopower of biphenyl-based single-molecule junctions. *Physical review b*, 86(11), 115304.
27. Al-Khaykane, M. K., Ismael, A. K., Grace, I., & Lambert, C. J. (2018). Oscillating Seebeck coefficients in  $\pi$ -stacked molecular junctions. *RSC advances*, 8(44), 24711-24715.
28. Zotti, L. A., Bürkle, M., Pauly, F., Lee, W., Kim, K., Jeong, W., ... & Cuevas, J. C. (2014). Heat dissipation and its relation to thermopower in single-molecule junctions. *New Journal of Physics*, 16(1), 015004.

29. Hüser, F., & Solomon, G. C. (2015). From chemistry to functionality: Trends for the length dependence of the thermopower in molecular junctions. *The Journal of Physical Chemistry C*, *119*(25), 14056-14062.
30. Lambert, C. J., Sadeghi, H., & Al-Galiby, Q. H. (2016). Quantum-interference-enhanced thermoelectricity in single molecules and molecular films. *Comptes Rendus Physique*, *17*(10), 1084-1095.
31. Noori, M., Sadeghi, H., Al-Galiby, Q., Bailey, S. W., & Lambert, C. J. (2017). High cross-plane thermoelectric performance of metallo-porphyrin molecular junctions. *Physical Chemistry Chemical Physics*, *19*(26), 17356-17359.
32. Ismael, A. K., & Lambert, C. J. (2020). Molecular-scale thermoelectricity: a worst-case scenario. *Nanoscale Horizons*, *5*(7), 1073-1080.
33. Famili, M., Grace, I. M., Al-Galiby, Q., Sadeghi, H., & Lambert, C. J. (2018). Toward high thermoelectric performance of thiophene and ethylenedioxythiophene (EDOT) molecular wires. *Advanced Functional Materials*, *28*(15), 1703135.
34. Hou, S., Wu, Q., Sadeghi, H., & Lambert, C. J. (2019). Thermoelectric properties of oligoglycine molecular wires. *Nanoscale*, *11*(8), 3567-3573.
35. Naghibi, S., Ismael, A. K., Vezzoli, A., Al-Khaykane, M. K., Zheng, X., Grace, I. M., ... & Nichols, R. J. (2019). Synthetic Control of Quantum Interference by Regulating Charge on a Single Atom in Heteroaromatic Molecular Junctions. *The journal of physical chemistry letters*, *10*(20), 6419-6424.

36. Ismael, A. K., Wang, K., Vezzoli, A., Al-Khaykane, M. K., Gallagher, H. E., Grace, I. M., ... & Higgins, S. J. (2017). Side-Group-Mediated Mechanical Conductance Switching in Molecular Junctions. *Angewandte Chemie International Edition*, 56(48), 15378-15382.
37. Capozzi, B., Low, J. Z., Xia, J., Liu, Z. F., Neaton, J. B., Campos, L. M., & Venkataraman, L. (2016). Mapping the transmission functions of single-molecule junctions. *Nano letters*, 16(6), 3949-3954.
38. Tschudi, S. E., & Reuter, M. G. (2016). Estimating the Landauer– Büttiker transmission function from single molecule break junction experiments. *Nanotechnology*, 27(42), 425203.
39. Wang, X., Bennett, T. L., Ismael, A., Wilkinson, L. A., Hamill, J., White, A. J., ... & Lambert, C. J. (2020). Scale-up of room-temperature constructive quantum interference from single molecules to self-assembled molecular-electronic films. *Journal of the American Chemical Society*, 142(19), 8555-8560.
40. Ismael, A., Wang, X., Bennett, T. L., Wilkinson, L. A., Robinson, B. J., Long, N. J., ... & Lambert, C. J. (2020). Tuning the thermoelectrical properties of anthracene-based self-assembled monolayers. *Chemical science*, 11(26), 6836-6841.

## Chapter 6

### 6. Conclusion and Future Work

#### 6.1 Conclusion

In this thesis, I have presented the main equations and tools which provide the foundation for my work, including the Schrödinger equation, density functional theory (DFT), and the SIESTA package which implements DFT and solves these equations. I have also introduced single particle transport theory, which is based on the Hamiltonian and Green's functions, and have given some example calculations to demonstrate its use. These concepts are reported in chapters 2 and 3, respectively.

Chapter 4 is the first result chapter in this thesis, where I started by investigating how to optimise power harvesting by controlling the pressure applied to anthracene-based molecular junctions. Herein, I used the tilt angle  $\theta$  as a key parameter for seeking the optimum power. In this chapter, two anthracene-based SAMs were explored. Both are terminated with thioacetate (ASc), however they differ by the connectivity. SAM-1 is 9,10-Di(4-(ethynyl)phenylthioacetate), whereas SAM-2 is 1,5-Di(4-(ethynyl)phenylthioacetate). I have demonstrated that the thermoelectric properties of such molecular devices can be controlled by taking advantage of their mechanical flexibility, more specifically tuning the optimum power via the applied pressure (tilt angle  $\theta$ ).

Through systematic theoretical simulations, I showed how the tilt angle  $\theta$  plays a role as a pivotal parameter in increasing the conductance  $G$  and decreasing the thermopower

$S$  and ultimately achieving the optimum power  $P = G S^2$  at tilt angle of approximately  $\theta \approx 65^\circ$ . An excellent agreement has been achieved between my simulations and the experimental measurements for both SAMs.

In chapter 6, my second result chapter, I confronted the question of whether the Seebeck coefficient of a junction can be predicted from a simple measured  $I - V$  curve. I explained the advantages of making such a prediction. One benefit could be that the experimentally more difficult task of creating an experimental set-up to measure their thermoelectric properties could be avoided.

In this chapter, I presented a novel strategy for predicting an upper bound to the Seebeck coefficient of single molecules or SAMs, from measurements of their  $G - V$  characteristics. I demonstrated a curve fitting procedure, which begins by making a fit to measured  $G - V$  curves using three fitting parameters, denoted  $a, b$ , and  $c$ . I explained the relation between the Taylor expansion and the transmission coefficient. I referred to this method as the ‘ABC’ theory.

‘ABC’ theory predicted a maximum value for the magnitude of the corresponding Seebeck coefficient. This is a useful material parameter, because if the predicted upper bound is large, then the material would warrant further investigation using a full Seebeck measurement setup. On the other hand, if the upper bound is small, then the material would not be promising and this much more technically demanding set of measurements would be avoided.

Histograms of predicted Seebeck coefficients of the ‘ABC’ theory were compared against histograms of the directly measured Seebeck coefficients from the Scanning

Tunneling Microscope STM device. Furthermore, the standard deviations  $\sigma$  obtained from experiment and predicted ‘*ABC*’ theory for six different SAMs, formed from anthracene-based molecules with different anchor groups including: pristine thioether, pristine thioacetate, pristine pyridine and a mixture of thioether and pyridine. These six SAMs are mixture of two different connectivities mainly **1-5** or **9-10**.

Finally, I discussed the case when the three parameters  $a, b, c$  of the ‘*ABC*’ theory were reduced to two (only  $a$  and  $b$ ) by setting  $c$  to be equal to zero. A comparison was made between the two cases ( $c=0$  and  $c \neq 0$ ) by checking both against the STM experiment results and excellent agreement was found.

The theory presented within this work represents an important step forward in the study of molecular thermoelectric, greatly increasing the accessibility of the field to those without access to the specialist equipment usually needed to perform such complex thermal measurements.

## **6.2 Future work**

One very interesting direction of research would be employing the *ABC* theory for searching for high-performance thermoelectricity materials. Searching for high-performance thermoelectricity materials can be assessed without the need for experimentally derived Seebeck coefficients. Moreover, if measurements of the latter are available, then ‘*ABC*’ theory can be applied as a consistency check between the two sets of measurements.

The optimum power harvesting of SAMs or single molecule discussed in this study is very promising, however there are still number of open questions. For example, the effect of the anchor group.